

**RADIO OBSERVATIONS OF THE MOON AND VENUS
AT 8.6 MM WAVELENGTH**

FINAL REPORT

CONTRACT NO. NASw-593

MAY 1, 1962 - NOVEMBER 1, 1963

FACILITY FORM 602

N66 28655

(ACCESSION NUMBER)

136

(PAGES)

CR-753K3

(NASA CR OR TTR OR AD NUMBER)

N66 28660

(THRU)

1

(CODE)

30

(CATEGORY)

PREPARED FOR:

OFFICE OF LUNAR AND PLANETARY PROGRAMS

NASA HEADQUARTERS

WASHINGTON, D.C.

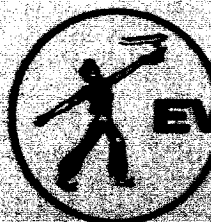
GPO PRICE \$ _____

CFSTI PRICE(S) \$ _____

Hard copy (HC) _____

Microfiche (MF) _____

653 July 65



EWEN KNIGHT

Doc. # 1088

Copy # 10

RADIO OBSERVATIONS OF THE MOON AND VENUS

AT 8.6 MM WAVELENGTH

FINAL REPORT

CONTRACT NO. NASw-593

MAY 1, 1962 - NOVEMBER 1, 1965

PREPARED FOR:

OFFICE OF LUNAR AND PLANETARY PROGRAMS

NASA HEADQUARTERS

WASHINGTON, D. C.

TABLE OF CONTENTS

INTRODUCTION

PART I - RADIO OBSERVATIONS OF THE MOON AND VENUS AT 8.6 MM WAVELENGTH

✓ SECTION A - Thermal Radiation from the Moon at 8.6 mm
Wavelength

✓ SECTION B - A Two-Layer Model of the Lunar Surface

✓ SECTION C - Observations of Venus Near the 1962 Inferior
Conjunction

✓ SECTION D - Observations of Venus Near the 1964 Inferior
Conjunction

✓ PART II - ATMOSPHERIC EFFECTS ON CELESTIAL RADIO MEASUREMENTS AT 8.6 MM

1.0 INTRODUCTION

2.0 THEORETICAL CONSIDERATIONS

3.0 REVIEW OF OBSERVATIONAL METHODS AND DATA

4.0 MEASUREMENT PROGRAM

5.0 RADOME CONSIDERATIONS

ADDENDUM - PART II - Atmospheric Characteristics

INTRODUCTION

The prime objective of this investigation was to measure the radio lutation curve characteristics for several selected regions on the lunar surface and, by comparison of this data with available analytical models of lunar surface structure, derive conclusions concerning the most probable material content of lunar surface material.

The approach was predicated on minor modification of an existing 28-foot radio telescope facility originally developed under Navy Contract No. NObs-3977 for observation of radio stars at a frequency of 8 GHz. The modifications to the telescope were in part supported under Air Force Contract No. AF33(616)-7414 and included the addition of a polyurethane foam, zinc sprayed 28-foot diameter parabolic reflector capable of operation in the lower millimeter portion of the spectrum, a remotely-adjustable, mechanically-driven RF head focusing unit and several critical millimeter radiometric components.

The NASA effort reported here was undertaken prior to completion and evaluation of the several modifications introduced in the telescope to improve its upper frequency response characteristics.

The scope of the modification program was limited to the minimum changes considered adequate to capitalize on the availability of an existing facility in order to provide high angular resolution lunar radio data at millimeter wavelengths. Approximately one-third of the total investment in the three-year investigation was associated with the engineering effort and the material costs associated with the completion of telescope modifications originally undertaken under Air Force Contract No. AF33(616)-7414. The remaining two-thirds of program costs were associated with the accumulation of observational data, data reduction and analysis.

It was recognized at the outset that a fully instrumented precision telescope of competitive performance would cost well in excess of one million dollars. The instrument used in this program was made available at a program cost of less than one-fifth that amount.

The original intent was to obtain observational data at three frequencies: 8 GHz, 35 GHz, and 75 GHz. The 8 GHz observations were given low priority in view of the relatively poor angular resolution and the potential availability of comparable data from other existing telescopes within the U.S.

During the telescope modification and evaluation phase, several advanced engineering problems were encountered, notably:

- The determination of the physical location of the focal plane

- Radome effects

- Atmospheric effects

A period of three months was devoted to establishing the position of the focal plane of the antenna when operating at a frequency of 35 GHz (8.6 millimeter wavelengths). The degree of difficulty encountered, coupled with the measured efficiency of the aperture at this frequency, suggested the inadvisability of proceeding with observations at the upper 75 GHz frequency (4 millimeter wavelengths). For the reasons noted above, all observations were concentrated at a wavelength of 8.6 millimeters.

This final report on the investigation has been prepared in two parts. Part I provides a summary of the scientific results derived from the lunar and Venus observations presented in the form of four preprints of technical articles submitted for publication in recognized scientific journals. Part II of the report describes the effect of atmospheric attenuation and reradiation on observational data obtained at millimeter wavelengths, with particular emphasis on methods of data reduction as well as the techniques of observation deemed most appropriate for measurements of this type.

Summary

Of most notable significance is the fact that high angular resolution radio observations of various regions of the lunar surface at 8.6 millimeters do not show a marked difference. This suggests that the upper surface layer of the moon is of the same general material, independent of the optically observed form; i.e., mountainous, crater-packed, or maria.

Harmonic analysis of the data and comparison with the single layer homogeneous model of Piddington and Minnett shows lack of correlation, particularly with regard to the 45° maximum phase delay required by this analytical model.

A two-layer analytical model was developed and the measured data compared with the predictions of this model. The correlation of measured data with the predictions of the two-layer model in regard to amplitude and phase of the harmonic content of the lunation curve were equally disappointing. The two-layer model allows a relatively large dynamic range of amplitude and phase for the various harmonics of the lunation curve when compared to the simple single layer or homogeneous model. An indication of a "better fit" with the two-layer model than with the homogeneous model is undoubtedly influenced by the reduced degree of restraint imposed on the amplitude and phase of the various harmonics.

The lack of correlation between measured data and analytical models is not surprising when one considers the limitations inherent in each. Perhaps the most serious criticism of present analytical models for both infrared as well as millimeter and microwave lunation characteristics, is the assumption of a smooth surface. It is clear from photographs of the moon that the surface is definitely not smooth and the crevices, rills and craters will therefore exhibit distorted periodic heating and cooling cycles. The degree to which randomly distributed rills, craters and crevices would affect the amplitude and phase characteristics of an otherwise homogeneous material would be of considerable interest, but does require a more intensive analytical effort than undertaken to date. Observational data encounters limitations associated with the realizable degree of angular as well as amplitude resolution, absolute calibration and errors associated with atmospheric effects. For the measurements reported here, the radome represents an additional source of error.

It is evident as a result of this investigation that the derivation of knowledge concerning lunar surface material characteristics by passive radiometric techniques will not be an easy task. An improvement in measurement capability combined with less simplified analytical models free of obvious unrealistic physical assumptions is required if we hope to obtain more fruitful results via this potentially valuable method

of measurement. This single fact represents a significant scientific contribution of the investigation. We now know that an easy solution is not available, that more powerful measurement instruments are required, and more physically-consistent analytical models must be developed. We now know the nature of the signal and from this information are able to establish the requirements for future measurements which will be made from earth as well as lunar orbit.

PART I

RADIO OBSERVATIONS OF THE MOON AND VENUS

AT 8.6 MM WAVELENGTH

BY

JACK COPELAND

INTRODUCTION TO PART 1

The scientific findings resulting from the lunar and Venus observations are presented in this portion of the report.

Since the scientific results either have been or will be submitted to recognized scientific journals for publication, the most clear and concise presentation of such information is simply the reprints or preprints of the papers themselves. Consequently, this report consists of four sections each of which is a reprint or preprint of four technical papers which describe the results obtained in the four major areas of investigation:

- A. Radio observations of Venus near the 1962 inferior conjunction.
- B. Theoretical consideration of lunar surface models.
- C. Radio observations of the moon from August 1963 to August 1964.
- D. Radio observations of Venus during the 1964 inferior conjunction.

Each section includes within itself all the necessary information to stand alone as a separate report, and therefore, each section is numbered separately.

PART I

TABLE OF CONTENTS

- A. THERMAL RADIATION FROM THE MOON AT 8.6MM WAVELENGTH
- B. A TWO-LAYER MODEL OF THE LUNAR SURFACE
- C. OBSERVATIONS OF VENUS NEAR THE 1962 INFERIOR CONJUNCTION
- D. OBSERVATIONS OF VENUS NEAR THE 1964 INFERIOR CONJUNCTION

N66.28656

SECTION A

THERMAL RADIATION FROM THE MOON AT 8.6 MM WAVELENGTH

ABSTRACT

SECTION A - PART 1

THERMAL RADIATION FROM THE MOON AT 8.6 MM WAVELENGTH

28656

Observations of the moon with an angular resolution of $4 \times 5\frac{1}{2}$ minutes of arc were made at 8.6 mm wavelength during the one-year period from August, 1963 through August, 1964. By means of a raster scan technique, antenna temperatures as functions of local phase angle were obtained for four selected regions of the lunar surface.

The data were corrected for radome attenuation, which was measured directly and daily corrections calculated from ground level meteorological data were made for the effects of atmospheric attenuation.

The temperature versus phase angle curves were corrected for antenna smoothing before being examined from the standpoint of both one and two layer models. Although the absolute temperatures and phase angles are subject to some uncertainty, the data are generally inconsistent with the homogeneous model for the lunar surface, but agrees with what would be expected from a layered structure.

Author

N66 28656

TABLE OF CONTENTS

SECTION A

THERMAL RADIATION FROM THE MOON AT 8.6 MM WAVELENGTH

	<u>Page No.</u>
ABSTRACT	
A. 1 INTRODUCTION	1
A. 2 MEASUREMENT EQUIPMENT	1
A. 3 OBSERVATIONAL PROCEDURE	2
A. 4 DATA REDUCTION	2
A. 4.1 Correction for Atmospheric Attenuation	4
A. 4.2 Instrument Calibration	4
A. 5 OBSERVATIONAL DATA	5
A. 6 DATA INTERPRETATION	9
A. 7 CONCLUSIONS	11
APPENDIX I-A - CORRECTION PROCEDURE FOR ANTENNA SMOOTHING	22
REFERENCES	

LIST OF FIGURES
SECTION A - PART I

<u>Figure No.</u>	<u>Title</u>	<u>Page No.</u>
A-1	A Typical Set of Scans Across the Lunar Disk	3
A-2 (a)	Antenna Pattern in Hour Angle	6
A-2 (b)	Antenna Pattern in Declination	7
A-3	The Four Regions of the Lunar Surface Under Consideration	8
A-4	Antenna Temperature as a Function of Local Phase Angle for the Copernicus Region	16
A-5	Antenna Temperature as a Function of Local Phase Angle for the Mare Nubium Region	17
A-6	Antenna Temperature as a Function of Local Phase Angle for the Mountainous Region	18
A-7	Antenna Temperature as a Function of Local Phase Angle for the Region of Maria Serenitatis and Tranquillitatis	19
A-8	Theoretical Infrared Temperature as a Function of Phase Angle for $(k p c)^{-1/2}$ approximately 1200	20
A-9	The Hour Angle Antenna Pattern Projected on Lunar Surface and Centered on the Copernicus Region. The Pattern is Considered Zero Beyond the Edges of the Lunar Disk.	21

ADDENDUM

1-1	A Sketch Illustrating the Approximate Relative Size of Antenna Patterns and the Lunar Disk	23
1-2	The Geometry of the Coordinate Transformation	24

LIST OF TABLES

SECTION A

	<u>Page No.</u>
A-1 ANTENNA TEMPERATURES	13
A-2 INFRARED TEMPERATURES	14
A-3 MICROWAVE TEMPERATURES	15

A.1 INTRODUCTION

The nature of thermal radiation from the moon depends upon the wavelength at which it is observed. The lunar surface material is opaque to radiation at infrared wavelengths, so that infrared observations yield the temperature of the outermost surface skin. However, the lunar surface is partially transparent to radiation of microwave wavelengths and measurements at these wavelengths necessarily give a weighted average temperature with depth.

Early microwave measurements (Piddington and Minnet 1949) revealed that a simple homogeneous model for the lunar surface could not adequately explain the observational results at both microwave and infrared wavelengths. It is generally agreed (Piddington and Minnet 1949; Jaeger and Harper 1950; Jaeger 1953; Jaeger 1959; Gibson 1958) that if the lunar surface were considered covered with a thin layer of poorly conducting material, the microwave and infrared results could be brought into closer agreement. More recently, investigators in the Soviet Union (Troitskii, 1965; Salomonovich 1962; Troitskii 1962; Krotikov and Troitskii, 1964) have concluded from various measurements at different wavelengths that the lunar surface is probably homogeneous to a depth of the order of meters, although there is some disagreement (Levin, 1964). It has been speculated that recent photographic evidence from the Ranger spacecrafts indicates, at least in a qualitative manner, that there exists a deep layer of porous material to depths of many feet.

The objective of the program was to determine the brightness temperature as a function of phase angle for selected regions of the lunar surface in an effort to detect possible variations in subsurface material characteristics between the different regions. The observations were performed with a 28-foot diameter radome enclosed antenna which exhibits half-power beamwidths of 4 minutes of arc in declination and 5 1/2 minutes of arc in hour angle. Daily raster-type scans in hour angle were made, weather permitting, during the one year period from August 1963 through August 1964.

The data was corrected for the radome attenuation, which was measured directly, and daily corrections, calculated from ground level meteorological data, were made for the effects of atmospheric attenuation.

The temperature versus phase angle curves were corrected for antenna beam filling and smoothing before being examined from the standpoint of both one and two layer models.

A.2 MEASUREMENT EQUIPMENT

The antenna is a 28-foot diameter equatorially mounted paraboloidal antenna, which is enclosed in an air-supported radome. The antenna pattern, which will be described later, is asymmetric.

The radiometer is a conventional Dicke-type superheterodyne with switching between two feed horns, one of which points outward with a half-power beamwidth of about 10° .

The radiometer fluctuations with a one second time constant is about 4° peak-to-peak.

The front end of the radiometer, including the IF preamplifier, is located on the antenna feed ring, and the remainder, from IF amplifier to a strip chart recorder, is located near the antenna control console.

A.3 OBSERVATIONAL PROCEDURE

All observations were made near meridional crossing on reasonably clear days when the radome was dry. The observational procedure was as follows:

- a. The absolute pointing accuracy of the antenna drives and readouts are not known; the relative readout accuracy, however, was found to be about one minute of arc. The moon was first located radiometrically, and the antenna beam was boresighted approximately on the center of the lunar disk. While tracking in hour angle, a slow scan in declination (always from south to north to eliminate the effects of possible backlash in the drive) permitted the declination dial reading corresponding to the center of the scan to be determined. Declination settings for scans in hour angle were calculated for 4, 8, and 12 minutes of arc north and south of the center of the disk in declination.
- b. The seven scans in hour angle at the relative declinations given above, were made at sidereal rate; i.e., the antenna was positioned west of the moon and the earth's motion permitted to move the antenna beam across the lunar disk.
- c. A nominal 100° calibrate signal, which is approximately equal to the antenna temperature due to the moon, was turned on prior to and after each of the seven scans.
- d. The two points on each scan in hour angle corresponding to the edges of the lunar disk were then determined from scan rate and chart speed and compared with the angular size of the lunar disk as tabulated in the ephemerides. The location of these two points coincided with the half-power points on the scan to within plus and minus one minute of arc. The accuracy of this procedure was verified from similar scans of the solar disk.

Outside temperature and relative humidity were continuously recorded in order that surface water vapor density could be calculated.

A.4 DATA REDUCTION

Each days observation supplied seven drift scans. A typical set of daily scans made near full moon is shown in Figure A-1. Antenna temperatures were taken from the center of each drift scan and at points east and west from the center separated by 4 minutes of arc from the edges of the lunar disk. This procedure gave a total of 37 points for each day. The location of these points on the lunar surface was determined in selenographic longitude and latitude by means of a rotatable plastic overlay, on which were inscribed the paths of each scan, on a 28-inch diameter lunar map.

N

W

E

S

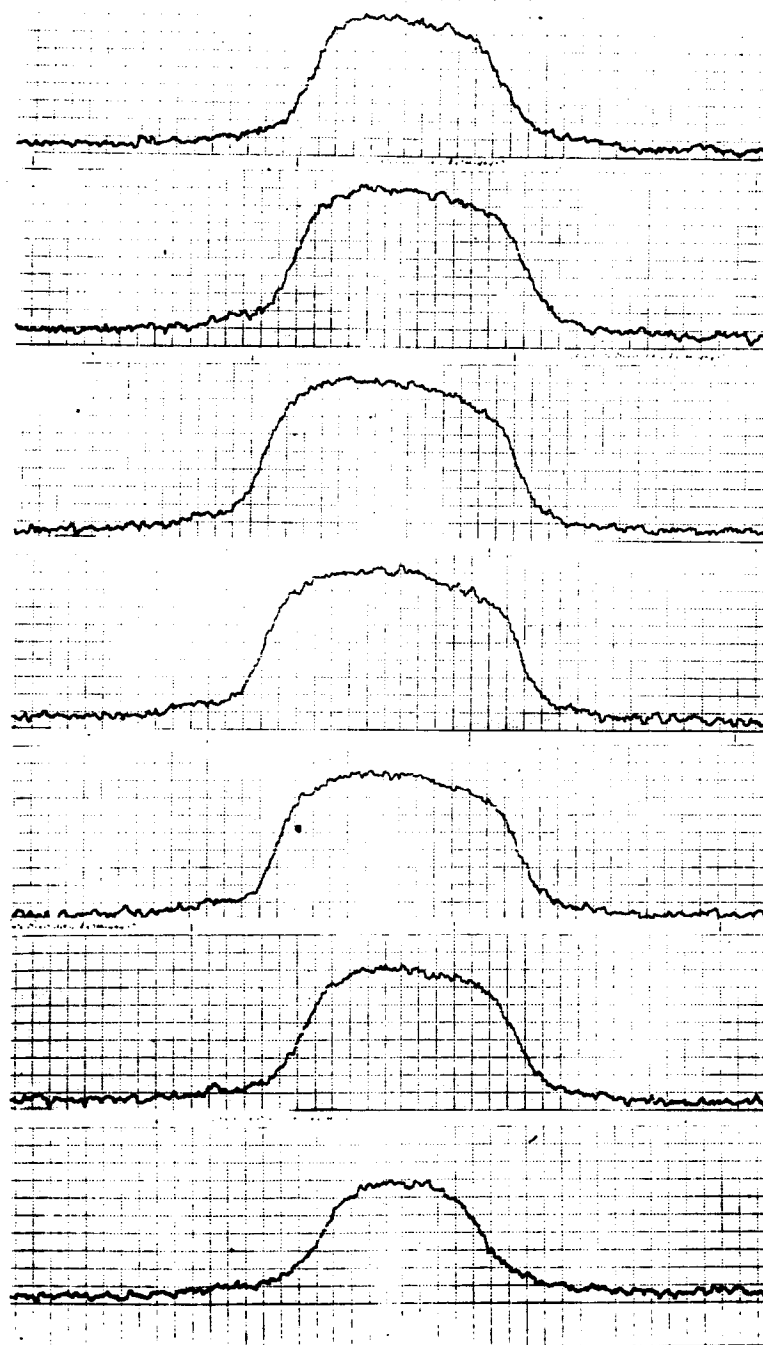


Figure A-1- A typical set of scans across the lunar disk. The lunar phase angle is 6° and the position angle of the polar axis is 2° . The maximum temperature of the central scan is approximately 100°K .

After some simple intermediate calculations then, the data for each day of observation consists of antenna temperatures for 37 points on the lunar surface, their location on the lunar surface in latitude and longitude, the separation in longitude of each point from the longitude of the subsolar point, and the outside temperature and relative humidity at the time of observation.

A.4.1 Correction For Atmospheric Attenuation

The atmospheric attenuation at 8.6 mm is caused primarily by the presence of oxygen and water vapor. If one assumes a homogeneous, plane parallel atmosphere, the effect of atmospheric attenuation can be removed by multiplying by the factor $\exp [(\tau_{H_2O} + \tau_{O_2}) \sec \Theta]$, where τ_{O_2} and τ_{H_2O} are the zenith optical depths due to oxygen and water vapor respectively, and Θ is the zenith angle at the time of observation.

The optical depth, τ_{O_2} , was taken to be constant and equal to 0.0276 (Meeks and Lilley, 1963). The value for τ_{H_2O} depends on the water vapor content. A model due to Barrett and Chung, 1962, gives 0.006 per cubic meter of surface water vapor density. The daily values of $\exp [(\tau_{H_2O} + \tau_{O_2}) \sec \Theta]$, so calculated ranged from 1.05 to about 1.20, with a typical value of about 1.12.

Although the validity of using values obtained from a single atmospheric model under varying weather conditions is most certainly questionable, it was believed that the more or less random part of the error would average to a low value over long periods of observation, and any systematic error would probably be less than the systematic error in instrumental calibrations.

A.4.2 Instrument Calibration

Instrumental calibration involved the following considerations:

1. The nominal 100° calibrate signal, which was obtained by means of a 10,000°K noise tube via a directional coupler and an attenuator, should be compared to a thermal load.
2. The radome attenuation, which was originally estimated as 2.3 db from laboratory measurements on an unweathered sample of radome material, should be measured directly.
3. The antenna beam, although narrow, is not completely filled. Also, the antenna temperatures as a function of phase angles are not the true brightness distributions with lunar longitude since they are averages over the lunar disk, weighted by the antenna pattern.

The radome loss was measured directly in the following manner. The radiometer was removed from the feed ring of the antenna and mounted, with a 2-foot diameter antenna on an equatorial tripod-supported telescope mount. Solar antenna temperatures measured from inside and outside of the radome were compared. The ratio of solar antenna

temperature to the calibrate signal was found to be 7.40 ± 0.14 (6 measurements) outside the radome and 4.75 ± 0.12 (12 measurements) inside the radome. The radome loss is, therefore, 1.93 (+ 0.33 db, - 0.44 db).

The nominal 100°K noise tube calibrate signal was compared with thermal loads at 20°C and -7°C and found to be 96.5 ± 2.45 °K (6 measurements).

Knowledge of the antenna pattern is particularly crucial to the interpretation of the data, since averages over a wide range of phase angles are made.

Antenna pattern measurements were performed at the conclusion of the observational program. A power monitored klystron with a 2-foot diameter paraboloid was located at a site which was 8 1/2 miles from the antenna, and elevated approximately 500 feet. Although the far field requirements are not quite met, and the elevation angle was nearly zero, the transmitting site was the most remote available location.

The measured antenna patterns in hour angle and declination are shown in Figure A-2. The declination pattern is quite satisfactory; however, the hour angle pattern is badly deteriorated. The asymmetry in the pattern is believed to be caused by the method of fabrication and assembly that was used. The reflector was machined in two halves which were subsequently mated and attached to the supporting structure at the observational site. The demarcation line between the two halves is north-south, which indicates that the deteriorated hour angle pattern is probably the result of unsatisfactory mating of the two halves.

The antenna gain was also measured by comparison with a standard gain (20 db) horn and found to be $64.8 \text{ db} \pm 1.21 \text{ db s.d.}$ (6 observations). The signal-to-noise ratio when the standard gain horn was used, however, was so low that the calculated value of the standard deviation from the mean of 64.8 db is probably low, particularly since only 6 measurements were made. A more reasonable value for the uncertainty in the measured gain is probably closer to 2.0 db.

A.5 OBSERVATIONAL DATA

Four regions, identified from their optical features, were chosen for consideration. They were:

1. The region containing the craters Copernicus and Kepler.
2. The region of Mare Nubium.
3. The region containing the two Maria Serenitatis and Tranquillitatis.
4. The generally mountainous region in the southwest quadrant.

These four regions are outlined in Figure A-3.

The antenna temperatures and phase angles relative to the subsolar point for each of the four regions were extracted from the basic data and corrected for radome loss and atmospheric attenuation.

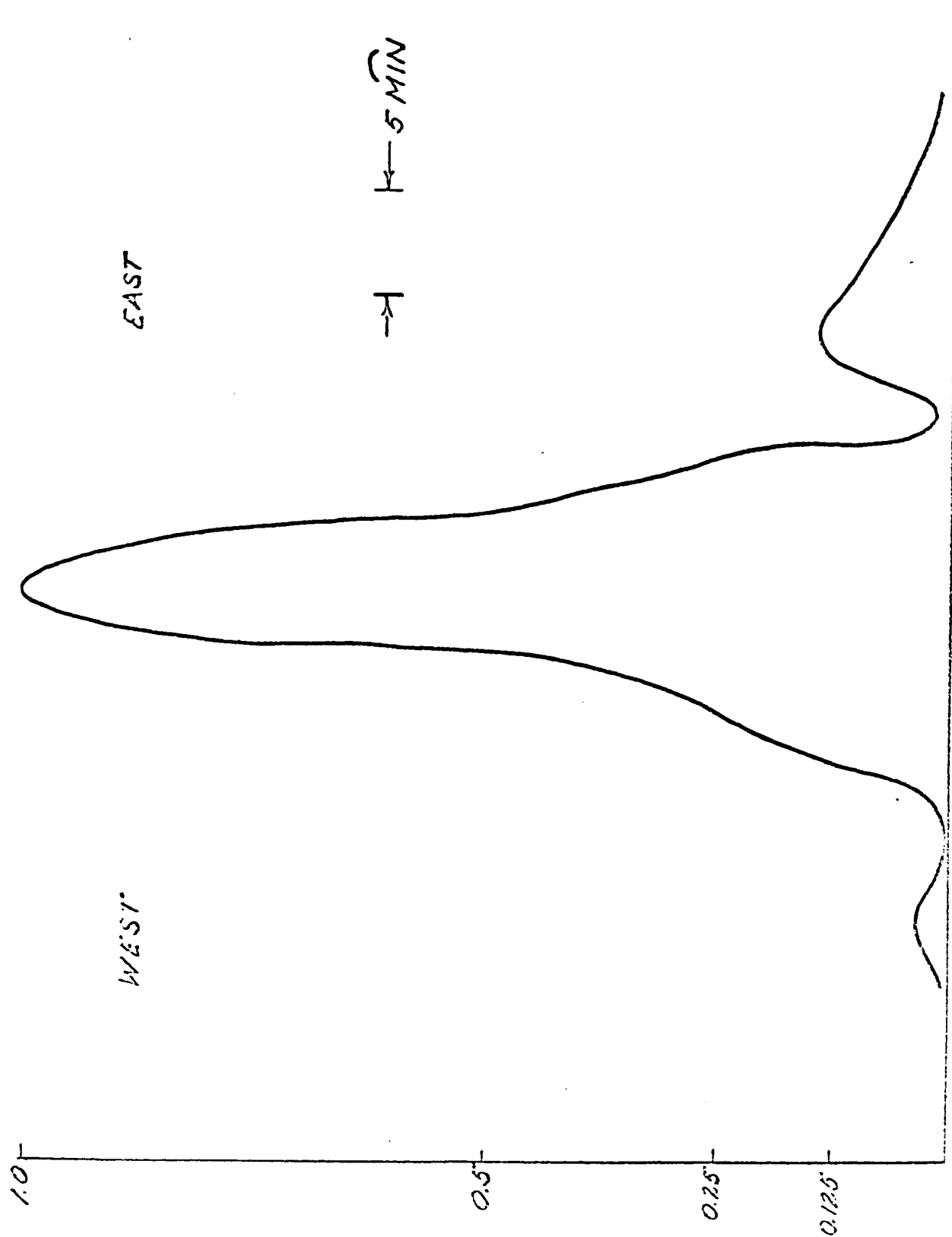


Fig. A-2(a) Antenna pattern in hour angle.

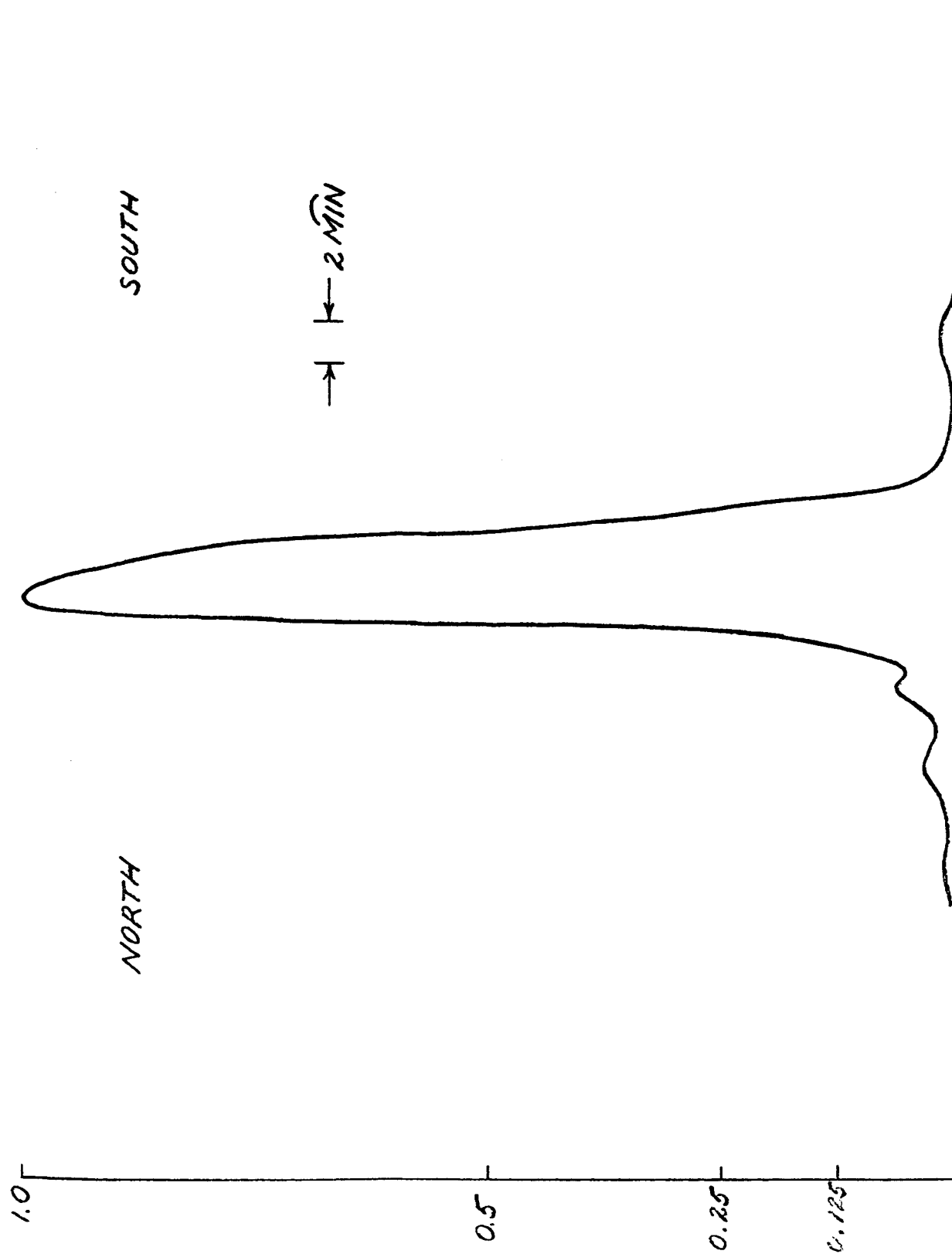


Fig. A-2(b) Antenna pattern in declination.

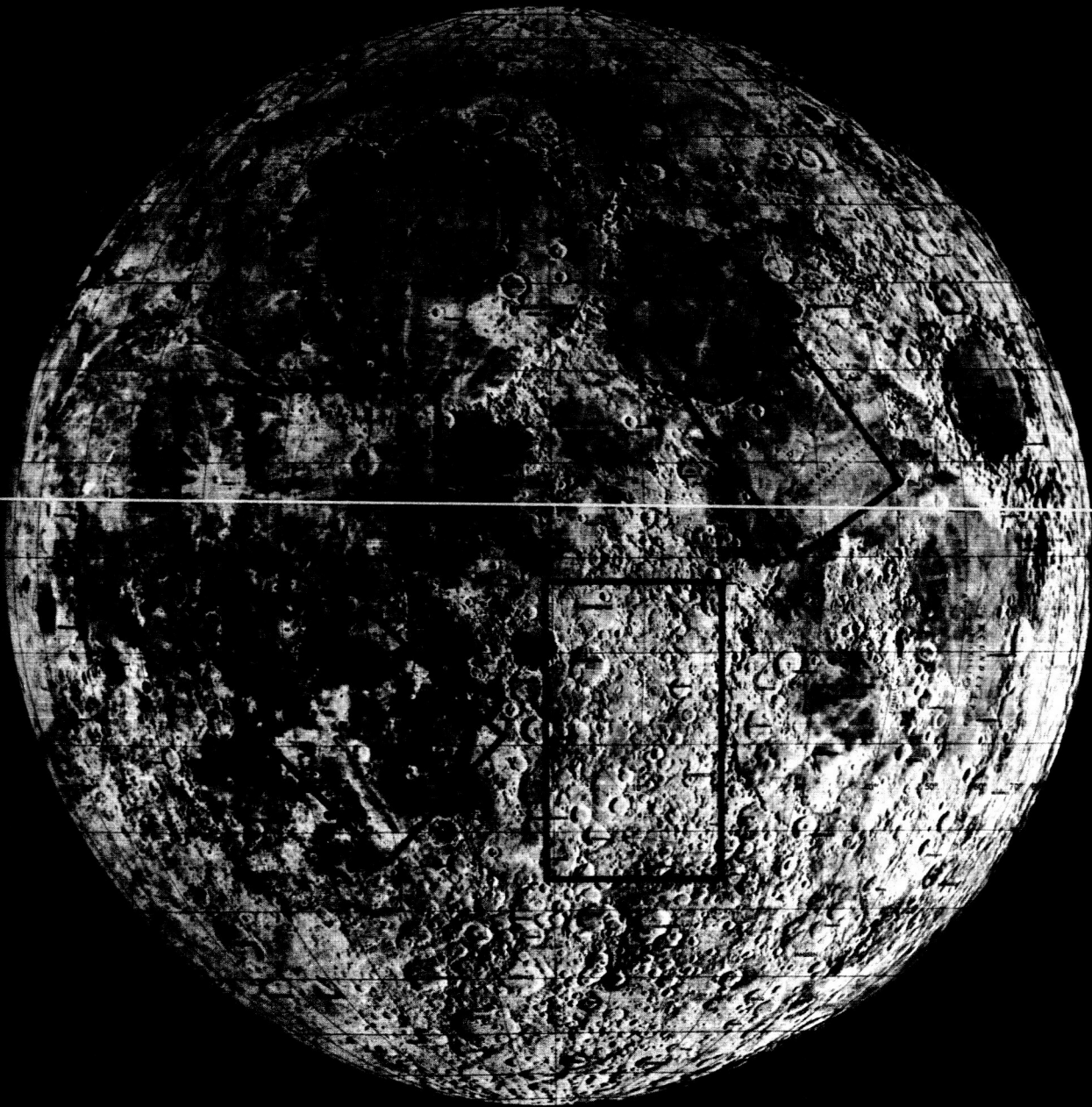


Figure A-3 The four regions of the lunar surface under consideration.

The resulting temperatures are shown in Table A-1. The temperatures listed are averages of temperatures between $\pm 10^\circ$ of phase angle; for example, the antenna temperature for 100° phase angle, say, is the average of temperatures obtained for phase angles between 90° and 110° . Also given in Table A-1 are the rms deviations from the mean and the number of values averaged.

The data from Table A-1 are shown graphically in Figure A-4 through Figure A-7; the curves drawn through the data points are visual best fits.

A.6 DATA INTERPRETATION

It is well known (Piddington and Minnet, 1949) that if the lunar surface is considered as a homogeneous semi-infinite solid with specific heat c , thermal conductivity, k , and density, ρ , independent of depth and temperature, then the microwave brightness temperature, $T_B(t)$, of a point of the surface, when observed at normal incidence can be written as:

$$T_B(t) = \sum_{n=0}^{\infty} T_n (1 + 2\delta_n + 2\delta_n^2)^{-\frac{1}{2}} \cos(\omega_n t - \epsilon_n - \varphi_n) \quad (A-1)$$

where the surface, or infrared temperature is given by:

$$T_{IR}(t) = \sum_{n=0}^{\infty} T_n \cos(\omega_n t - \epsilon_n) \quad (A-2)$$

The parameters in Equation (A-1) are related to the thermal and electrical properties of the lunar surface material as follows:

$$\begin{aligned} \omega_n &= 2\pi n/P \\ P &= \text{lunar period} \\ \delta_n &= \beta_n / \alpha \\ \alpha &= \text{microwave attenuation coefficient} \\ \beta_n &= \left(\frac{\omega_n \rho c}{2K} \right)^{1/2} \\ \tan \varphi_n &= \delta_n / (1 + \delta_n) \end{aligned}$$

As can be seen from Equation A-1, the microwave brightness temperature excursions during a complete lunation are less than the corresponding infrared temperatures, and the time of maximum brightness temperature occurs after full moon. More precisely, the amplitude of

the n^{th} harmonic of the microwave temperature is less than the corresponding harmonic of the infrared temperature by the factor $(1 + 2\delta_n + 2\delta_n^2)^{-1/2}$, and the phase angle of the n^{th} harmonic of the microwave temperature, measured from the corresponding infrared harmonic, is $\arctan [\delta_n / (1 + \delta_n)]$.

The homogeneous model places two rather severe general restrictions of the behavior of the microwave brightness temperature with phase angle. First, the phase angles, φ_n , of any of the harmonics cannot exceed 45° , and second, the time average or constant component of the microwave temperature must be identically equal to the average of the surface, or infrared temperature. Any experimental deviations from these two facts would indicate nonhomogeneity of the surface material.

Now, the infrared temperature has not been determined accurately during a complete lunation for any region of the lunar surface, primarily because of the extremely low temperatures during the lunar night. However, from theoretical considerations (Krotikov and Troitskii, 1964), and indeed from intuition, the infrared radiation originates from the uppermost top surface layers and should be nearly independent of the thermal properties of the surface material. Therefore, the infrared temperature should be, except for local changes in surface emissivity, practically the same everywhere on the lunar surface. In view of these considerations, and because the microwave spatial resolution is relatively poor compared to that possible in the infrared, Equation (A-2) will be assumed for the purpose of analysis, as representing the theoretical curve of Krotikov and Troitskii, for $(k \epsilon c)^{-1/2}$ approximately 1200, which is shown in Figure A-8. Figure A-8 was enlarged and harmonically analyzed by means of a mechanical analog harmonic analyzer with the results shown in Table A-2. By means of repeated measurements on a known waveform, the accuracy of the harmonic analyzer itself was found to be good to four significant figures; however, harmonics higher than the fifth were not considered meaningful.

Interpretation of the microwave observations from Equation (A-1) cannot yet be done, however, since the observed temperatures are the result of an average over a large range of phase angles by the antenna pattern. To illustrate this effect, the relative pattern in terms of longitude from Capernicus is shown in Figure A-9; the antenna response is treated as zero beyond the edges of the disk since there is no contribution to the antenna temperature beyond those points.

By a harmonic analysis technique developed in the Appendix I, it is shown that harmonic analysis of both the hour angle antenna pattern (projected on the lunar surface) and the antenna temperatures permits calculation of the harmonic amplitudes of the actual brightness temperature curve as a function of local phase angle.

Figures A-4 through A-7 were enlarged to about 5 inches amplitude for improved harmonic resolution. The hour angle antenna pattern was also enlarged and projected on the lunar surface and centered on each of the four regions under consideration. These eight curves were then harmonically analyzed and Equations (I-15) of the Appendix used to calculate the first five harmonics of the average brightness temperature of each of the four regions with the results shown in Table A-3.

A.7 CONCLUSIONS

A casual inspection of Figures A-4 through A-7 does not reveal any major differences in the thermal behavior of the four regions, with the possible exception of the mountainous region; on the other hand, the harmonic content of the curves differ appreciably. Because of the experimental uncertainties, the actual significance of the higher harmonics, as determined by the harmonic analyzer, is most certainly questionable. Whether or not the different harmonic content does indeed indicate different thermal properties has not yet been determined.

Simple calculations, based on the homogeneous model, show that the harmonic amplitudes are inconsistent with their corresponding phase angles; in general, they are smaller than predicted by Equation (A-1) and Equation (A-2). Furthermore, the phase angles, ϕ_n , clearly are not confined to values less than 45° ; this coupled with the fact that the average values are all less than the infrared average value, could be interpreted as evidence of nonhomogeneity in the surface material.

In order to discuss the results more quantitatively, some consideration of the effects of a layered structure can be made. Consider the lunar surface as a semi-infinite solid with a homogeneous surface layer of thickness, l , covering a homogeneous though different subsurface. It is not difficult to show that the microwave time average temperature should be less than the infrared average temperature by the factor $\epsilon_1 [\epsilon_2 e^{-\alpha l} + (1 - e^{-\alpha l})]$ where ϵ_1 , and ϵ_2 are the microwave transmissivities at the surface and subsurface boundaries respectively, and α is the microwave attenuation coefficient of the layer. The reason for the factor ϵ_1 is clear. The term $\epsilon_2 e^{-\alpha l}$ represents that fraction of the microwave flux from the subsurface which penetrates the subsurface boundary and is subsequently attenuated by the layer, and the term $(1 - e^{-\alpha l})$ arises because of the thermal reradiation from the layer itself. If one chooses reasonable values for the boundary reflectivities, and speculates somewhat on a value for α , the total reduction could easily be 10%, which is approximately what is observed. Although the absolute values of the quoted temperatures are most certainly questionable, the observed differences between the microwave and infrared average values, if real, would be consistent with a layered structure.

From the standpoint of a two-layer structure, the experimental values for the phase angles also become more reasonable. Suppose the layer to be nearly transparent to microwave radiation and to serve only as a thermal blanket for the subsurface. The received microwave radiation is then the integrated flux from the subsurface, a region which from a microwave standpoint, is isolated from its heat source, the surface insulation. Thickening the layer would then have the effect of moving the heat source further from the regions being observed (since the layer is assumed transparent) thereby introducing more thermal delay in the layer. Therefore, the presence of the layer results in an additional phase angle that could be any value whatsoever depending upon the depth of the layer. A partially transparent surface layer, or layers, would result in phase angles whose values are not necessarily restricted to 45° , a result which agrees at least qualitatively, with the observed values.

It is not intended that these results and conclusions be considered definitive by any means. Because of the many approximations, assumptions, observational errors, inadequate spatial resolution, simple modelization, etc., the observations should be treated as exploratory

and the conclusions most preliminary. However, it is clear that even the gross structure of the lunar surface still remains in doubt. In fact, it is the author's opinion that the value of the observations lies mostly in the fact that they point out the need for more accurate, definitive measurements of lunar microwave temperatures with much improved resolution and pointing accuracy.

TABLE A-1
ANTENNA TEMPERATURES
(corrected for losses)

T_A °K	phase angle	T_{rms} °K	number of measurements	T_A °K	phase angle	T_{rms} °K	number of measurements.
Copernicus				Mare Serenitatis			
172	0	3.9	15	172	0	6.0	10
173	20	3.4	14	175	20	5.5	8
177	40	3.4	17	168	40	6.2	4
173	60	5.1	15	167	60	4.6	9
168	80	3.4	18	156	80	4.6	10
155	100	5.6	13	161	100	2.8	12
151	120	3.9	18	158	120	4.7	9
146	140	2.4	20	146	140	2.3	4
141	160	4.4	27	146	160	1.9	8
138	180	3.8	17	141	180	3.0	8
139	200	2.8	10	134	200	4.5	15
134	220	3.6	23	134	220	4.0	14
134	240'	2.8	24	134	240	1.6	7
136	260	2.2	24	131	260	2.8	10
144	280	3.4	19	136	280	2.0	13
150	300	4.2	18	143	300	4.2	11
163	320	3.0	16	146	320	6.9	9
173	340	4.3	21	155	340	6.5	8
Mountainous Region				Mare Nubium			
173	0	4.8	15	173	0	5.3	16
177	20	5.3	11	177	20	2.9	13
177	40	5.2	21	172	40	5.0	22
170	60	4.8	16	177	60	4.6	22
170	80	5.9	21	173	80	5.2	12
163	100	5.0	16	161	100	2.3	10
156	120	5.1	11	153	120	4.1	16
155	140	5.0	10	150	140	3.9	21
144	160	4.7	20	143	160	4.2	26
144	180	3.5	21	141	180	3.6	21
139	200	4.3	27	139	200	2.7	18
139	220	3.4	23	139	220	4.2	22
136	240	3.8	21	136	240	4.1	24
136	260	3.6	21	136	260	2.9	13
138	280	5.0	27	141	280	4.2	14
150	300	4.0	25	153	300	6.6	15
158	320	5.1	20	163	320	3.9	15
170	340	5.6	21	172	340	4.8	12

TABLE A-2

INFRARED TEMPERATURE

$$\sum_{n=0}^{\infty} T_n \cos(\omega_n t + \epsilon_n)$$

n	T _n °K	n degrees
0	218	-
1	173	-1.2
2	34	11
3	33	180
4	13	-165
5	17	0

TABLE A-3

MICROWAVE TEMPERATURES

$$\sum_{n=0}^{\infty} (1 + 2\delta_n + 2\epsilon_n^2)^{-1/2} T_n \cos(\omega_n x + \epsilon_n + \varphi_n)$$

T_n °K	$\epsilon_n + \varphi_n$ degrees	n	T_n °K	$\epsilon_n + \varphi_n$ degrees	φ_n degrees
Copernicus					
153	-	0	215	-	-
23	-34	1	36	-33	-32
1.2	-29	2	2.1	-36	-47
2.0	68	3	3.8	68	-112
0.1	-90	4	0.3	-90	75
0.6	-200	5	1.7	-201	-201
Mare Nubium					
155	-	0	205	-	-
22	-36	1	33	-33	-32
1.8	-33	2	1.9	-36	-47
1.9	-255	3	3.9	-255	-175
0.3	-210	4	0.3	-183	-18
0.6	70	5	1.6	70	70
Mountainous Region					
153	-	0	176	-	-
21	-41	1	27	-37	-36
2.5	3	2	4.2	6	-5
1.0	79	3	2.2	75	-105
0.1	-243	4	0.1	-259	-194
0.1	-90	5	0.3	-102	-102
Serenitatis					
149	-	0	191	-	-
22	-45	1	32	-42	-41
3.3	-52	2	6.3	-60	-71
1.6	16	3	3.7	0	-18
1.0	-15	4	2.7	-34	131
0.2	-45	5	1.6	-81	-81

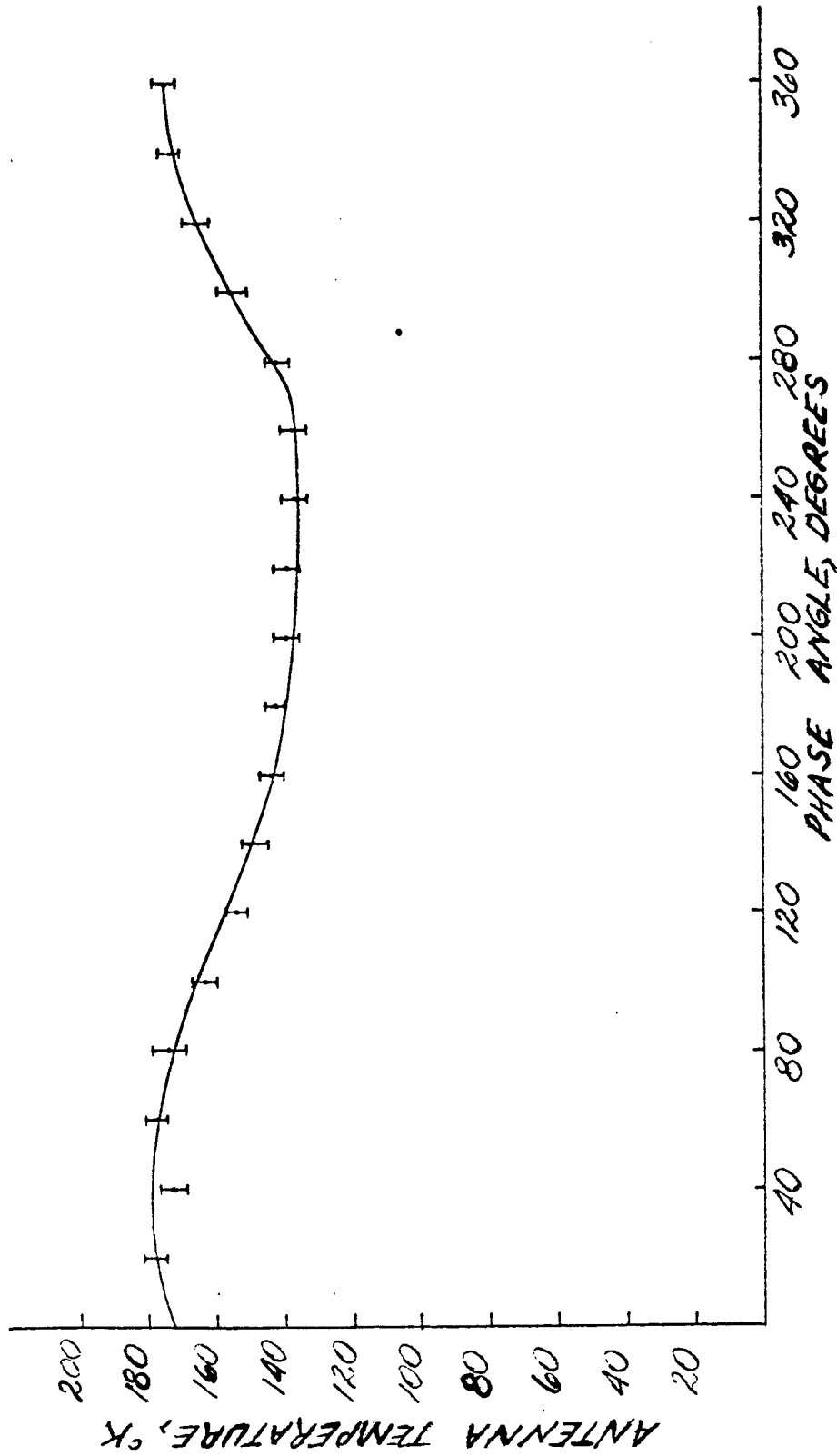


Fig. A-4 Antenna temperature as a function of local phase angle for the Copernicus region.

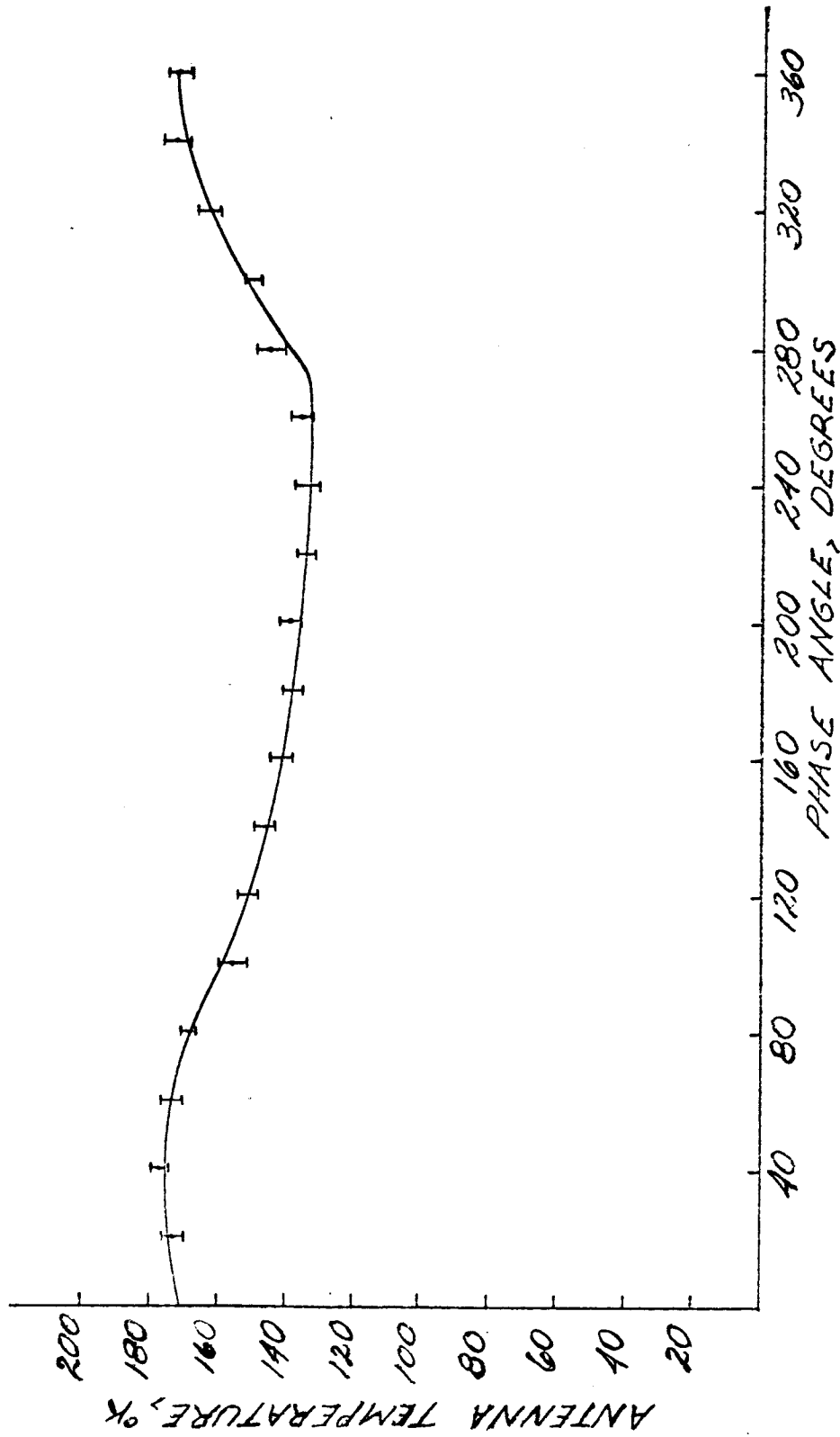


Fig. A-5. Antenna temperature as a function of local phase angle for the Mare Nubium region.

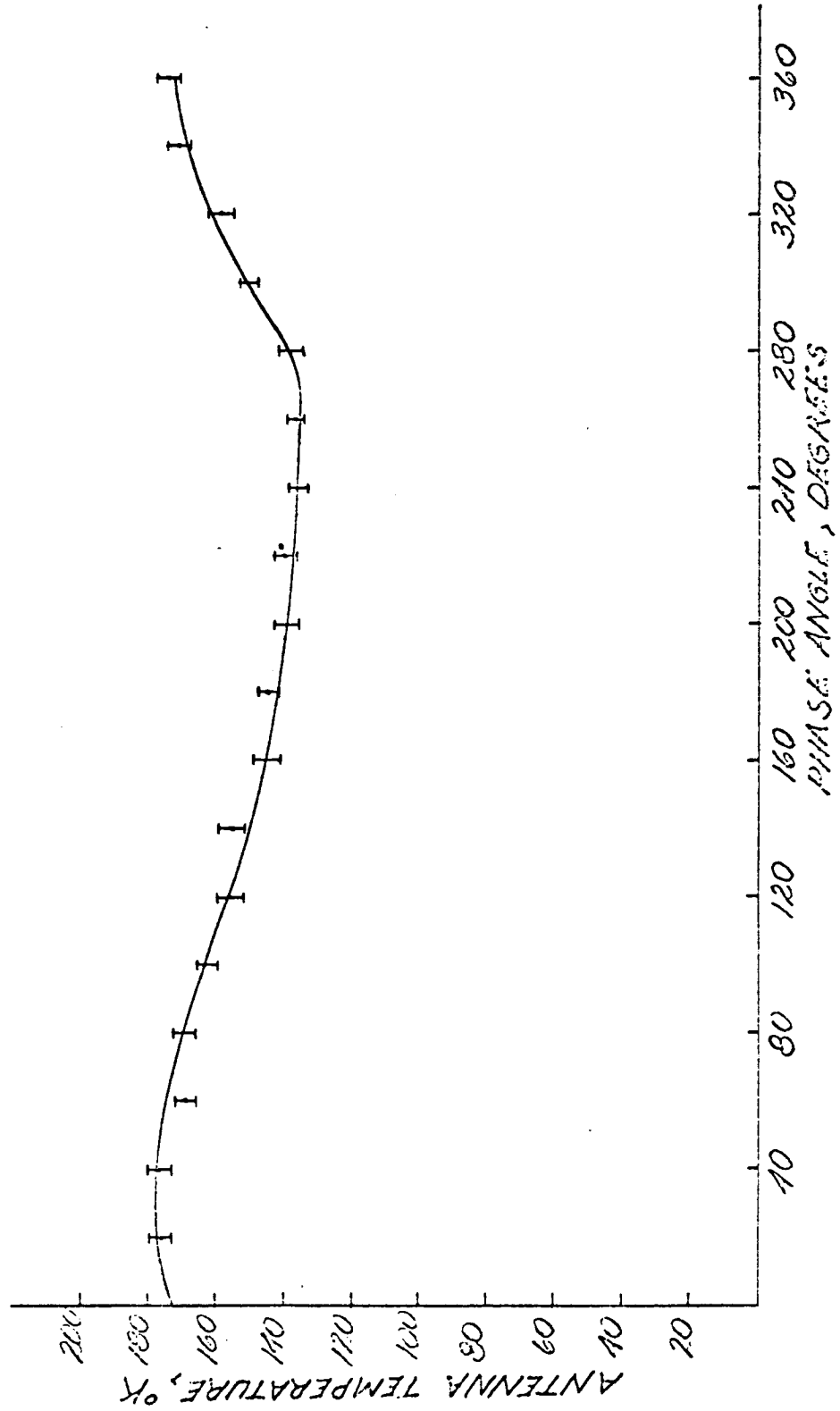


Fig. A-6. Antenna temperature as a function of local phase angle for the mountainous region.

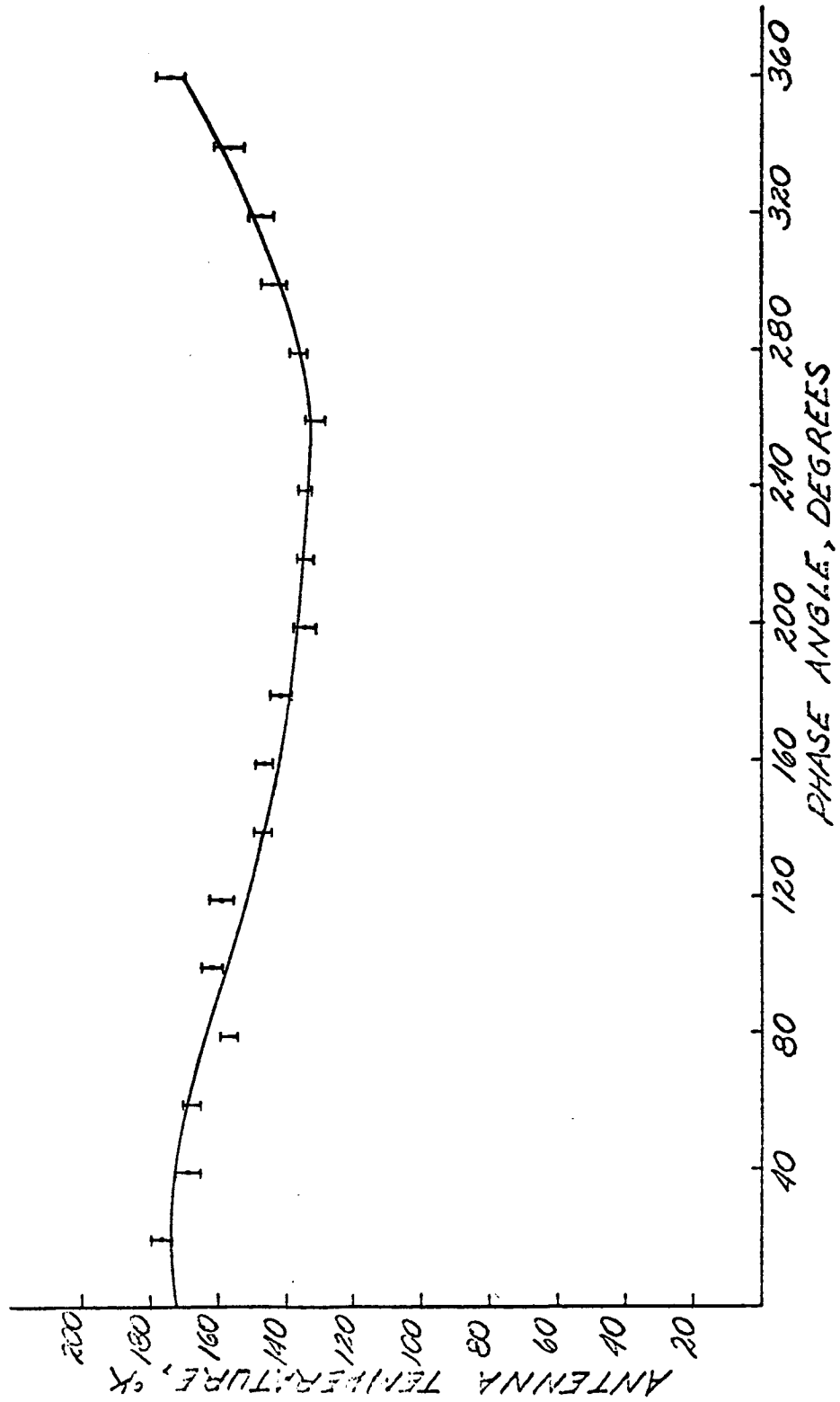


Fig. A-7 Antenna temperature as a function of local phase angle for the region of Maria Serenitatis and Tranquillitatis.

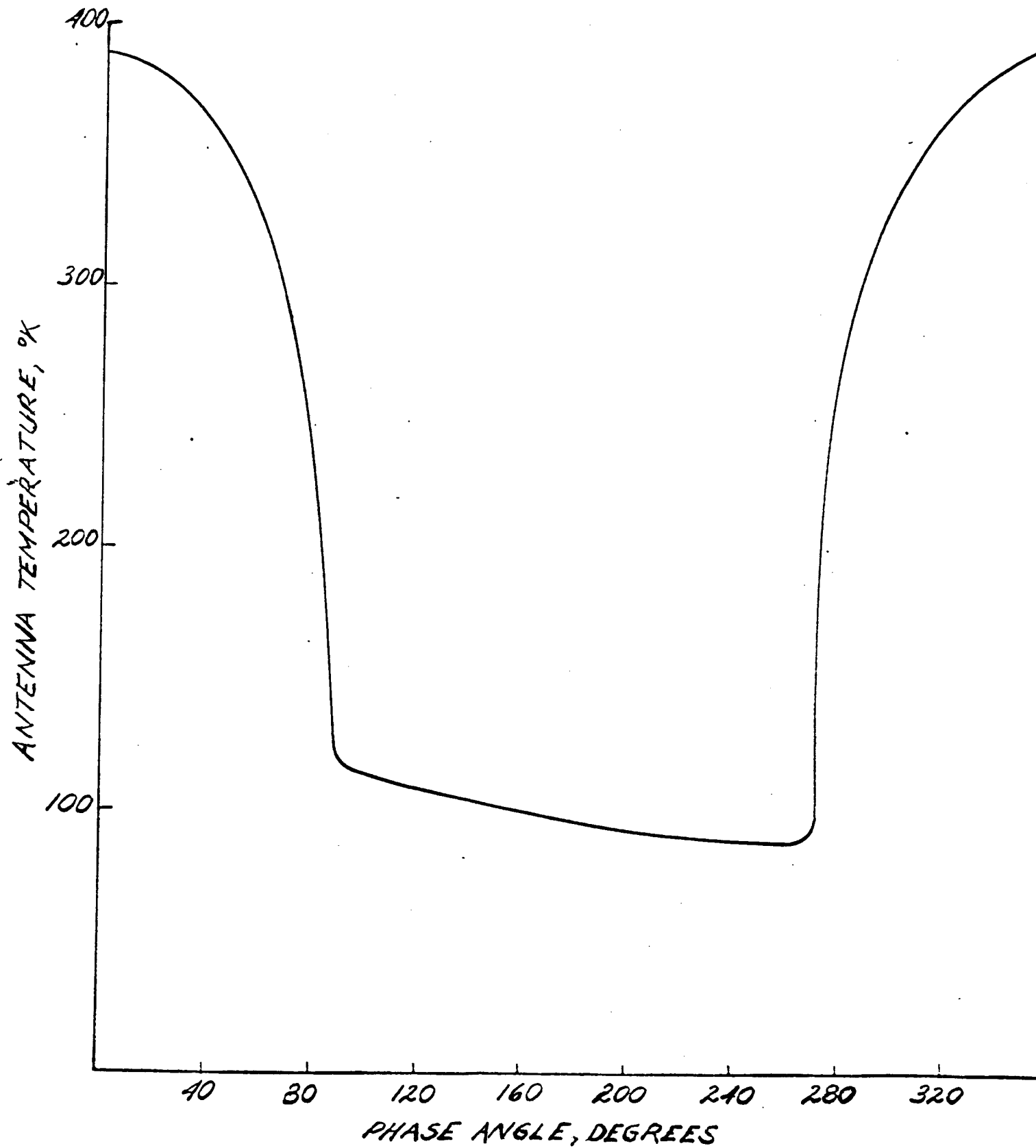


Fig. A-8 Theoretical infrared temperature as a function of phase angle for
 $(k p c)^{-1/2}$ approximately 1200.

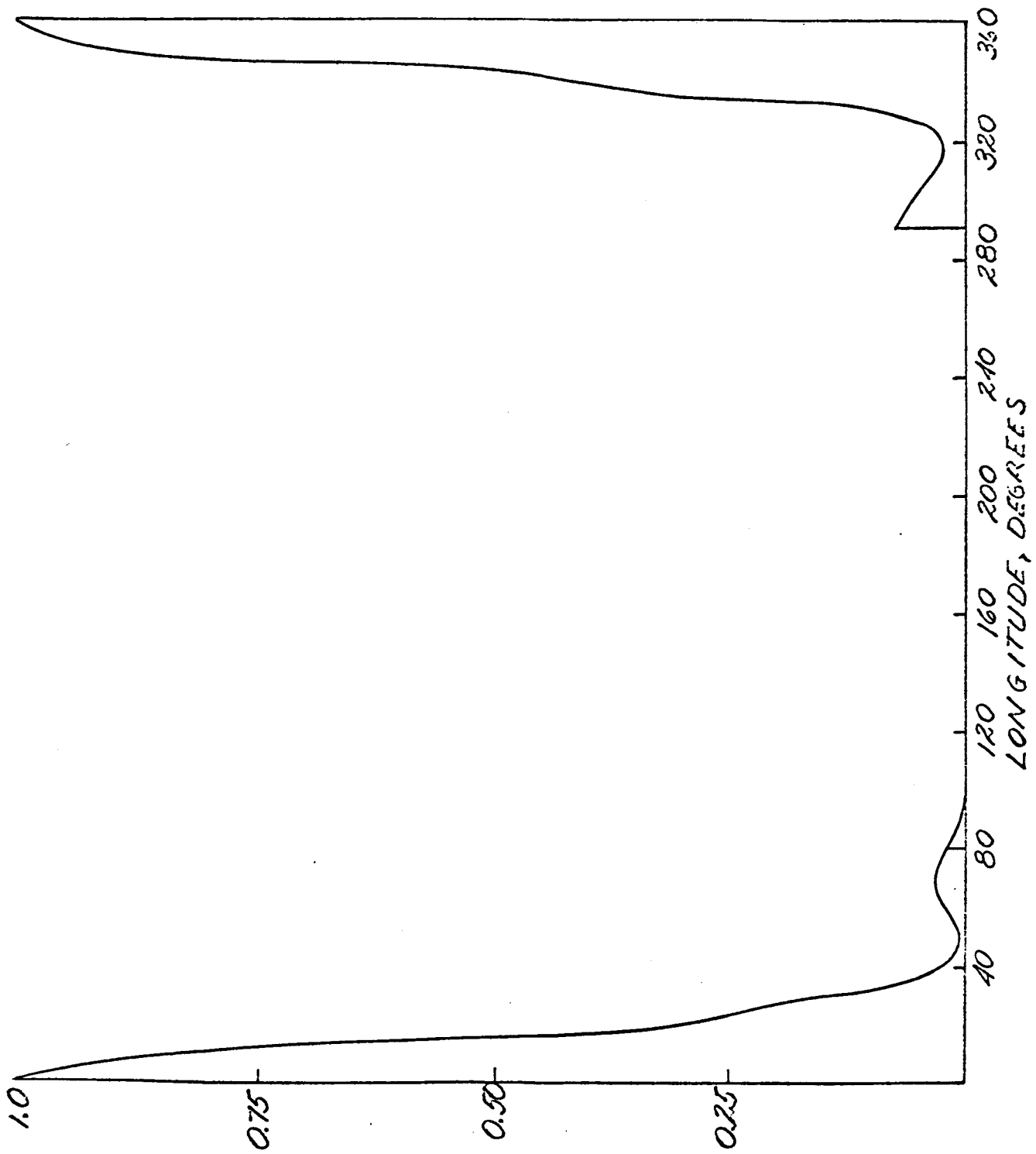


Fig. A-9. The hour angle antenna pattern projected on lunar surface and centered on the Copernicus region. The pattern is considered zero beyond the edges of the lunar disk.

ADDENDUM
SECTION A - PART I

CORRECTION PROCEDURE FOR ANTENNA SMOOTHING

Consider the antenna pointed near the sub-terrestrial point as illustrated in Figure 1-1, where the lunar disk and the two patterns in hour angle and declination are shown approximately to scale. The antenna temperature is given by:

$$T_A(t) = \frac{\iint_{\text{moon}} T_B(\nu, \varphi, t) F(\nu, \varphi) d\Omega}{\iint_{4\pi} F(\nu, \varphi) d\Omega} \quad (1-1)$$

where $T_B(\nu, \varphi, t)$ is the lunar brightness temperature as a function of time and the polar angles ν and φ , and $F(\nu, \varphi)$ is the normalized antenna pattern in two dimensions. Now, the antenna patterns were actually measured in a different coordinate system; i.e., in terms of the hour angle α , and declination, δ . The geometry is shown in Figure 1-2.

From Figure 1-2, it can be seen that the two coordinate systems are related by:

$$\begin{aligned} \tan \delta &= \tan \varphi \sin \nu \\ \tan \alpha &= \tan \varphi \cos \nu \end{aligned} \quad (1-2)$$

and the differential solid angle is:

$$d\Omega = \sin \varphi \, d\varphi \, d\nu \quad (1-3)$$

Because of the narrow beamwidth, the range of angle through which the patterns can be measured is small. Under this condition, Equation (1-2) and Equation (1-3) become:

$$\begin{aligned} \delta &\approx \varphi \sin \nu \\ \alpha &\approx \varphi \cos \nu \\ d\Omega &\approx \varphi \, d\varphi \, d\nu \end{aligned} \quad (1-4)$$

Now, the transformation between the two coordinate systems is identical to the transformation from rectangular to plane polar coordinates with $d\varphi$ playing the role of an element of area. Therefore, the element of solid angle can be approximated by:

$$d\Omega \approx d\alpha \, d\delta \quad (1-5)$$

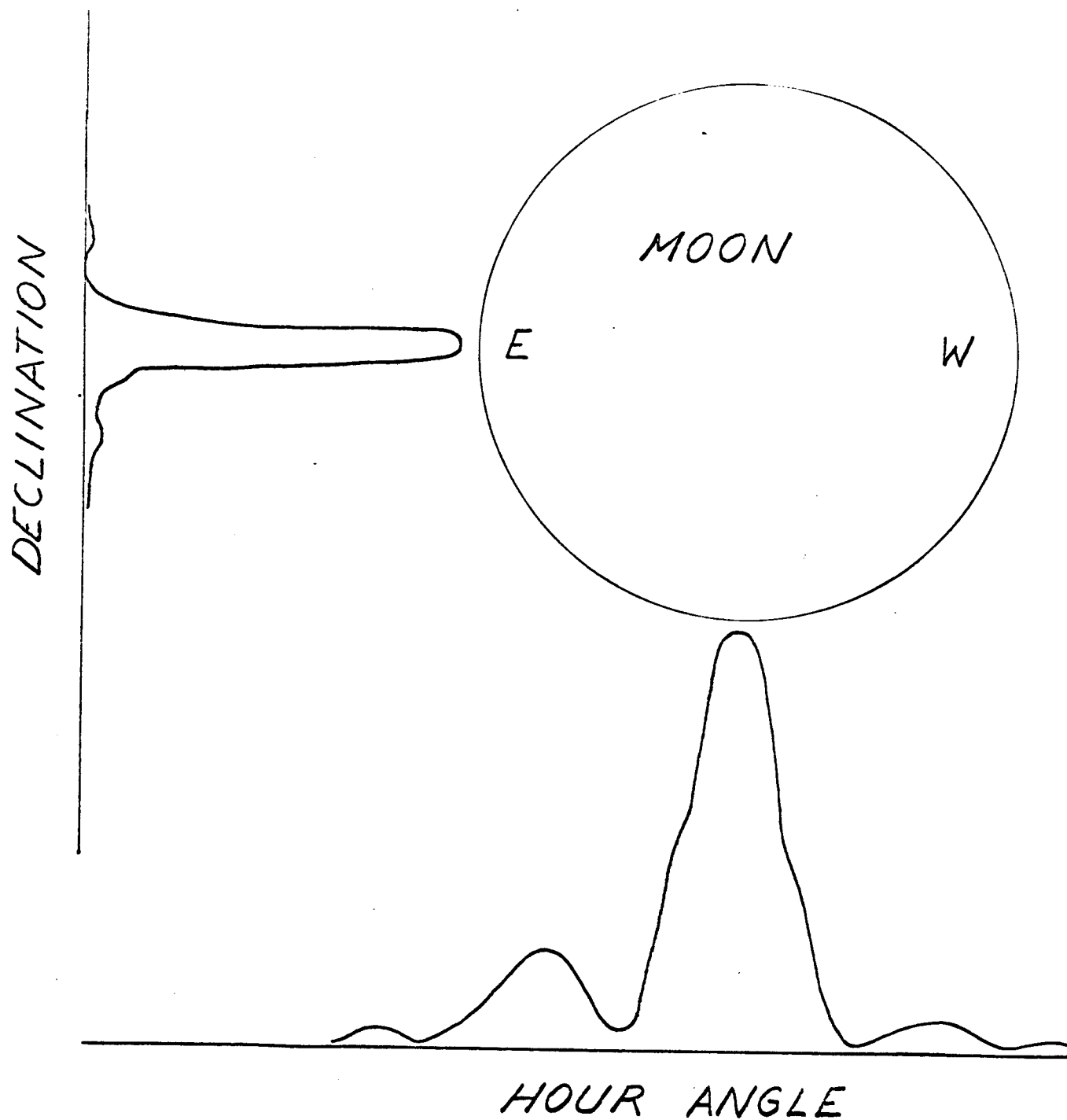


Fig. 1-1. A sketch illustrating the approximate relative sizes of patterns and the lunar disk.

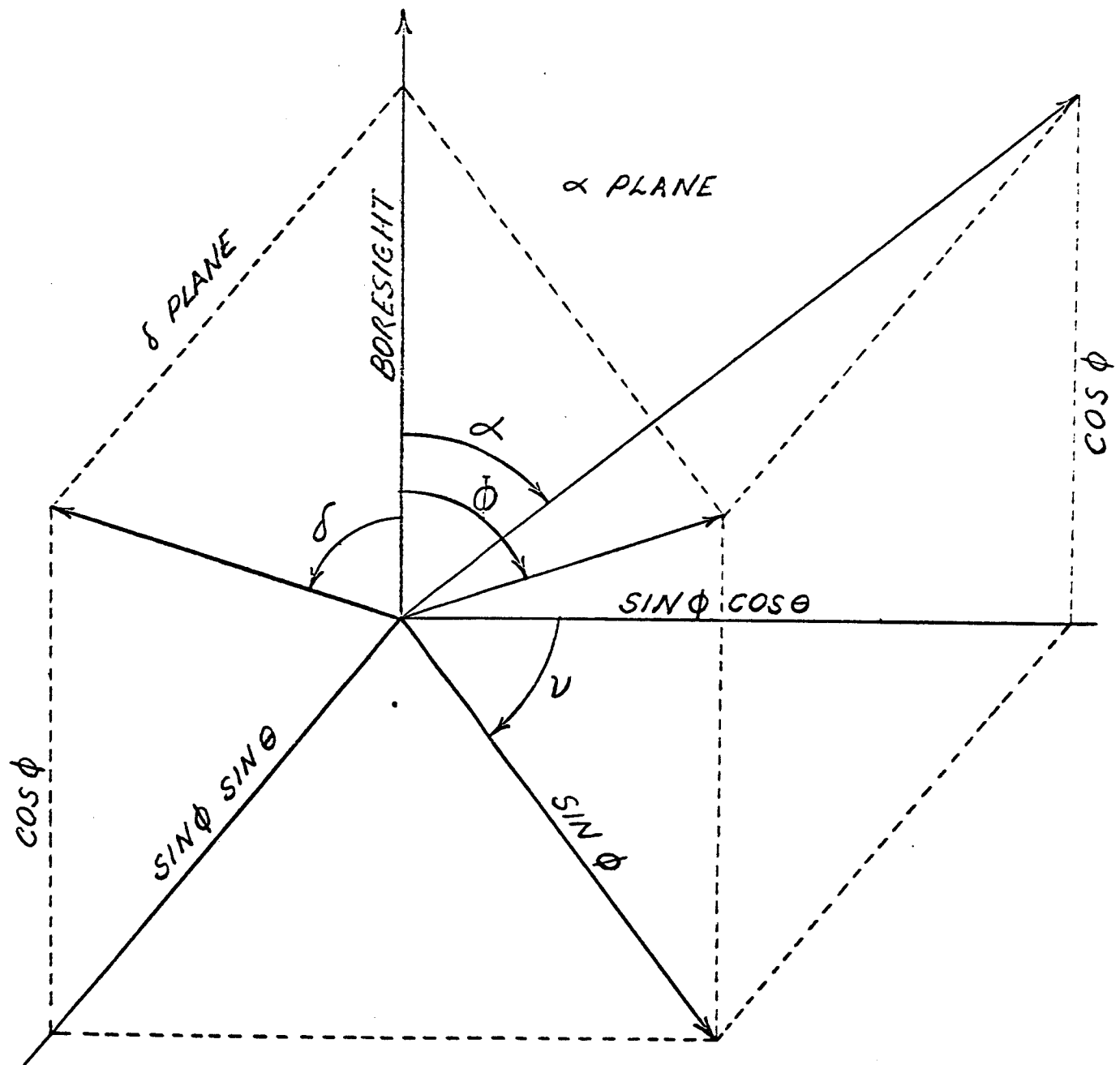


Fig. 1-2 . The geometry of the coordinate transformation.

Equation (1-1) can now be written as:

$$T_A(t) = \frac{\iint_{\text{moon}} T_B(\alpha, \delta, t) G(\alpha, \delta) d\alpha d\delta}{\iint_{4\pi} G(\alpha, \delta) d\alpha d\delta} \quad (1-6)$$

where all quantities have been written as functions of the hour angle and declination. The complete pattern in either the (α, δ) or the (ν, φ) coordinates are not known; only the patterns in the α plane and the δ plane have been determined. Some assumption about the functional form of $G(\alpha, \delta)$ must be made.

Because of the lack of knowledge about the actual complete pattern in two dimensions, any one assumption is no more justifiable than any other; however, it is convenient to define $G(\alpha, \delta)$ as:

$$G(\alpha, \delta) = f(\alpha)g(\delta) \quad (1-7)$$

where $f(\alpha)$ and $g(\delta)$ are the antenna patterns in the α plane and δ plane respectively.

Equation (1-6) becomes:

$$T_A(t) = \frac{\iint_{\text{moon}} T_B(\alpha, \delta, t) f(\alpha)g(\delta) d\alpha d\delta}{\int_0^{2\pi} f(\alpha) d\alpha \int_0^{2\pi} g(\delta) d\delta} \quad (1-8)$$

The denominator of (1-8) is the product of the areas A_α and A_δ under the two patterns in hour angle and declination.

In the quantity $T_B(\alpha, \delta, t)$, the independent variables are not actually independent, since the coordinate (α, δ) corresponds to different points on the lunar surface at different times of the month, because of the rotation of the lunar polar axis with respect to lines of constant hour angle. If, however, this effect is neglected and the lunar meridian assumed parallel to hour angle lines, the angles α and δ correspond approximately to lunar longitude and latitude respectively, were the antenna patterns projected on the lunar disk. Because of the finite spatial resolution, this assumption is probably no more drastic than the assumption on $G(\alpha, \delta)$.

Now, $T_B(\alpha, \delta, t)$ is periodic with time and can be written in the form:

$$T_B(\alpha, \delta, t) = T_0(\alpha, \delta) + \sum_{h=0}^{\infty} T_h(\alpha, \delta) \cos[\omega_h t + \phi_h(\alpha, \delta)] \quad (1-9)$$

If only the constant term in (1-9) inserted into (1-8), the result is:

$$\begin{aligned}(T_A)_{avg} &\approx \frac{T_0}{A_A A_S} \int_{\text{moon}} f(\alpha) d\alpha \int_{\text{moon}} g(\delta) d\delta \\ &\approx \frac{T_0}{K}\end{aligned}\tag{1-10}$$

The constant term, $T_0(\alpha, \delta)$, has its origin deep beneath the lunar surface and should, therefore, be independent of spatial variation in the electrical and thermal properties of the surface material. Furthermore, $T_0(\alpha, \delta)$ does not depend strongly on lunar latitude and longitude (Salomonovich and Losovskii, 1963), perhaps as the square root of the cosine of the latitude. If the antenna is pointed reasonably near the center of the moon, then, Equation (1-10) can be approximated by:

$$\begin{aligned}(T_A)_{avg} &\approx \frac{T_0}{A_A A_S} \int_{\text{moon}} f(\alpha) d\alpha \int_{\text{moon}} g(\delta) d\delta \\ &\approx \frac{T_0}{K}\end{aligned}\tag{1-11}$$

where K is the ratio of the products of the areas under the antenna patterns to the product of the areas measured out the edges of the lunar disk. The quantity K is the factor that the antenna temperatures must be multiplied by to obtain the true brightness temperatures because of the fact that the antenna beam is not completely filled.

The development of a procedure for antenna smoothing correction is more difficult when all the terms in Equation (1-9) are considered. When the antenna is directed at some point on the lunar surface, the pattern averages over both latitude and longitude, the brightness temperatures of different regions at different phase angles. Furthermore, the coordinates, i.e., hour angle and declination, in which the antenna patterns were determined are not simply related to lunar longitude and latitude. However, when the extent of the hour angle pattern on the lunar surface and the method used to determine the position of the antenna relative to the edges of the lunar disk are considered, a rigorous treatment is not justified. In order to arrive at a reasonably simple analytical procedure, several approximations will be made.

First, because of the relatively narrow antenna pattern in declination, the brightness temperature will be assumed a function of lunar longitude only. Furthermore, the tilt of the lunar polar axis with respect to the meridian will be neglected and hour angle measured from the antenna boresight assumed synonymous with lunar longitude. With these assumptions, the problem is reduced to one dimension and the measured antenna temperature as a function of phase angle can be approximated as a convolution between the actual brightness temperature as a function of longitude and the antenna pattern projected upon the lunar surface.

Now, the microwave temperature of regions at different longitudes will, in general, be different functions of the local phase angle because of differing thermal and electrical

properties. However, from inspection of Figures A-4 through A-7, it appears that the thermal behavior of the four regions, each of which are in approximately four different quadrants, is nearly the same. If it is assumed for the purpose of the antenna smoothing correction alone that this is true, then the temperature distribution with longitude is to a first approximation, the same as the functional dependence of the temperature of each region on local phase angle.

If the brightness temperature with local phase angle is denoted by $T_B(\varphi)$, the antenna pattern projected on the lunar disk and centered on each of the four regions by $h(\varphi)$, and the antenna temperature as $T(\varphi)$, then:

$$T(\varphi) = \int_0^{2\pi} T_B(x) h(x-\varphi) dx \quad (1-12)$$

where:

$$\int_0^{2\pi} h(\varphi) d\varphi = K^{-1} \quad (1-13)$$

In order that Equation (1-11) still be true.

Now, let $T_B(\varphi)$, $T(\varphi)$, and $h(\varphi)$ be expanded in Fourier series as follows:

$$\begin{aligned} T(\varphi) &= \frac{A_0}{2} + \sum_{n=1}^{\infty} (A_n \cos n\varphi + B_n \sin n\varphi) \\ h(\varphi) &= \frac{C_0}{2} + \sum_{n=1}^{\infty} (C_n \cos n\varphi + D_n \sin n\varphi) \\ T_B(\varphi) &= \frac{E_0}{2} + \sum_{n=1}^{\infty} (E_n \cos n\varphi + F_n \sin n\varphi) \end{aligned} \quad (1-14)$$

When Equations (1-14) are inserted into Equation (1-12), the cross-product terms, formed from term by term multiplication of the two series in the integrand, average to zero and all that remains is:

$$\frac{\pi}{2} E_0 C_0 + \pi \sum_{n=1}^{\infty} [E_n (C_n \cos n\varphi - D_n \sin n\varphi) + F_n (C_n \sin n\varphi + D_n \cos n\varphi)]$$

Upon equating coefficients and invoking Equation (1-13) one obtains:

$$E_o = K A_o$$

$$E_n = K C_o \frac{C_n A_n - B_n D_n}{C_n^2 + D_n^2} \quad (1-15)$$

$$F_n = K C_o \frac{A_n D_n + C_n B_n}{C_n^2 + D_n^2}$$

SECTION A - PART I

THERMAL RADIATION FROM THE MOON AT 8.6 MM WAVELENGTH

REFERENCES

- Barrett, A.H., and Chung, V.K., 1962, J. Geophys. Res., 67, 11.
- Gibson, J.E., 1958, Proc. IRE, 46, 1.
- Jaeger, J.G., 1953, Aust. J. Phys., 6, 10.
- , 1959, Nature, 183, 1316.
- Jaeger, J.G., and Harper, A.F.A., 1950, Nature, 166, 1026.
- Krotikov, V.D., and Troitskii, V.S., 1964, Soviet Physics Uspekki, 6, 6.
- Levin, B. Yu., 1964, Soviet Astronomy, 7, 818.
- Meeks, M.L., and Lilley, A.E., 1963, J. Geophys. Res., 68, 6.
- Piddington, J.H., and Minnet, H.C., 1949, Aust. J. Sci. Res., A2, 63.
- Salomonovich, A.E., 1962, Soviet Astronomy, 6, 55.
- Salomonovich, A.E., and Ya Losovskii, B., 1963, Soviet Astronomy, 6, 6.
- Troitskii, V.S., 1962, Soviet Astronomy, 6, 51.
- , 1965, Soviet Astronomy, 8, 576.

N66-28657

SECTION B

A TWO-LAYER MODEL OF THE LUNAR SURFACE

N66 28657

ABSTRACT

SECTION B - PART 1

A TWO-LAYER MODEL OF THE LUNAR SURFACE

28257

A two layer model of the lunar surface is treated theoretically and an exact analytical solution is obtained for the microwave brightness temperature in terms of the periodic surface temperature. It is found that the time average of the microwave temperature is, even after correction for surface reflectivity, less than the time average of the surface temperature. Furthermore, if the surface layer can be assumed sensibly transparent, the phase lag of maximum microwave temperature behind full moon can be any value whatsoever depending on the thickness of the layer.

Author

TABLE OF CONTENTS

SECTION B

	<u>Page No.</u>
B. 1 INTRODUCTION	1
B. 2 ANALYSIS	1
B.2.1 General Solution	1
B.2.2 Transparent Surface Layer	6
B.2.3 Thin Semi-Transparent Surface Layers	7
B. 3 CONCLUSIONS	9
B.3.1 Transparent Surface Layer	9
B.3.2 Semi-Transparent Layer	9

B.1 INTRODUCTION

The nature of thermal radiation from the moon depends upon the wavelengths at which it is observed. The lunar surface material is opaque to radiation at infrared wavelengths, so that observations at those wavelengths yield the temperature of the outermost surface skin. However, the lunar surface is partially transparent to radiation of microwave wavelengths and measurements at these wavelengths necessarily give a weighted average temperature.

Early microwave measurements (Piddington and Minnet, 1949) soon revealed that a simple homogeneous model for the lunar surface could not adequately explain the observational results at both microwave and infrared wavelengths. It was generally agreed (Piddington and Minnet, 1949; Jaeger and Harper, 1950; Jaeger, 1953; Jaeger, 1959) that if the lunar surface were considered covered with a thin layer of poorly conducting material, the microwave and infrared results could be brought into close agreement. More recently, investigators in the Soviet Union (Troitskii, 1965; Salomovich, 1962; Troitskii, 1962; Krotikov and Troitskii, 1964) have concluded that the lunar surface is probably homogeneous to a depth of the order of meters, although there is some disagreement (Levin, 1964). It has been speculated that recent photographic evidence from the Ranger spacecrafts indicates, at least in a qualitative manner, that there exists a deep layer of porous material to depths of many feet.

Microwave observations of lunar thermal radiation cannot distinguish between the homogeneous model and a two layer model if the depth of the layer is large compared to the microwave penetration depth; however, the extent to which this is true depends upon the wavelength at which the measurements are made. Previous theoretical treatments of a two layer model considered the surface layer to be extremely thin, permitting the assumption of zero thermal capacity (Jaeger, 1953) or a constant thermal gradient independent of depth in the surface layer (Piddington and Minnet, 1948). It is instructive to consider the case where the depth of the layer is more arbitrary.

The analysis proceeds as follows: Solutions to the heat conduction equations for a homogeneous layer covering a homogeneous subsurface are found. Although the thermal and electrical parameters of the layer and subsurface most probably are functions of both depth and temperature, a prior knowledge of the actual functional dependence is, of course, unknown; therefore, they are assumed constant. The constants of integration are chosen so as to match the temperature and the thermal flux at the boundary between subsurface and layer. The expressions for the temperature as a function of depth and time for the subsurface and the layer are inserted in the equation of radiative transfer and the subsequent integration gives the microwave temperatures. The resulting expressions are quite complicated; two approximations are considered: (1) The surface layer is transparent to microwave radiation and serves only as a thermal blanket for the subsurface; (2) The surface is partially transparent to first order terms, and serves as both a thermal blanket and a source of microwave flux.

B.2 ANALYSIS

B.2.1 General Solution

Consider the lunar surface as a semi-infinite solid with a homogeneous surface layer, of thickness ℓ , covering a homogeneous, though different subsurface. Let the

depth, x , be measured positive inward. The specific heat, c , the thermal conductivity, k , and the density, ρ , are assumed independent of temperature and depth in each region. If there is no thermal resistance at the boundary between the layers, then the temperature in each region obeys the heat conduction equation:

$$\begin{aligned} K_1 \frac{\partial T_1(x,t)}{\partial t} &= \frac{\partial^2 T_1(x,t)}{\partial x^2} & 0 < x \leq l \\ K_2 \frac{\partial T_2(x,t)}{\partial t} &= \frac{\partial^2 T_2(x,t)}{\partial x^2} & x \geq l \end{aligned} \quad (B-1)$$

where the subscripts 1 and 2 refer to the layer and the subsurface respectively, and K has been written for $(\rho c/k)$. Possible internal sources of heat have been neglected.

Equation (B-1) will be solved with the aid of Laplace transforms. In the final result, the transient terms will be discarded and only the periodic part retained. Therefore, the initial temperatures are arbitrary and can be assumed to be zero for convenience.

The Laplace transform of $T_1(x, t)$ with respect to time is defined as:

$$T_1^*(x, s) = \int_0^{\infty} T_1(x, t) e^{-st} dt$$

with the same notation for T_2 .

The transformation of Equation (B-1) gives:

$$\begin{aligned} s K_1 T_1^*(x, s) &= \frac{\partial^2 T_1^*(x, s)}{\partial x^2} \\ s K_2 T_2^*(x, s) &= \frac{\partial^2 T_2^*(x, s)}{\partial x^2} \end{aligned} \quad (B-2)$$

where, as stated above,

$$T_1(x, 0) = T_2(x, 0) = 0$$

has been assumed.

The solution of Equation (B-2) is:

$$T_1^*(x, s) = A_1 e^{-x\sqrt{K_1 s}} + B_1 e^{x\sqrt{K_1 s}}$$

$$T_2^*(x, s) = A_2 e^{-x\sqrt{K_2 s}}$$

(B-3)

The arbitrary constants will be determined by three boundary conditions:

1. The two solutions, (B-3) should be the same at boundary:

$$T_1^*(l, s) = T_2^*(l, s)$$

2. The flux across the boundary $x = l$, as given by each solution should be equal:

$$k_1 \left[\frac{\partial T_1^*(x, s)}{\partial x} \right]_{x=l} = k_2 \left[\frac{\partial T_2^*(x, s)}{\partial x} \right]_{x=l}$$

3. The surface temperature is periodic with angular frequency ω :

$$T_1(0, t) = \sum_{n=0}^{\infty} (a_n \sin \omega_n t + b_n \cos \omega_n t)$$

$$T_1^*(0, s) = \sum_{n=0}^{\infty} \frac{a_n \omega_n + s b_n}{\omega_n^2 + s^2}$$

In boundary condition 3, $T_1(0, t)$ represents the infrared temperature written for form of a Fourier series; however, the summation sign, \sum , and the summation index, n , will be omitted for simplicity. It will be understood that, wherever the symbols a and b appear, they represent only one term of an infinite series which will be written as in the final result.

Application of the boundary conditions gives:

$$A_1 e^{-l\sqrt{k_1}s} + B e^{l\sqrt{k_1}s} = A_2 e^{-l\sqrt{k_2}s} \quad (B-4)$$

$$k_1 A_1 \sqrt{k_1} s e^{-l\sqrt{k_1}s} - k_1 B \sqrt{k_1} s e^{l\sqrt{k_1}s} = k_2 A_2 \sqrt{k_2} s e^{-l\sqrt{k_2}s} \quad (B-5)$$

$$A_1 + B = \frac{a\omega + bs}{\omega^2 + s^2} \quad (B-6)$$

Simultaneous solution of Equations (B-4), (B-5), and (B-6), to determine the constants yields:

$$A_1 = \frac{1}{2} \frac{a\omega + bs}{\omega^2 + s^2} \cdot \frac{(1 + \gamma_2/\gamma_1)e^{l\sqrt{K_1}s}}{(\gamma_2/\gamma_1)\cosh l\sqrt{K_1}s + \sinh l\sqrt{K_1}s} \quad (B-7)$$

$$B_1 = \frac{1}{2} \frac{a\omega + bs}{\omega^2 + s^2} \cdot \frac{(\gamma_2/\gamma_1)e^{-l\sqrt{K_1}s}}{(\gamma_2/\gamma_1)\cosh l\sqrt{K_1}s + \sinh l\sqrt{K_1}s} \quad (B-8)$$

$$A_2 = \frac{a\omega + bs}{\omega^2 + s^2} \cdot \frac{(\gamma_2/\gamma_1)e^{l\sqrt{K_2}s}}{(\gamma_2/\gamma_1)\cosh l\sqrt{K_2}s + \sinh l\sqrt{K_2}s} \quad (B-9)$$

where: $\gamma = (k p c)^{-1/2}$

Equation (B-3) finally becomes:

$$T_1^*(x, s) = \frac{a\omega + bs}{\omega^2 + s^2} \frac{(\gamma_1/\gamma_2)\sinh[(l-x)\sqrt{K_1}s] + \cosh[(l-x)\sqrt{K_1}s]}{(\gamma_1/\gamma_2)\sinh l\sqrt{K_1}s + \cosh l\sqrt{K_1}s}$$

$$T_2^*(x, s) = \frac{a\omega + bs}{\omega^2 + s^2} \frac{e^{(l-x)\sqrt{K_2}s}}{(\gamma_1/\gamma_2)\sinh l\sqrt{K_1}s + \cosh l\sqrt{K_1}s} \quad (B-10)$$

From the inversion theorem of the Laplace transformation, the inverse transform is given by:

$$T(x, t) = \frac{1}{2\pi i} \int_{\sigma - i\infty}^{\sigma + i\infty} T^*(x, s) e^{st} ds \quad (B-11)$$

where the integration is performed in the complex plane and σ is a positive constant. The integrands of (B-11) have branch points at $s = 0$ and simple poles at $s = \pm i\omega$.

When the integrals (B-11) are evaluated by contour integration in the usual way, the residues at the poles yield the desired steady state terms. The result is:

$$T_1(x, t) = \text{RE} \left\{ \frac{a+ib}{i} \frac{(\gamma_1/\gamma_2) \sinh[\beta_1(l-x)(1+i)] + \cosh[\beta_1(l-x)(1+i)]}{(\gamma_1/\gamma_2) \sinh[\beta_1 l(1+i)] + \cosh[\beta_1 l(1+i)]} e^{i\omega t} \right\}$$

$$T_2(x, t) = \text{RE} \left\{ \frac{a+ib}{i} \frac{e^{\beta_2(l-x)(1+i) + i\omega t}}{(\gamma_1/\gamma_2) \sinh[\beta_1 l(1+i)] + \cosh[\beta_1 l(1+i)]} \right\} \quad (\text{B-12})$$

where $\beta = \sqrt{1/2 K}$ and RE denotes the "real part of".

If advantage is taken of the fact that Equations (B-12) are the products of functions of x and functions of t , it is not difficult to show that they satisfy the differential Equation (B-11) and all three boundary conditions.

For normal incidence, the microwave brightness temperature is found by:

$$T_B(t) = \epsilon_1 \int_0^l \alpha_1 T_1(x, t) e^{-\alpha_1 x} dx + \epsilon_1 \epsilon_2 e^{-\alpha_1 l} \int_l^\infty \alpha_2 T_2(x, t) e^{-\alpha_2 (x-l)} dx \quad (\text{B-13})$$

where α is the microwave attenuation coefficient, and ϵ is the boundary transmissivity, i.e., the reflectivity subtracted from unity.

Evaluation of the integrals (B-13) gives:

$$T_B(t) = \text{RE} \left[\frac{\alpha_1 \epsilon_1 (a+ib) e^{i\omega t}}{i(2i\beta_1^2 - \alpha_1) \{ (\gamma_1/\gamma_2) \sinh[\beta_1 l(1+i)] + \cosh[\beta_1 l(1+i)] \}} \right. \\ \times \left\{ \left[\beta_2(1+i) - \alpha_1 (\gamma_1/\gamma_2) \right] \sinh[\beta_1 l(1+i)] + \left[(\gamma_1/\gamma_2) \beta_1(1+i) - \alpha_1 \right] \left\{ \cosh[\beta_1 l(1+i)] - e^{-\alpha_1 l} \right\} \right\} \\ \left. + \frac{\epsilon_1 \epsilon_2 \alpha_2 (a+ib) e^{-\alpha_1 l + i\omega t}}{i[\beta_2(1+i) - \alpha_2] \{ (\gamma_1/\gamma_2) \sinh[\beta_1 l(1+i)] + \cosh[\beta_1 l(1+i)] \}} \right] \quad (\text{B-14})$$

The first term gives the contribution to $T_B(t)$ from the layer, and the second term the contribution from the subsurface. The extraction of the real part of Equation (B-14) is a tedious process. It is prudent at this point to consider some approximations.

B.2.2 Transparent Surface Layer

The simplest approximation is to assume that the layer is transparent to microwave radiation and serves only as a thermal blanket for the subsurface. In this case, the first term of Equation (B-14) vanishes. The second term becomes, after considerable reduction.

$$T_{B2}(t) = \sum_{n=0}^{\infty} \epsilon_2 \left[\frac{a_n^2 + b_n^2}{1 + 2\delta_{n2} + 2\delta_{n2}^2} \right]^{1/2} \cos(\omega_n t - \xi_n - \Theta_n - \varphi_n)$$

$$\times \left\{ \left[\cosh \beta_{n1} l + (\gamma_1/\gamma_2) \sinh \beta_{n1} l \right]^2 \cos^2 \beta_{n1} l + \left[(\gamma_1/\gamma_2) \cosh \beta_{n1} l + \sinh \beta_{n1} l \right]^2 \sin^2 \beta_{n1} l \right\}^{-1/2} \quad (B-15)$$

where:

$$\delta_{n2} = \beta_{n2}/\alpha_2 \quad \tan \xi_n = a_n/b_n \quad \tan \Theta_n = \delta_{n2}/(1 + \delta_{n2})$$

$$\tan \varphi_n = \tan \beta_{n1} l \frac{(\gamma_1/\gamma_2) \cosh \beta_{n1} l + \sinh \beta_{n1} l}{\cosh \beta_{n1} l + (\gamma_1/\gamma_2) \sinh \beta_{n1} l}$$

and the summation over all harmonics is now indicated.

As can be seen, Equation (B-15) reduces to the well known expression for the homogeneous model for $l = 0$.

If the surface layer is thin, $T_{B2}(t)$ becomes, to first order in the arguments of the hyperbolic and circular functions,

$$T_{B2}(t) = \sum_{n=0}^{\infty} \frac{\epsilon_2 (a_n^2 + b_n^2)^{1/2} \cos(\omega_n t - \xi_n - \Theta_n - \varphi_n)}{(1 + 2\delta_{n2} + 2\delta_{n2}^2)^{1/2} (1 + 2\delta_{n1} + 2\delta_{n1}^2)^{1/2}} \quad (B-16)$$

and φ_n is now given by $\delta_{n1}/(1 + \delta_{n1})$, where $\delta_{n1} = \beta_{n1} l (\gamma_2/\gamma_1)$

The second order term $2\delta_{n1}^2$ should be discarded to be consistent with the approximation; however, it was intentionally retained in order that an expression in the same functional form as that given by Krotikov and Troitskii (1964) could be developed. The results agree except that the factor (γ_2/γ_1) in δ_{n1} is replaced by $(\gamma_2/\gamma_1)^2$.

B.2.3 Thin Semi-Transparent Surface Layers

The next logical extension of the problem is to assume that the surface layer is thin and only partially transparent to microwave radiation. The first term of Equation (B-14) becomes, to first order terms in the exponential and hyperbolic functions,

$$T_{B1}(t) = \text{RE} \left\{ \frac{\epsilon_1 \alpha_1 (a + ib) \left\{ [\beta_1 l (1+i) - (\gamma_1/\gamma_2) \alpha_1] [\beta_1 l (1+i)] + [(\gamma_1/\gamma_2) (1+i) \beta_1 - \alpha_1 l] \right\}}{i (z i \beta_1^2 - \alpha_1^2) [1 + (\gamma_1/\gamma_2) (1+i) \beta_1 l]} e^{i \omega t} \right\}$$

$$= \frac{\alpha_1 \epsilon_1 l (a^2 + b^2)^{1/2}}{(1 + 2\delta_1 + 2\delta_1^2)^{1/2}} \cos(\omega t - \xi - \varphi) \quad (\text{B-17})$$

Therefore, Equation (B-14) becomes, including all harmonics:

$$T_B(t) = \sum_{n=0}^{\infty} \left[\frac{\epsilon_1 (a_n^2 + b_n^2)}{1 + 2\delta_{n1} + 2\delta_{n1}^2} \right]^{1/2} \left[\frac{\epsilon_2 \cos(\omega_n t - \xi_n - \varphi_n)}{(1 + 2\delta_{n2} + 2\delta_{n2}^2)^{1/2}} + \alpha_1 l \cos(\omega_n t - \xi_n - \varphi_n) \right]$$

(B-18)

If the two terms in (B-17) are combined, the result is, to first order terms in α, l :

$$T_B(t) = \sum_{n=0}^{\infty} \epsilon_1 (a_n^2 + b_n^2)^{1/2} \left[\frac{\epsilon_2^2 + 2\alpha_1 \epsilon_2 l (1 + \delta_{n2} - \epsilon_2)}{(1 + 2\delta_{n1} + 2\delta_{n1}^2)(1 + 2\delta_{n2} + 2\delta_{n2}^2)} \cos(\omega_n t - \xi_n - \varphi_n - \psi_n) \right]$$

(B-19)

where:

$$\tan \varphi_n = \frac{\epsilon_2 \delta_{nz} (1 - \alpha_{,l})}{\epsilon_2 (1 + \delta_{nz}) + \alpha_{,l} [1 + 2\delta_{nz} + 2\delta_{nz}^2 - \epsilon_2 (1 + \delta_{nz})]}$$

B.3 CONCLUSIONS

B.3.1 Transparent Surface Layer

For the case of a transparent surface layer, the phase angle θ has the limiting value $\pi/4$ as in the homogeneous model. However, because of the factor $\beta_n l$ in Equation (B-15), the presence of the layer results in an additional angle φ_n which, may have any value whatsoever depending upon the thickness of the layer. This is as it should be. The microwave flux is the integrated flux from a region which, from a microwave standpoint, is isolated from its source of heat, the surface. Thickening the layer has the effect of moving the heat source further from the region that is actually observed, thereby introducing more thermal delay in the layer.

The effect of the thermal blanket on the phase angle can be appreciable. A layer of thickness comparable to the thermal wavelength, β_1 , although this stretches the assumption of transparency somewhat, results in a phase angle, φ_1 , of 60° .

In general, the presence of a layer that is reasonably transparent to microwaves will cause the maximum microwave temperature to lag behind full moon by an amount which can be appreciably larger than that predicted by a homogeneous model.

B.3.2 Semi-Transparent Layer

The most interesting result for the case of a semi-transparent layer is that the time average microwave temperature, even when corrected for surface reflectivity, is less than the average surface temperature.

This result can be arrived at more directly by inserting only the constant terms from Equation (B-12) into (B-13). The constant component of the microwave temperature is found to be less than average surface temperature by the factor:

$$\Delta = \epsilon_1 \left[\epsilon_2 e^{-\alpha_2 l} + (1 - e^{-\alpha_2 l}) \right]$$

with no approximations concerning the layer. Equation (B-20) can be separated into three terms. The term $\epsilon_2 e^{-\alpha_2 l}$ represents that part of the microwave flux from the subsurface which penetrates the boundary and then is attenuated by the layer. The term $(1 - e^{-\alpha_2 l})$ arises because of the flux originating in the layer that is attenuated in the layer itself before reaching the surface. The factor ϵ_1 , of course, is the usual emissivity factor because of the discontinuity between the surface and free space.

The average microwave temperature and the average surface temperature are equal when ϵ_1 and ϵ_2 are unity, so that all microwave flux originating in the subsurface and the layer emerges from the lunar surface. This result should not be surprising. In fact, since the microwave temperature is an "average" temperature and the surface temperature is an actual temperature, they are two different quantities which need not be numerically equal, but may be by coincidence, in special cases.

If one chooses reasonable values for the surface reflectivities and speculates some-what on a value for α , ℓ the factor Δ could reasonably range from 15% to 25%.

Two other facts should be pointed out. First, Equation (B-18) shows how the higher harmonics originate primarily in the layer. Secondly, it can be seen from Equation (B-19) that the phase angle, ℓ_n , arising from integrating through the subsurface does not have the limiting value of $\pi/4$ as in the homogeneous model, but reaches a maximum value and then decreases to zero as δ_{n2} is increased without limit.

SECTION B - PART I

A TWO-LAYER MODEL OF THE LUNAR SURFACE

REFERENCES

Jaeger, J. G., 1953, Aust. J. Phys., 6, 10.

-----, 1959, Nature, 183, 1316.

Jaeger, J. G., and Harper, A. F. A., 1950, Nature, 166, 1026.

Krotikov, V. D., and Troitskii, V. S., 1964, Soviet Physics Uspekki, 6, .

Levin, B. Yu., 1964, Soviet Astronomy, 7, 818.

Piddington, J. H., and Minnet, H. C., 1949, Aust. J. Sci. Res., A2, 63.

Salomovich, A. E., 1962, Soviet Astronomy, 6, 55.

Troitskii, V. S., 1962, Soviet Astronomy, 6, 51.

-----, 1965, Soviet Astronomy, 8, 576.

N66-28658

SECTION C

OBSERVATIONS OF VENUS NEAR THE 1962 INFERIOR CONJUNCTION

Published in Astrophysical Journal, Vol. 139,
No. 1, January 1, 1964, under the title,
"Preliminary Results from Measurements of
8.6 MM Radiation from Venus," by J. Copeland
and W. Tyler.

LIST OF FIGURES

SECTION C

		<u>Page No.</u>
Figure 1	Typical drift curves of Venus made on November 28, 1962, showing the 5°K calibrating signals. The drift rate is sidereal and the time constant is 1.5 seconds.	4
Figure 2	The brightness temperature of Venus as a function of the fraction of the planetary disk eliminated by the sun. The straight line is a least-squares best fit to the daily data points each weighted by the signal-to-noise ratio on that day. The error flags show the rms fluctuations converted to equivalent uncertainty in brightness temperature.	6

LIST OF TABLES

		<u>Page No.</u>
TABLE 1	SUMMARY OF 8-MM VENUS DATA	4

N66 28658

SECTION C

OBSERVATIONS OF VENUS NEAR THE 1962 INFERIOR CONJUNCTION

Radio observations of the planet Venus in the millimeter wavelength region have produced apparently conflicting results. Kuzmin and Salomonovich (1963) report that the brightness temperature of the planet at 8-mm wavelength depends strongly on the optical phase with a temperature minimum $374^{\circ} + 75^{\circ}\text{K}$ occurring just before inferior conjunction. Essentially the same results were given by Kislyakov, Kuzmin, and Salomonovich (1962) at a wavelength of 4 mm. On the other hand, Gibson (1963) reports a brightness temperature of 410°K at 8.6-mm wavelength with probable errors of $+ 30^{\circ}$ and -20°K . Although the change in phase angle during the observational period was limited, Gibson concludes that an appreciable variation of brightness temperature with phase is unlikely. Grant, Corbett, and Gibson (1963) have observed Venus at 4.3-mm wavelength. Their result is 350°K for the brightness temperature with probable errors of $+ 50^{\circ}$ and -30°K , and no indication of dependence on optical phase.

In addition to the observations described here, other measurements at millimeter wavelengths performed near the time of the 1962 inferior conjunction were those of Lynn (1962) at 8.5-mm and Welch (1962) at 8.35-mm. Lynn reports a brightness temperature of 380°K , with probable errors of $+ 70^{\circ}$ and -50°K , as an average over 4-day period, 1 month after conjunction. Welch gives 394°K , with a probable error of $+ 70^{\circ}\text{K}$, as an average brightness temperature over a 3-week period centered about 3 weeks before conjunction.

Kuzmin and Salomonovich (1962) and Lynn (1962) were able to obtain recognizable drift scans of Venus at 8.5 mm from one passage of the planet through the antenna beam. Other observers working at the same wavelength were forced to average individual daily scans in order to obtain measureable antenna temperatures. The purpose of this communication is to report additional 8.5 mm measurements in which the signal-to-noise ratio was sufficiently large that the averaging of individual scans was not necessary.

The observations reported here were made at 8.6 mm wavelength with a 28-foot, radome-inclosed, equatorially mounted paraboloid, following the inferior conjunction of 1962. The radiometer was a Dicke-type superheterodyne which switched between two antenna feed horns, one on boresight, and the other positioned so as to provide a beam displaced approximately one degree from the primary beam. The output fluctuations were about 1°K rms for a 1-second time constant. Calibration was provided by means of a $10,000^{\circ}\text{K}$ standard noise tube, the signal from which was reduced to 5°K by means of a directional coupler and an attenuator.

Antenna pattern measurements were performed about 3 weeks before conjunction by observing a known source (a power-monitored klystron and a standard gain horn) located 8 miles from the antenna. The receiver was a wide-band crystal-video system, temperature calibrated by means of a standard noise tube. The antenna exhibited a half-power beam-width of 4.1 minutes of arc in declination and 4.3 minutes of arc in right ascension.

Calculation of the absolute antenna gain required knowledge of the noise bandwidth of the receiver. Accurate measurements of the receiver bandwidth were complicated by its extreme broadness and the presence of several narrow "slots" in the passband. Preliminary laboratory tests indicate that the bandwidth of the receiver used for the antenna tests is larger than 20 per cent of the center frequency. The upper limit for the bandwidth can be established from the frequency range of the dominant waveguide mode which is about 40 per cent of the center frequency. It is believed that the most probable value of the bandwidth is somewhat less than 30 per cent of the center frequency.

The bandwidth which was chosen for actual calculation was 29 per cent, which led to a combined antenna efficiency-random loss combination at 31 per cent. A sample of the random material was measured for loss at 8.6 mm by independent observers, who reported a value of $2.3 \text{ db} \pm 0.1 \text{ db}$. When this factor is removed, the antenna efficiency that results is about 53 per cent, which is compatible with the results of previous antenna surface measurements.

The planet Venus was first detected on November 7, 1962. At the time of observation, Venus was nearly on the horizon and covered by clouds from an approaching rainstorm; the signal-to-noise ratio was therefore poor and no quantitative data was taken.

After 4 days of inclement weather, during which time tests and adjustments were made to optimize equipment performance, the observing program was begun on November 12, 1962. At this time, the planet was located radiometrically and, while tracking at sidereal rate, the antenna was carefully refocused for infinity by means of a remotely controlled, motor-driven feed support.

For a period of 4 weeks following conjunction observational data over a total of 7 days were accumulated. In the interest of minimizing indeterminate measurement uncertainties, observations were restricted to days while were clear and, in particular, when the radome material was dry. Furthermore, each daily observational period was near meridional crossing, when the planet's elevation angle was maximum, in order to further reduce atmospheric attenuation effects.

The daily experimental procedure was as follows:

1. The planet was located radiometrically.
2. While tracking in right ascension, the antenna was moved slowly in hour angle and declination so as to center the planet in the antenna beam.
3. The antenna beam was then positioned west of Venus. The subsequent motion of the planet through the beam provided the usual drift scan. Beginning on November 29, 1962, a small scan rate in hour angle was introduced in order to increase the time of passage through the beam. This permitted the use of a larger time constant to improve the signal-to-noise ratio.

4. After the planet had moved completely through the beam, the noise tube was energized, thereby providing a calibrating signal after each drift scan. One exception to this procedure was during the first day of observation when the radiometer was calibrated periodically with a 150°K calibrating signal, with the appropriate change in sensitivity afterwards. During the data reduction, it was determined that the radiometer sensitivity had been changing in an unknown manner between the times of calibration; therefore, the first day's data was omitted from the data reduction procedure.
5. The antenna beam was repositioned when the declination of Venus changed by one-half beamwidth as indicated by the ephemerides. When it was discovered during the data reduction that such a pointing correction resulted in an increase in antenna temperature, the immediately preceding drift scan was rejected as being low because of declination pointing error.

A sample of the drift scans made on November 28th, is shown in Figure 1. The November 28th scans were chosen for illustration because they were made near the middle of the observational program and are, therefore, more representative of average drift scans than those made nearer conjunction when the signal-to-noise ratio was larger.

The last observational attempt, on December 18, 1962, was unsuccessful. Simple linear extrapolation verifies that the antenna temperature on that date should have been only about twice the rms fluctuations and, therefore, difficult to distinguish from noise.

The observational period included phase angles from 174° on November 12th to 130° on December 9th. This corresponds to the fraction, k , of the planetary disk illuminated by the sun from 0.003 to 0.172, respectively. During this time the antenna temperature decreased from about 7°K to about 3.5°K .

The antenna temperatures were corrected for atmospheric attenuation by using a value of 0.2 db for zenith attenuation, with the usual correction for the zenith angle of observation.

The antenna temperatures were converted to brightness temperatures in the usual manner, with the angular size of the planet taken as that of the optical disk as tabulated in the ephemerides. The mean brightness temperatures obtained for each day of observation are tabulated in Table 1.

In order to investigate the phase dependence of brightness temperature, a straight line best fit to the daily brightness temperatures as a function of k was calculated. Each daily data point was weighted according to the signal-to-noise ratio on that day.

The result was:

$$T_n = 353 + 53 k. \quad (C-1)$$

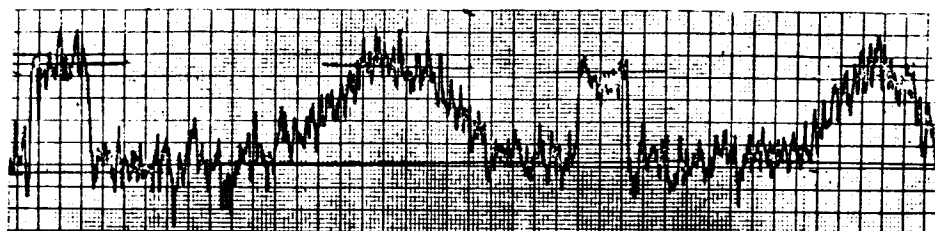


Figure 1 - Typical drift curves of Venus made on November 28, 1962, showing the 5°K calibrating signals. The drift rate is sidereal and the time constant is 1.5 seconds.

TABLE 1
SUMMARY OF 8-MM VENUS DATA

Date	No. of Drift Curves	Mean Antenna Temperature ($^{\circ}\text{K}$)	Mean Brightness Temperature ($^{\circ}\text{K}$)	k
November 12	15	6.75	383	0.003
November 14	9	6.22	355	.004
November 16	9	5.83	346	.006
November 27	4	5.26	357	.066
November 28	7	5.02	352	.072
November 29	3	5.14	376	.082
December 9	3	3.59	349	0.172

Equation (C-1) is plotted as the solid line in Figure 2, where the bars on the data points show the rms noise fluctuations in terms of equivalent uncertainty in brightness temperature. The dashed line is that of Kuzmin and Salomonovich.

Because of the possible large systematic error introduced by the uncertainty in antenna efficiency, the authors prefer not to discuss critically the validity of the absolute values of the temperatures quoted until more definitive antenna measurements can be performed.

The standard deviations that resulted from the least squares analysis were 10°K for the intercept and 120°K for the slope. The standard deviation of the points from the line is 13°K . The relative values of the temperatures are more reliable, therefore, and some conclusions concerning the change of brightness temperature with phase can be made. In particular, the standard deviation in slope of 120°K indicates that a slope larger than 360°K in the data reported here is most unlikely.

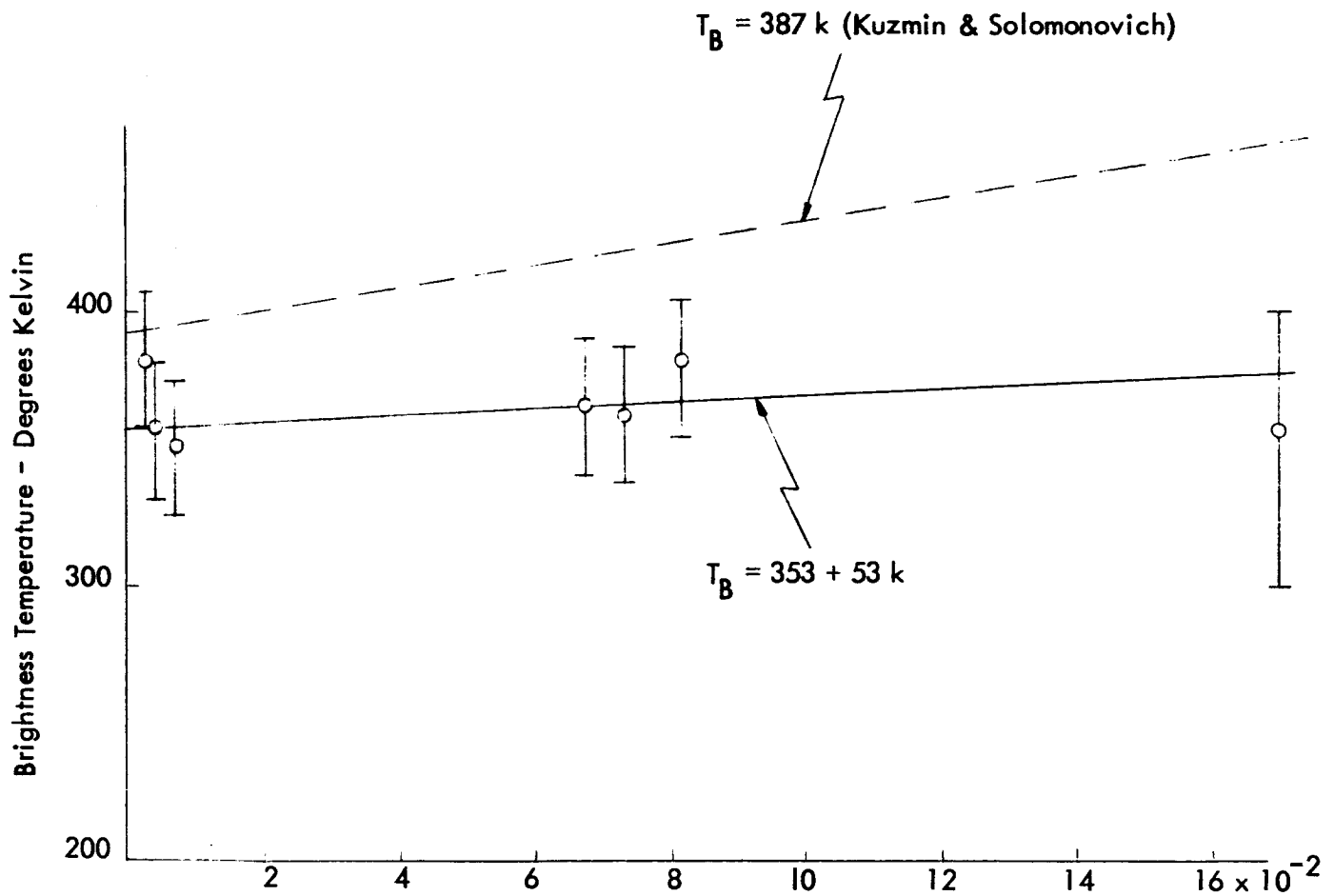


Figure 2 - The brightness temperature of Venus as a function of the fraction of the planetary disk illuminated by the sun. The straight line is a least-squares best fit to the daily data points each weighted by the signal-to-noise ratio on that day. The error flags show the rms fluctuations converted to equivalent uncertainty in brightness temperature.

SECTION C - PART I

OBSERVATIONS OF VENUS NEAR THE 1962 INFERIOR CONJUNCTION

REFERENCES

Gibson, J.E., 1963, Ap. J., 137, 611.

Grant, C.R., Corbett, H.H., and Gibson, J.E., 1963, Ap. J., 137, 620.

Kislyakov, A.G., Kuzmin, A.D., and Salomonovich, A.E., 1962,
Astr. Zhur., 39, 410.

Kuzmin, A.D., and Salomonovich, A.E., 1962, Astr. Zhur., 39, 660.

Lynn, L.V., 1962, private communication.

Tolbert, C., 1962, private communication (radome material tests).

Welch, J., 1962, private communication.

N66 28659

SECTION D

OBSERVATIONS OF VENUS NEAR THE 1964 INFERIOR CONJUNCTION

LIST OF FIGURES

SECTION D

		<u>Page No.</u>
Figure D-1	A typical drift scan (right) with a nominal 5°K calibrate signal (left).	2
Figure D-2	Antenna temperatures, corrected for atmospheric attenuation, as a function of date. The error bars show the rms deviations from each daily mean.	6
Figure D-3	Computed brightness temperatures (top) and 10.7 cm solar flux (bottom) as a function of date. The error bars show the rms deviation from each daily mean.	7

LIST OF TABLES

TABLE D-1	SUMMARY DATA	Page No.
		5

SECTION D

OBSERVATIONS OF VENUS AT 8.6 MILLIMETERS WAVELENGTH NEAR INFERIOR CONJUNCTION

This section of the report gives the results of radio observations of the planet Venus at 8.6 millimeters wavelength near the inferior conjunction of 1964. The original objective was to determine the average disk brightness temperature at this wavelength as a function of planetary phase angle. However, the reduced data contain anomalous variations which are larger than would be expected from phase alone so that a reliable measure of brightness temperature dependence on phase angle could not be made. Of more interest is the fact that the anomalous variations in brightness temperature appear to be correlated with solar activity.

The observations were performed with a 28-foot diameter, radome enclosed and equatorially mounted, antenna which exhibits half-power beamwidths of 4 minutes of arc in declination and 5 1/2 minutes of arc right ascension.

The radiometer is a conventional Dicke-type with switching between two antenna beams, one offset from boresight by approximately one degree to the east. The radiometer fluctuations with a one second time constant are about 4°K peak-to-peak.

All observations were made near meridional crossing on reasonably clear days when the radome was dry. Each day the planet was first located radiometrically and the antenna was positioned in declination for maximum signal. While tracking in hour angle at sidereal rate, the antenna was scanned alternately east and west at approximately one-sixth sidereal rate. A nominal 5°K calibrate signal was turned on after each scan. The radiometer time constant was 18 seconds. A typical drift scan and calibrate signal is shown in Figure D-1.

Outside temperature and relative humidity were recorded at the time of observation in order that the surface water vapor density could be calculated.

The atmospheric attenuation of 8.6 mm is caused primarily by the presence of oxygen and water vapor. If one assumes a homogeneous, plane parallel atmosphere, the effect of atmospheric attenuation can be removed by multiplying by the factor $\exp(\tau_{H_2O} + \tau_{O_2}) \sec \nu$, where τ_{O_2} and τ_{H_2O} are the zenith optical depths due to oxygen and water vapor respectively, and ν is the zenith angle at the time of observation.

The optical depth, τ_{O_2} , was taken to be constant and equal to 0.0276 (Meeks and Lilley 1963). The value for τ_{H_2O} depends on the water vapor content. A model due to Barrett and Chung, 1962, gives 0.006 per cubic meter of surface water vapor density. The daily values of $\exp(\tau_{H_2O} + \tau_{O_2}) \sec \nu$, so calculated ranged from 1.05 to about 1.20, with a typical value of about 1.12.

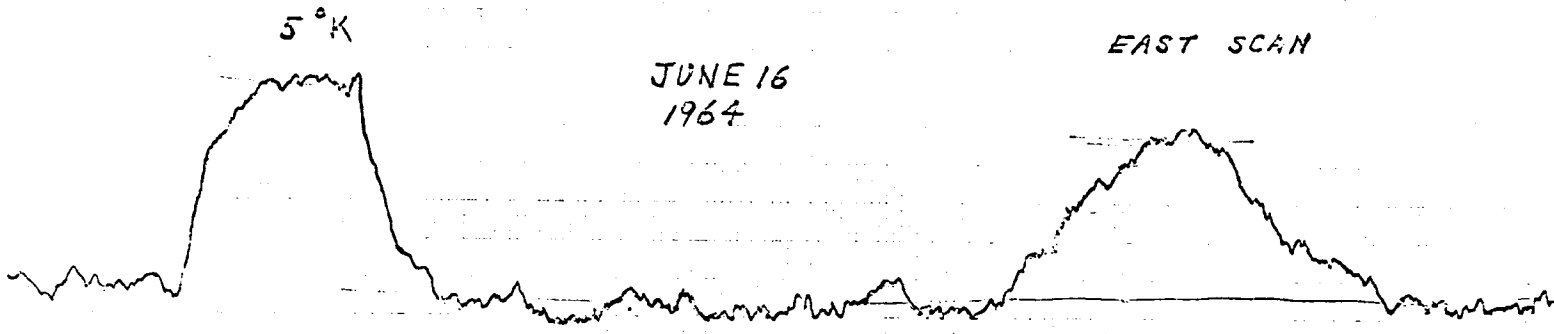


Fig.D-1 A typical drift scan (right) with a nominal 5°K calibrate signal (left).

1

2

The nominal 5°K noise tube calibrate signal was compared with thermal loads at 20°C and -7°C and found to be $4.75^{\circ}\text{K} \pm 0.12^{\circ}\text{K}$ (12 measurements).

Antenna pattern measurements were performed two months after the observational program. A power monitored klystron with a 2-foot diameter paraboloid was located at a site which was $8\frac{1}{2}$ miles from the antenna, and elevated approximately 500 feet. Although the far field requirements are not quite met, and the elevation angle was nearly zero, the transmitting site was the most remote available location.

The declination pattern is quite satisfactory; however, the hour angle pattern is somewhat deteriorated. The asymmetry in the pattern is believed to be caused by the method of fabrication and assembly that was used. The reflector was machined in two halves which were subsequently mated and attached to the supporting structure at the observation site. The demarcation line between the two halves is north-south, which indicated that the deteriorated hour angle pattern is probably the result of unsatisfactory mating of the two halves.

The antenna gain was also measured by comparison with a standard gain (20 db) horn and found to be $64.8\text{ db} \pm 1.21\text{ db s.d.}$ (6 observations). The signal-to-noise ratio when the standard gain horn was used, however, was so low that the calculated value of the standard deviation from the mean of 64.8 db is uncertain, particularly since only 6 measurements were made. A more reasonable value for the uncertainty in the measured gain is probably closer to 2.0 db.

The radome loss was measured directly by the following procedure. The radiometer was removed from the feed ring of the antenna and mounted, with a 2-foot diameter antenna on an equatorial tripod-supported telescope mount. Solar antenna temperatures measured from inside and outside of the radome were compared. The ratio of solar antenna temperature to the calibrate signal was found to be 7.40 ± 0.14 (6 measurements) outside the radome and 4.75 ± 0.12 (12 measurements) inside the radome. The radome loss is, therefore, 1.93 db ($+0.33\text{ db}$, -0.44 db).

The antenna temperature were corrected for atmospheric and radome loss, and converted to average disk brightness temperatures in the usual manner, with the angular size of the planet taken as that of the optical disk as tabulated in the ephemerides.

The data is summarized in Table D-1. The antenna temperatures shown in Table D-1 have been corrected for atmospheric attenuation only; the brightness temperatures contain the radome loss correction.

The 4-day period just after conjunction was unsuitable for observations because of the proximity of the sun to the comparison beam.

The antenna temperature as a function of data are shown in Figure D-2. The deviations from a smooth curve about June 6th and again around July 1st and July 28th, are reflected in the computed brightness temperatures which are shown in Figure D-3, along with the 10.7 cm solar flux during the observational period.

As can be seen from Figure D-2, there appears to be some crude correlation between the brightness temperatures and the 10.7 cm solar flux; however, it should be recognized that such an effect could simply be due to incorrect atmospheric attenuation corrections because of daily variations from the assumed model. On the other hand, the effect of solar activity appears more pronounced further away from conjunction when a larger fraction of the planetary disk is illuminated, which lends some credence to the reality of the phenomenon.

As can be seen from Figure D-2, there appears to be some crude correlation between the brightness temperatures and the 10.7 cm solar flux; however, it should be recognized that such an effect could simply be due to incorrect atmospheric attenuation corrections because of daily variations from the assumed model. On the other hand, the effect of solar activity appears more pronounced further away from conjunction when a larger fraction of the planetary disk is illuminated, which lends some credence to the reality of the phenomenon.

TABLE D-1- SUMMARY OF DATA

Date	Antenna Temperature, T_A , Degrees Kelvin	$(\Delta T_A)_{rms}$ $^{\circ}K$	Brightness Temperature, T_B , Degrees Kelvin	$(\Delta T_B)_{rms}$ $^{\circ}K$	Phase Angle Degrees	e sec τ	Number of Measurements
May							
28	3.3	0.64	459	89	135	1.07	7
29	3.0	0.51	401	69	136	1.08	7
30	3.4	0.52	447	68	137	1.10	7
31	2.8	0.31	354	40	138	1.11	7
June							
1	3.1	0.40	385	50	139	1.09	7
2	3.4	0.51	407	61	141	1.11	9
3	2.5	0.53	292	62	143	1.11	7
4	2.9	0.68	295	70	145	1.08	7
5	3.3	0.33	330	33	146	1.07	6
6	3.5	0.39	347	38	148	1.09	7
10	3.6	0.72	355	71	156	1.15	8
11	4.1	0.33	397	32	158	1.09	5
12	3.9	0.48	374	46	160	1.09	9
15	4.1	0.84	371	77	166	1.12	7
16	4.2	0.62	379	56	168	1.08	8
17	4.1	0.52	369	47	170	1.09	8
18	4.2	0.54	373	48	174	1.10	4
19	4.1	0.69	363	61	175	1.14	6
28	3.9	0.62	374	60	163	1.09	7
29	4.1	0.35	403	34	162	1.10	6
30	3.9	0.51	386	50	160	1.15	6
July							
1	3.7	0.56	379	57	157	1.15	8
2	3.7	0.60	381	61	155	1.16	8
5	3.6	0.52	406	58	150	1.14	8
6	3.5	0.44	397	50	147	1.12	7
7	3.3	0.50	386	59	146	1.13	9
8	3.1	0.47	366	55	144	1.12	8
12	2.8	0.47	378	64	137	1.16	5
15	2.3	0.43	349	64	136	1.15	6
17	2.2	0.37	347	59	130	1.14	9
18	2.4	0.47	403	77	129	1.17	8
20	2.6	0.60	459	103	126	1.11	6
22	2.0	0.19	377	36	124	1.19	4
23	2.2	0.20	423	38	123	1.18	7
29	1.3	0.43	300	101	117	1.19	4
30	1.9	0.73	458	177	115	1.11	4
31	2.0	0.36	493	89	114	1.08	5

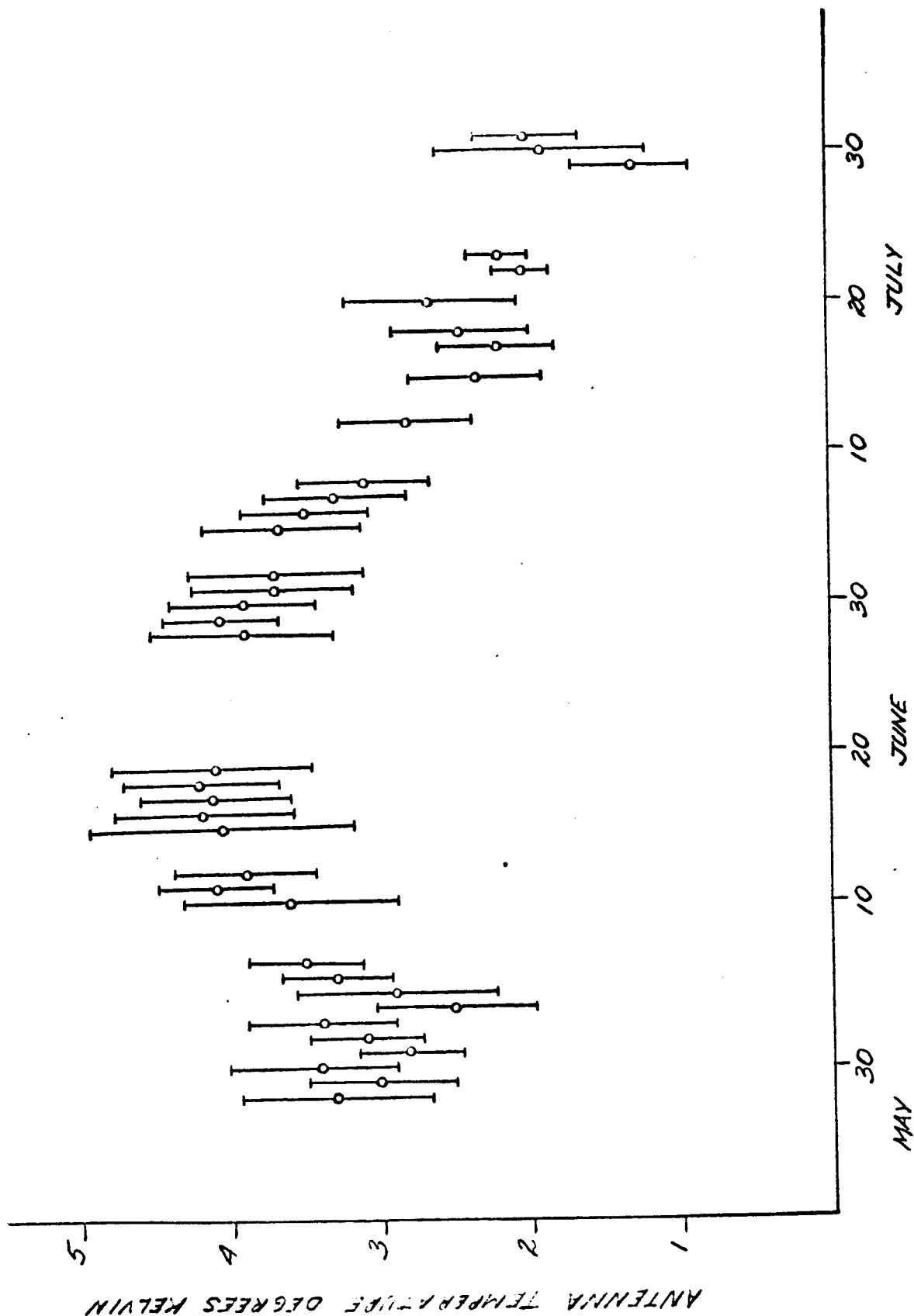


Fig. D-2 Antenna temperatures, corrected for atmospheric attenuation, as a function of date. The error bars show the rms deviations from each daily mean.

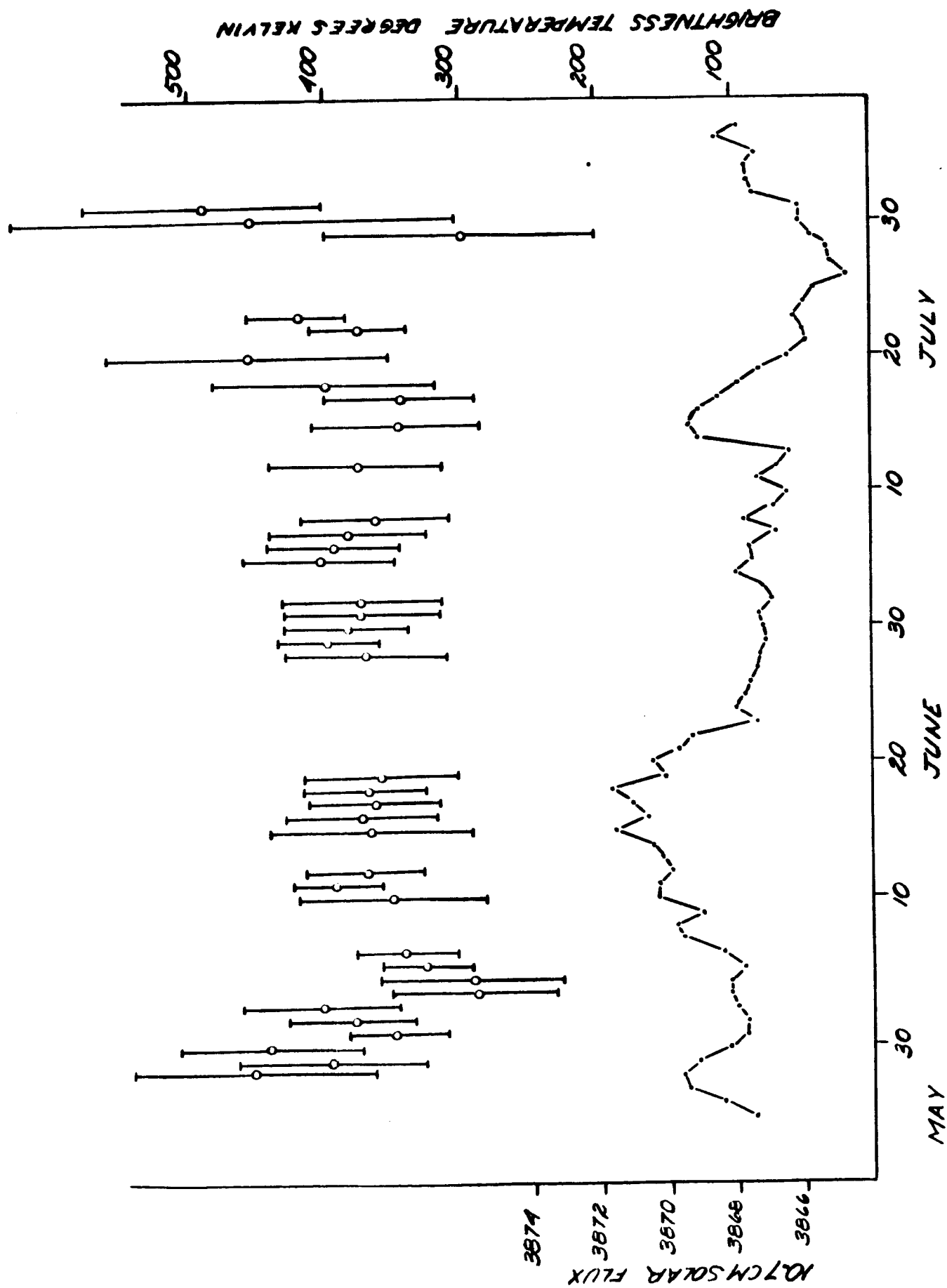


Fig.D-3 Computed brightness temperatures (top) and 10.7 cm solar flux (bottom) as a function of date. The error bars show the rms deviation from each daily mean.

SECTION D - PART I

OBSERVATIONS OF VENUS NEAR THE 1964 INFERIOR CONJUNCTION

REFERENCES

Barrett, A. H., and Chung, V.K., 1962, J. Geophys. Res., 67, 11.

Meeks, M.L., and Lilley, A.E., 1963, J. Geophys. Res., 68, 6.

N66 28660

PART II

ATMOSPHERIC EFFECTS ON
CELESTIAL RADIO MEASUREMENTS
AT 8.6 MILLIMETERS

BY

PAUL M. KALAGHAN

PART II

TABLE OF CONTENTS

	<u>PAGE NO.</u>
1.0 INTRODUCTION	1
2.0 THEORETICAL CONSIDERATIONS	3
2.1 General Form of Atmospheric Attenuation and Reradiation	
2.2 Comparison of Atmospheric Effects on Solar, Lunar and Planetary Observations	
3.0 REVIEW OF OBSERVATIONAL METHODS AND DATA	10
3.1 Stanford University (Lee and Waterman, 1964)	
3.2 Naval Research Laboratory (Coates, 1958)	
3.3 Aerospace Corporation (Shimabukuro, 1965)	
4.0 MEASUREMENT PROGRAM	14
4.1 Method of Observation	
4.2 Observational Data	
4.3 Data Reduction	
4.4 Conclusions	
5.0 RADOME CONSIDERATIONS	18
<u>ADDENDUM</u> - ATMOSPHERIC CHARACTERISTICS	30

LIST OF FIGURES

<u>Figure No.</u>	<u>Title</u>	<u>Page No.</u>
1	Histogram of Measured Daily Medians of Vertical Through the Atmosphere Attenuation at 8.6 MM During Period December 1962 Through April 1963.	22
2	Summary of Zenith Attenuation at 3.2 MM and Precipitable Water Vapor for the Year 1964.	22
3	Effect of Thick Clouds on Attenuation	23
4	Secant of Zenith Angle Versus Hour Angle and Declination, δ	24
5	Typical Solar Recordings	25
6	Photodetector Weather Groupings	26
7	Uncorrected Data Distribution	27
8	Secant Corrected Distribution	27
9	Modified Secant Corrected Distribution	29

ADDENDUM

1	Attenuation of Radio Waves in Oxygen and Water Vapor	31
2	Atmospheric Attenuation Versus Wavelength	37
3	Per cent of Total Measured Precipitation of Raindrops as a Function of Drop Diameter for Various Precipitation Rates	41
4	Transmission Loss Due to R in Fall	42

LIST OF TABLES

<u>TABLE NO.</u>	<u>TITLE</u>	<u>PAGE NO.</u>
1	Measured Atmospheric Attenuations and Antenna Temperatures (Coates, 1958)	21

ADDENDUM

1	Linewidth Factors Used to Determine Atmospheric Absorption	33
2	Values Used in the Calculation of Atmospheric Absorption	34
3	Water Vapor Attenuation (One way) in db/km After Gunn-East	35
4	Pressure and Temperature Correction for Oxygen Attenuation for Wavelengths between 0.7 and 10 cm After Gunn-East	35
5	Expected Absorption Coefficients of Trace Atmospheric Constituents at 300°K (Westwater et al, 1964)	38
6	One-way Attenuation Coefficient, K_1 , In Clouds in db/km/gm/m ³ (Westwater et al, 1964)	39
7	Percentage of Total Volume of Rainfall Occupied by Raindrops of Different Diameters D (cm) and Varying Rainfall Rates p (mm/hr).	44
8	Attenuation in Decibels per Kilometer for Different Rates of Precipitation of Rain.	44
9	Attenuation in Rains of Known Drop Size Distribution and Rate of Fall	45
10	Correction Factor for Rain Attenuation	45

1.0 INTRODUCTION

The development and operation of a 28-foot diameter millimeter radio telescope represents several advanced engineering challenges each associated with the fact that the antenna aperture is $28 \times 12 \times 25.4/8.6$ wavelengths in diameter when operating at a wavelength of 8.6 millimeters. This situation introduces the need for new techniques for the evaluation of instrument performance. There is a paucity of data available concerning applicable measurement techniques and anticipated performance. Only three telescopes of this size are currently in operation at millimeter wavelengths in the United States. The investigation of instrument performance in any one of several areas could very easily have accommodated the entire scope and time period of the effort. Our prime objective, however, was the accumulation and reduction of scientific data which necessitated that the degree of penetration into engineering detail be limited to a level considered sufficient to achieve the data accumulation objective. The various engineering problems and degree of investigation of each have been discussed in detail in the various monthly and quarterly reports. The scientific objective of the investigation suggested that a minimum of detailed engineering information be presented in this Final Report.

Methods of observation and related instrument limitations occupied a considerable portion of the engineering support effort. Areas of consideration included:

- a. Methods for establishing the focal plane of the secondary reflector.
- b. Techniques for the cancellation of the atmospheric reradiation component.
- c. The effect of the atmosphere in the near field of the antenna aperture (far field approximately 12 miles).
- d. Determination of the antenna beam position.
- e. Calibration of indicated versus actual radio beam position.
- f. Attenuation and reradiation attributable to atmospheric gases and associated condensation and precipitation products.
- g. Measurement errors introduced by the radome under various observational conditions.

The latter two areas of consideration were considered of increasing significance as the program progressed. During the latter phase of the program a series of measurements were undertaken to determine the probable magnitude of the error introduced as a consequence of atmospheric attenuation. It was concluded as a result of these measurements that the methods of observation and data reduction used in the lunar measurements reduced the effect of atmospheric errors to a negligible degree. This conclusion is based on the large number of observations made (in excess of 4,000) which allowed for selection of near ideal observing conditions as well as data selection on the reasonable assumption that the lunation curve for a selected area of the moon would be invariant from one lunation period to any other. This condition, of course,

does not hold for observations of solar radiation which are nonperiodic or for observations of the planet Venus which are confined to a relatively short time period of observation negating the opportunity for repetitive measurement on a convenient time scale, i.e., only two conjunctions of the planet Venus were observed during the program period while more than thirty lunations of the moon were observed. The selection criteria for observation and data reduction of lunar data were as follows:

1. All observations were made within ± 1 hour of meridian crossing to minimize the effect of variation in the secant correction.
2. All observations were made under "clear weather" conditions defined as less than 1/10 cloud cover and an apparent blue rather than hazy sky.
3. All observations made after periods of precipitation were preceded by a regularly programmed scan of the antenna beam in both hour angle and declination from horizon to horizon covering that portion of the radome "illuminated" by the antenna aperture during the time of lunar observations. For these tests the radiometer was operated in its most sensitive mode to detect any inhomogeneities or departures from a uniform reradiation temperature distribution. Nonuniform reradiation is typical of a wet radome condition.

A more detailed discussion of radome characteristics and methods of observation pertaining to the radome are presented in Section 5.0.

That portion of the measurement program directed to the determination of atmospheric effects concentrated prime attention on determining the efficacy of the selected criteria for observations and data reduction used in the lunar program as described above. The measurements were extended to include observational conditions considered more adverse than allowed by the selection criteria in the hope that a selection criteria for future measurements could be extended to include a greater number of useful days of observation. Observational conditions which would otherwise meet the selection criteria with the exception of a high degree of scattered cloud cover (0.1 to 0.8) were given particular attention. As a result of this portion of the measurement effort, it was established that a simultaneous record of solar intensity obtained from an optical monitor was of considerable aid in identifying those portions of the radio record during which the sun was momentarily obscured by clouds. Deleting these portions of the record and reducing only that data obtained when the sun is unobscured adds to the number of observational days by the simple expedient of this additional selection criteria.

2.0 THEORETICAL CONSIDERATIONS

2.1 General Form of Atmospheric Attenuation and Reradiation

The amount of radiation flowing in any radiation field is conventionally described by the amount of radiant energy, DE , in a specified frequency interval $(\nu, \nu + d\nu)$ which is transported across an element of area $d\sigma$ and in directions confined to an element of solid angle $d\omega$ during a time dt . The solid angle is centered around the polar angles (Θ, Φ) , measured with respect to the normal to the surface. This energy is expressed in terms of the intensity, I_ν , by (Chandrasekhar, 1960):

$$dE = I_\nu \cos\Theta d\sigma d\omega d\nu dt \quad (1)$$

The variation of the intensity through a medium is related to the absorptive and emissive properties of the medium. The absorptive characteristics may be expressed through an absorption coefficient, α_ν , which is the absorption per unit path length, occurring at frequency ν .

The emissive characteristics are expressed by an emission coefficient, j_ν , which is defined as the amount of radiated energy per unit time, per unit frequency interval, per unit solid angle by an emitter of mass dm . During conditions of local thermodynamic equilibrium, the emission coefficient is related to the Planck function, $B_\nu(T)$, by Kirchoff's Law (Goody, 1964).

$$j_\nu = \frac{\alpha_\nu}{\rho} B_\nu(T) \quad (2)$$

where:

$$B_\nu(T) = \frac{2h\nu^3}{c^2} \frac{1}{e^{h\nu/kT} - 1} \quad (3)$$

ρ = the mass density of the material

In (3), h is Planck's constant, k is the Boltzmann constant, c is the velocity of light, and T is the absolute temperature.

Equation (3) for the emission function can be simplified for microwave frequencies by using the Rayleigh-Jeans approximation:

$$B_\nu(T) = 2KT \frac{\nu^2}{c^2} \quad (4)$$

The amount of radiation emitted by the atmosphere and received by a radiometer can be determined by integrating the radiation transfer equation along a ray path. This equation is (Meeks and Lilley, 1963):

$$\frac{dI_\nu}{ds} = -\alpha_\nu [I_\nu - B_\nu(T)] \quad (5)$$

Here ds is an increment of path length. The solution of (5) evaluated at the ground is:

$$I_{\nu} = I_{\nu,0} e^{-\int_0^{\infty} \alpha_{\nu}(s') ds'} + \int_0^{\infty} B_{\nu}(s) \alpha_{\nu}(s) e^{-\int_0^s \alpha_{\nu}(s') ds'} ds \quad (6)$$

where $I_{\nu,0}$ is the unattenuated intensity of discrete sources lying outside the earth's atmosphere. The first term represents contributions to the received energy from external noise sources attenuated by the intervening medium. The second term may be understood physically as follows: An element along the path emits energy toward earth at a rate equal to $B_{\nu} \alpha_{\nu} ds$; this emitted energy is in turn attenuated by the intervening medium by an amount:

$$e^{-\int_0^s \alpha_{\nu}(s') ds'}$$

The total contribution is then obtained by integrating all contributions along the ray path.

It is now necessary to consider the functional dependencies of the variables α_{ν} and B_{ν} . The absorption coefficient, α_{ν} , is an explicit function (see Addendum, Table 2) of meteorological parameters such as temperature, pressure and water vapor density. These parameters are, in turn, functions of position along the ray path, thus making the absorption an implicit function of position, it is this dependence which has been indicated above. Similarly, the Planck function, which is an explicit function of temperature alone, can be written as a function of position. The intensity received at the ground, I_{ν} , thus depends on the meteorological profile at every point on the ray path. The intensity may be related to a quantity called the brightness temperature, $T(\nu)$:

$$I_{\nu} = 2K \frac{\nu^2}{c^2} T(\nu)$$

which compares the received emissions in a single direction to those of a black body at temperature $T(\nu)$.

Thus, introducing the concept of an apparent brightness temperature corresponding to each intensity function $I_{\nu,0}$ and $B_{\nu}(s)$, the result for intensity function I_{ν} given in (6) may be expressed:

$$T(\nu) = T_s(\nu) e^{-\int_0^{\infty} \alpha_{\nu}(s) ds} + \int_0^{\infty} T_M(\nu, s) \alpha_{\nu}(s) e^{-\int_0^s \alpha_{\nu}(s') ds'} ds \quad (7)$$

As with the interpretation given to (6), the first term corresponds to the apparent temperature received from a source beyond the atmosphere while the second term represents the temperature contribution reradiated by the medium between the cosmic sources and the observer.

In order to collect this radiation, an antenna must be placed in the medium. However, a real antenna will receive radiation from all directions for any particular antenna orientation, whereas the brightness temperature as defined above refers to the contributions from only a single direction. The effective brightness temperature, $T_A(\nu, \Theta', \Phi')$, measured by an antenna pointing in the direction (Θ', Φ') may be expressed as (Pawsey and Bracewell, 1955):

$$T_A(\nu, \Theta', \Phi') = \frac{1}{4\pi} \int_{\text{ALL SPACE}} G(\Theta', \Phi' | \Theta, \Phi) T(\nu, \Theta, \Phi) d\Omega \quad (8)$$

where $G(\Theta', \Phi' | \Theta, \Phi)$ is the directional gain function in the direction (Θ, Φ) with respect to the antenna axis; $T(\nu, \Theta, \Phi)$ is the brightness temperature in this direction, and the integration extends over all solid angles, $d\Omega$. For passive probing purposes, a highly directional antenna with low side lobes is necessary so that the measured effective noise temperature closely approximates the brightness temperature in the desired direction (Westwater, 1965).

Expanding (8) into the individual radiation terms, $T_A(\nu)$ becomes:

$$T_A(\nu) = \frac{1}{4\pi} \int G(\Theta', \Phi' | \Theta, \Phi) T_{\nu(s)} e^{-\int_0^s \alpha_{\nu}(s') ds'} d\Omega + \frac{1}{4\pi} \int G(\Theta', \Phi' | \Theta, \Phi) T_M(\nu, s, \Theta, \Phi) \alpha_{\nu}(s) e^{-\int_s^{\infty} \alpha_{\nu}(s') ds'} ds d\Omega \quad (9)$$

Note that the first integral is evaluated only over those directions containing an extra-terrestrial source since only in such directions is $T(\nu)$ nonzero. The form of the antenna receiving pattern represented by $G(\Theta', \Phi' | \Theta, \Phi)$ in the second term is of particular significance here. Since G is usually measured only in the far field of the aperture, the use of G in an integral such as contained in Equation (9) implies that the brightness distribution is also in the far field. If this is not the case, then the antenna pattern must be obtained over the region where the radiation is occurring. For example, with a 28-foot diameter antenna operating at 8.6 mm, the far field begins some nine (9) miles away. Thus, to perform sky temperature calculations from Equation (9), the near field antenna patterns as explicit function of distance must be employed in the integration implied.

Assuming a horizontally stratified atmosphere and neglecting the effects of refraction, the element of path length can be expressed in terms of the height, h , of the absorptive layer between height h and $+dh$ as follows:

$$ds = dh \sec \Theta$$

where Θ is the zenith angle of the ray under consideration. Introducing the opacity, τ_{ν} , defined as:

$$\tau_{\nu}(h) = \int_0^h \alpha_{\nu}(h') dh'$$

Equation (9) becomes:

$$T_A(\nu) = \frac{1}{4\pi} \int_{\text{COSMIC SOURCES}} e^{-\tau_\nu(\omega) \sec \Theta} T_{(\nu)_S}(\Theta, \phi) G(\Theta, \phi' | \Theta, \phi) d\Omega$$

$$+ \frac{1}{4\pi} \int \int_{\text{ALL SPACE}} e^{-\int_0^h \alpha_\nu(h') \sec \Theta dh'} T_M(\nu, h) \sec \Theta \alpha_\nu(h) G(\Theta, \phi' | \Theta, \phi) dh d\Omega$$
(10)

As a particular case of the previous expression, consider the situation where the Sun is the extraterrestrial source with solid angle Ω_0 and where the atmospheric temperature depends only on height, then:

$$T_A(\nu)_0 = \frac{1}{4\pi} T_{(\nu)_0} \int_{\Omega_0} e^{-\tau_\nu(\omega) \sec \Theta} G(\Theta, \phi' | \Theta, \phi) d\Omega$$

$$+ \frac{1}{4\pi} \int \left(\int_0^\infty e^{-\int_0^h \alpha_\nu(h') \sec \Theta dh'} T_M(\nu, h) \sec \Theta \alpha_\nu(h) dh \right) G(\Theta, \phi' | \Theta, \phi) d\Omega$$
(11)

or assuming the solar diameter is relatively small compared to the complement of the zenith angle, so that $\sec \Theta$ is constant over the extent of the solar disc:

$$T_A(\nu)_0 = T_{(\nu)_0} e^{-\tau_\nu(\omega) \sec \Theta_0} \frac{1}{4\pi} \int_{\Omega_0} G(\Theta, \phi' | \Theta, \phi) d\Omega$$

$$+ \frac{1}{4\pi} \int \left(\int_0^\infty e^{-\tau(h) \sec \Theta} T_M(\nu, \tau_\nu(h)) \sec \Theta d\tau \right) G(\Theta, \phi' | \Theta, \phi) d\Omega$$
(12)

The second term above can be calculated only with the aid of radiosonde temperature profiles along the ray path. This is usually not attempted and instead a mean profile is often employed together with ground values of temperature, pressure and humidity. If, however, mean atmospheric temperature \bar{T}_M is introduced, the integration in the second term can be easily performed so that:

$$\int_0^{\tau_\nu(\omega)} T \sec \Theta d\tau e^{-\tau_\nu \sec \Theta} = \bar{T}_M (1 - e^{-\tau_\nu(\omega) \sec \Theta})$$

Thus:

$$T_A(\nu)_0 = T_{(\nu)_0} e^{-\tau_\nu(\omega) \sec \Theta_0} \int_{\Omega_0} \frac{G d\Omega}{4\pi} + \bar{T}_M \left(1 - \int_{\text{ALL SPACE}} e^{-\tau_\nu(\omega) \sec \Theta} \frac{G d\Omega}{4\pi} \right)$$
(13)

For an antenna system whose main lobe is much less than the solar diameter in width,

$$T_A(\nu)_0 = \rho_0 T(\nu)_0 e^{-\tau_v(\infty) \sec \theta_0} + \bar{T}_m (1 - e^{-\tau_v \sec \theta_0}) \quad (14)$$

where ρ_0 is the efficiency of the antenna system when viewing a source of solid angle Ω_0 .

From this model situation it can be seen that the effects of the atmosphere are to reduce the temperature of the sources observed and to produce an additional temperature contribution which depends on the actual stratification of the atmosphere at the time of observation and the antenna beam pattern of the receiving system. (It should be noted that in spite of the simplicity of the assumptions involved in its derivation, Equation (14) is the basic relationship between antenna temperature $T_A(\nu)$ and the observed brightness distributions used throughout the vast majority of millimeter atmospheric research.)

2.2 Comparison of Atmospheric Effects on Solar, Lunar and Planetary Observations

In order to see the effects of the reradiated energy from the atmosphere on the antenna temperature, let us consider the three cases where (1) the sun is the celestial source being observed, (2) the moon is the source being observed and (3) a planet is being observed. Rewriting Equation (12) assuming a constant source temperature, source size smaller than the antenna beam and a mean atmospheric temperature \bar{T}_m , the following results:

$$T_A(\nu) = \rho(T(\nu)_s \left(\frac{\Omega_s}{\Omega_A} \right) e^{-\tau \sec \theta} + \bar{T}_m (1 - e^{-\tau \sec \theta})) = T_s e^{-\tau \sec \theta} + \bar{T}_m (1 - e^{-\tau \sec \theta}) \quad (15)$$

where:

$$\begin{aligned} T(\nu)_s &= \text{source temperature} \\ \bar{T}_m &= \text{mean atmospheric temperature} \\ T_s &= \rho T(\nu)_s (\Omega_s / \Omega_A) \\ \Omega_s &= \text{the solid angle subtended by the source} \\ \Omega_A &= \text{the solid angle subtended by the main lobe of the antenna pattern } (\Omega_A > \Omega_s) \end{aligned}$$

Considering now the second term in Equation (15) as the antenna temperature due only to the atmosphere, it is necessary to investigate its magnitude for various combinations of atmospheric temperatures and source temperatures. Noting first from the work of Wulfsburg (1964) that \bar{T}_m lies between 250°K and 300°K, the maximum effect will occur when \bar{T}_m is 300°K. If the sun is considered as the source under

observation, then for a receiving system with an antenna beamwidth smaller than the sun's diameter, T_s will be in the vicinity of 5000°K ; for a system with an antenna beamwidth twice as large as the sun's diameter, T_s will be approximately 1000°K ; and for a beamwidth four times greater than the sun's diameter, T_s will be approximately 250°K . Similarly, for the moon (diameter of 30 minutes of arc), T_s for a small antenna beam (i.e., less than 10 minutes of arc) will be about 110°K ; for an antenna beam twice the lunar diameter T_s will be approximately 30°K ; and for an antenna beamwidth four times the lunar diameter, T_s will be reduced to approximately 8°K . Finally, for a planet such as Venus, when subtending an angle of one minute, a four-minute of arc beam would yield a 10°K antenna temperature under optimum conditions.

From the range of T_s values given above, it is clear that the effect of the atmospheric term in (15) can vary considerably. For the case of antenna beamwidths of 4 minutes of arc, the ratio of source term to reradiation term becomes:

$$\begin{aligned}\text{Sun:} & \quad -.060 (1 - e^{+T \sec \Theta}) \\ \text{Moon:} & \quad -2.72 (1 - e^{+T \sec \Theta}) \\ \text{Venus:} & \quad -37.5 (1 - e^{+T \sec \Theta})\end{aligned}$$

Alternatively, for 1 degree (60 minutes of arc) antenna beamwidths these same ratios become:

$$\begin{aligned}\text{Sun:} & \quad -.300 (1 - e^{+T \sec \Theta}) \\ \text{Moon:} & \quad -10.0 (1 - e^{+T \sec \Theta}) \\ \text{Venus:} & \quad -6000 (1 - e^{+T \sec \Theta})\end{aligned}$$

It is obvious from these figures that the atmospheric term is always of significance in lunar and planetary observations, while in solar work the atmospheric term may often be negligible when beamwidths smaller than the solar diameter are employed and the observations are confined to clear cold weather.

It should be noted that because of the preponderance of the atmospheric term in lunar and planetary observations, an observation scheme has been evolved wherein an additional signal derived from a second smaller antenna (looking parallel to the main antenna beam) is continuously subtracted from the main beam signal. The efficacy of this "exploded beam" technique comes from the fact that if the secondary antenna beam is made large, then it will sense only the contribution from the atmosphere. For a beamwidth of 10 degrees, for example, the signal from the moon in the exploded beam would amount to less than 0.3°K so that only a negligible portion of the lunar signal would be lost in the subtraction process. This technique loses its efficacy when the source is so bright that the required secondary beam becomes large and integrates the response over too vast a region of the sky, thereby decorrelating the subtracted atmospheric signal from the actual atmospheric contribution which is intended to be eliminated from the main beam signal. Thus, when an exploded beam is employed, Equation (15) reduces to the simple form:

$$T_A(\nu) = T_s e^{-\tau \sec \Theta} \quad (16)$$

An alternate approach to the cancellation of the atmospheric reradiation term is to measure the sky temperature in the region adjacent to the source and then manually subtract this contribution from the temperature produced when the source was in the beam. When this procedure is adopted, a system equation identical to Equation (16) also results.

Once the atmospheric reradiation term has been eliminated by some subtraction process and Equation (16) results, it is a simple matter to determine the net opacity. In particular, when natural logarithms are taken of both sides of Equation (16), it is apparent that the slope of the function $\ln(T_A(\nu)/T_s)$ when plotted against secant Θ is the actual opacity τ . Thus, the usual reduction procedure for observation is to plot the logarithm of the antenna temperature versus the secant of the zenith angle and determine the zenith opacity from the slope of the resulting curve.

3.0 REVIEW OF OBSERVATIONAL METHODS AND DATA

Experimental determinations of absorption through the entire atmosphere using radiometers to measure signals received either from thermal sources in the atmosphere or from extraterrestrial sources such as the sun, moon, etc., have been attempted over most of the electromagnetic spectrum. In the following sections typical measurement programs undertaken to date at Stanford University, the Naval Research Laboratory and Aerospace Corporation will be reviewed in regard to their basic observational data techniques and their method of data reduction.

3.1 Stanford University (Lee and Waterman, 1964)

35 Gc measurements of daily attenuation levels due to the atmosphere were made at Stanford Electronics Laboratories by Lee and Waterman. This effort consisted of a program of regular measurement of atmospheric absorption at a frequency of 35 Gc extending over a period of five months from December 1962 to April 1963. The measurements utilized the sun as a source of radiation which was received with a 5-foot paraboloidal reflector and Dicke-type radiometer.

The antenna consisted of a modified searchlight reflector, 60 inches in diameter, having a 0.4 degree beamwidth at 35 Gc and mounted equatorially. A waveguide feed was used, and an integrally mounted superheterodyne receiver with an intermediate frequency of 30 Mc and a bandwidth of 10 Mc. The receiver input was connected to a ferrite switch, which switches between the horn feeding the paraboloid and a temperature reference (a discharge tube in series with a precision attenuator) at a rate of 1000 cps. The detected output of the receiver was fed to a phase detector, along with the 1000 cps switching voltage, and then to a low-pass filter. The time constant of this filter was typically 1 second, and the instability of the output was a few degrees Kelvin.

The difference in effective temperature of the radiometer with the antenna pointed at the sun and at the adjacent sky was measured for solar elevation angles down to 5.75° (to avoid complications due to atmospheric refraction), and was plotted as a function of the cosecant of the solar elevation angle. When the atmosphere is horizontally stratified and unchanging, the logarithm of the apparent temperature of the sun will be a linear function of the cosecant of the solar altitude, with a slope equal to the attenuation vertically through the atmosphere. The data was graphically reduced according to this principle, and the maximum inaccuracy was found to be less than 0.01 db for a vertical attenuation of 0.30 db. On many days the attenuation varied considerably. Effective solar temperature appears to have been constant during the quarter within 2 or 3 per cent.

The median attenuation (of the daily medians) on "clear" days was 0.24 db, with a range of 0.19 to 0.35 db. The median attenuation on "cloudy" days was 0.34 db, with a range of 0.23 to 0.65 db. The median for all days was 0.27 db.

The difference between "clear" and "cloudy" medians, about 0.1 db, appears to be very typical of individual clouds, as indicated by the intervention of a cloud on "clear" days when it was possible to measure the attenuation increase due to the presence of the cloud.

Observations have been carried out during rain on several occasions. The resultant attenuations varied from normal to a peak value of 6.72 db during one heavy rainstorm. With the exception of this occasion, the peak attenuation during moderate rain did not exceed 1.60 db.

The correlation between ground level humidity and vertical attenuation on "clear" days was fairly good (perhaps good enough to be useful), but, of course, the ground level humidity is not a good measure of over-all atmospheric-water-vapor content. Figure 1 is a histogram of the measured daily medians. On two occasions measurements were as high as 0.65 and 0.90 db.

The measurements were intended to provide a quantitative example of the range and distribution of vertical through-the-atmosphere attenuation at 8.6 mm. In evaluating their applicability to other areas, it should be noted that they were made in a climate of medium humidity (the absolute humidity at ground level averaged $7 - 8 \text{ gm/m}^3$ during the measurement period).

3.2 Naval Research Laboratory (Coates, 1958)

In July 1956, a program of absolute measurements of solar radiation and atmospheric attenuation was initiated at a wavelength of 4.3 mm at the U. S. Naval Research Laboratory by Coates. The observing wavelength is in the atmospheric window between the 5 mm oxygen line and the 1.7 mm water-vapor line, and consequently there is considerable atmospheric attenuation from the wings of these lines.

The radio telescope used for these observations had a half-power beamwidth of 6.7 minutes of arc. The antenna reflector was an aluminum paraboloid, 10 feet in diameter with a focal length of 35.8 inches.

A small horn was used to feed the reflector. A specially designed low-loss waveguide section connected the feed horn at the focus of the reflector to the receiver on the back of the antenna.

The polar mount for the antenna was an old radar pedestal, appropriately mounted. The hour-angle drive was controlled with a servo system and the declination drive was operated manually.

The 4.3 mm receiver on the back of the antenna was a Dicke-type radiometer, consisting of a superheterodyne receiver preceded by a calibrated attenuator and a motor-driven attenuator wheel (which modulates the incoming signal), and followed by an audio amplifier, a synchronous detector, and a recording meter.

During calibration, the receiver was designed to obtain scans across the sun for determining the brightness distribution. When observing, the antenna was pointed ahead of the sun and locked in position, and the radiometer output was recorded continuously as the earth's rotation carried the sun through the antenna beam.

The atmospheric attenuation at the zenith, deduced by both sun and sky methods, and the values of the zero-loss antenna temperature for the sun are listed in Table I for several series of measurements made over a period of 6 months. Also included in Table I are results obtained from a measurement of a moonrise. The measured vertical atmospheric attenuations for 4.3 mm were between 1.6 and 2.2 db for clear skies.

A few cloud observations, made by tracking the sun as clouds passed over, indicate additional attenuations of about 0.7 db for fair weather cumulus clouds.

The average of the solar measurements gives 5505°K for the observed solar antenna temperature, after correcting for atmospheric and waveguide attenuation.

By considering the antenna pattern, the antenna temperatures for the moon, and longer wavelength measurements with the Naval Research Laboratory 50-foot antenna, it was estimated that the observed antenna temperature is about 20 percent lower than the solar brightness temperature. Therefore, dividing 5505° by 0.8 gives a value of $7000^\circ \pm 700^\circ\text{K}$ for the 4.3 mm brightness temperature at the central region of the sun. The uncertainty is due mainly to the estimate of the 20 percent factor.

3.3 Aerospace Corporation (Shimabukuro, 1965)

The next significant millimeter program was undertaken at the Aerospace Corporation in Los Angeles by Shimabukuro. The measurements were made at a wavelength of 3.3 mm which is located in the "window" between the complex of absorption lines near 5 mm and the singlet near 2.5 mm. The properties of the 3.3 mm atmosphere are principally determined by the oxygen and the water vapor, although some of the less abundant gases, including those which are man-made, have lines in this wavelength region.

The instrument used for the measurements was a 15-foot, computer-controlled parabolic antenna located at the Aerospace Space Radio Systems Facility. During the period in which the measurements were taken, the sensitivity at the antenna terminals, T_A , which is defined as the rms temperature at the output terminals for a signal-to-noise ratio of unity, was approximately 3°K for a 0.25 cps noise bandwidth.

The attenuation through the atmosphere was determined by measuring the intensity of the sun through different zenith angles. The attenuation curve was obtained in the usual manner. A reading was taken at the center of the sun; then a second reading was taken of the sky 1° away. The main beam (on-axis) and wide beam ("exploded" reference) lines were balanced well enough so that the sky emission difference over a 1° interval was undetectable. The logarithm of difference between the source and the sky background was plotted against the secant of the zenith angle.

The attenuation measurements were usually made in the afternoon to utilize the data from the radiosonde that is released daily at the Santa Monica Airport located 8 miles northwest of the antenna site. The theoretical attenuation coefficients were computed from this data. The measured and calculated values were in fair agreement. This comparison of the calculated and measured attenuations was done for the first 26 days of 1964 when both radiosonde and attenuation data were available. From these results a statistically derived expression for the zenith attenuation was:

$$\alpha(\text{db}) = 0.28 + 0.31 w \quad (16)$$

where w is the precipitable water in cm (the height of water at the surface in that area if all the water vapor in the atmosphere is condensed out).

However, the water vapor distribution is a variable quantity, and the attenuation can be different from day to day even though the precipitable water is the same.

Also, in the expressions for absorption, the important parameter is the line-width, which is proportional to pressure. The oxygen distribution is fairly predictable, and it is expected that for a given area the day to day oxygen attenuation should not

vary greatly. However, there may be seasonal variations if a region has wide temperature ranges. In the case of the water vapor, the distribution is more variable, and changes from day to day can be expected. Generally, it can be stated that for the same amount of precipitable water, the attenuation will be greater when the water vapor is concentrated lower in the atmosphere.

An expression for the atmospheric attenuation was obtained experimentally by plotting the measured attenuation against precipitable water. The intercept was the oxygen attenuation. Measured attenuations on 93 clear afternoons in 1964 were plotted along with the precipitable water obtained from the afternoon radio sounding in Figure 2. The regression line for the points for 95 percent confidence limits (2 σ) gave:

$$\alpha \text{ (db)} = (0.18 \pm 0.08) + (0.04 \pm 0.06) w \quad (17)$$

where w is the precipitable water in cm. It is not presently known whether the difference between Equations (16) and (17) is significant. The regression line for the measurements in which the precipitable water was less than 2 cm gives $\alpha \text{ (db)} = 0.27 + 0.31 w$. Note that the spread of α values given corresponds to a total spread of 10% in the actual values of the solar temperature.

However, the theoretical expressions did predict the actual physical situation well enough to warrant making some general observations about the absorption of the dry atmosphere. The first 3.2 km, which comprises 32 percent of the atmosphere, contributed half of the total attenuation. This was, of course, due to the pressure broadening of the complex of oxygen lines near 5 mm. Less than 1 percent of the attenuation was due to the atmosphere above 17 km.

Measurements also were made to show attenuation changing with time and a best fit curve was calculated assuming a linear time dependence in the attenuation.

From the data on varying attenuation Shimabukuro felt that it was apparent that one should be extremely careful in determining the brightness temperature of extraterrestrial sources in the millimeter wavelength region. If the attenuation was changing linearly with time, an accurate determination of the source temperature could be made by averaging the pre- and post-transit values. In any case, many measurements should be made, both before and after transit, and more statistical weight should be given to those measurements during which the attenuation changes were small.

The effects of thin clouds and thin layers of fog on propagation at 3.3 mm are quite small. In many cases they are undetectable, in the sense that their measured attenuation as compared with that of clear days with a comparable amount of precipitable water is well within the scatter observed. On the other hand, the effect of thick clouds and rain on propagation can be appreciable. The effect of thick cumulus clouds on the attenuation can be seen in Figure 3. Measurements during rain were scarce, but on two occasions zenith attenuations of 3 db and 4 db were measured in drizzling rain. During the 4 db measurement, 0.044 cm of rain fell in 1-1/2 hours; it is not known whether the rainfall rate was uniform.

Also, during this program emission measurements made early in 1964 showed that the zenith emission temperature varied between 48°K and 80°K.

4.0 MEASUREMENT PROGRAM

Data from the observations performed under Modification No. 2 of Contract No. NASw-593, exhibited a considerable degree of scatter (if all data was employed) after being corrected by a secant of the zenith angle type expression whose zenith opacity was determined from ground level values of temperature and humidity. Therefore, Modification No. 3 was initiated to investigate the possibility of deriving on an empirical basis a more suitable form of the atmospheric attenuation correction, together with an estimate of the irreducible portion of the fluctuations in the data produced by the atmosphere. Such corrections would then be employed post facto to reduce the scatter in these previous observations which were eliminated from further consideration due to inconsistent temperature levels.

The need for atmospheric corrections can be readily seen from consideration of the range of zenith angles encountered during any long duration lunar measurement program. Noting that the moon travels from $+23.5^\circ$ to -23.5° declination every 14 days, the resulting variation in the secant of the zenith angle can be seen from Figure 4. Even when observations are confined to ± 1 hour from meridian crossing, in one month the secant has varied from 1.10 to 2.40. Thus, the days when opacity values are high and zenith angles are large, produce lower apparent lunar temperatures which must be corrected if they are to be weighted equally with temperatures taken at other times under clear conditions. Thus, without an adequate correction procedure, many days of observation must be discarded due to unpredictable increases in absorption levels.

4.1 Method of Observation

The observational approach employed was to monitor the intensity of the solar flux at 8.6 mm wavelength under various combinations of ground level temperatures, humidity and cloud covers. The receiving instrument was the Ewen Knight Radio Telescope (located in Needham, Massachusetts) which consisted of a 28-foot diameter parabolic reflector antenna with an 8.6 millimeter superheterodyne radiometric receiver.

The decision to monitor the sun instead of performing "sky" temperature measurements was based on the fact that the near field of the antenna extends to distances of 9 miles. Thus, temperature measurements of the sky would necessarily have required mathematical "unfolding" of complex integrations of near field antenna patterns with the atmospheric temperature profiles which were being observed. Since neither the near field patterns of the antenna nor the exact atmospheric temperature profiles were available for the required data reduction, observations of the sun were the preferable approach to be employed. Although these observations do not remove the problem of the atmosphere being in the near field of the antenna, they do reduce the contribution that the atmospheric temperature makes to the received antenna temperature to less than 1 or 2 percent of the total signal, as shown in Section 2.2.

After preliminary experimentation in late January and early February 1965, with various operational procedures and with familiarization with signal level ranges encountered in normal runs, it was decided to modify the radiometer from the Dicke mode to the total power mode in order to alleviate the necessity of frequent scale shifts and variable calibration signal levels required to maintain 3 percent accuracy. In the total power mode the system noise was approximately 100°K on a peak-to-peak basis when a bandwidth of 8 MHz and a 3-second time constant were employed.

Calibration of the system was accomplished every thirty minutes by switching the input to a terminated load in place of the antenna horn and injecting a 2300°K from a noise tube. With the system operating in this manner, the solar deflection on a Sanborn Recorder was approximately 40 mm, while the calibrate deflection was approximately 28 mm.

4.2 Observational Data

Data was taken on 39 days, between March 4, 1965 and May 11, 1965. Each day's run consisted of a five to six hour period of continuous sun tracking beginning at the time of meridian transit. The usual auxiliary data consisting of surface temperature, relative humidity and a visual estimate of cloud cover were also collected. As an innovation, a simple "cloud detector" was also set up. In particular, this consisted of a General Electric cadmium sulfide diode set on an equatorial mount and manually positioned to follow the sun. From this device, a record of the solar insolation level in the region around $6,000 \pm 600$ Angstroms was obtained. (It was hoped that in using this cloud detector, a correlation might be observed between the extinction and scattering characteristics of clouds and the radiometric absorptive properties, even though it was known that the mechanism for the two effects were quite different.)

The 39 days when data was taken may be broken down into the following meteorological groupings: 11 days were nominally clear; 12 days were overcast, ranging from light hazes to very dark cloud cover; 7 days were partly cloudy; 8 days of precipitation ranging from drizzle to moderate rain, and finally, 1 day with a heavy snowstorm. Figure 5 illustrates typical chart recordings of data on a clear, a hazy, and a misty day. Lower scale numericals in this figure represent the zenith angle of the sun. By means of the photo detector records, however, a better classification of days was obtained. In particular, on 28 out of the 30 days when there was no precipitation, the photo detector record fell within 1 to 5 general groups (shown in Figure 6). In this grouping scheme, clear days are represented as an extremely straight trace showing no structure except the expected downward trend towards the later part of the afternoon. Hazy days exhibit a record of slightly lower level, but with 10% fluctuations in intensity. Partly clear days exhibit periods of high intensity similar to that of a clear day with pronounced decreases ranging from very short durations of one minute to others lasting for 10 to 40 minutes with typical intensity drops of 30%. The fourth group, cloudy days with broken clearings, exhibit a generally lower trace with few flat-topped peaks corresponding to periods of clear sky. The fifth grouping, the completely overcast day, exhibited a trace roughly 40% lower than the clear day with very slow variations of $\pm 15\%$ and a more pronounced decrease toward the later afternoon. Utilizing these trace groupings, 11 days qualified as clear in Group I. Nine days were in Group II with a hazy overcast, 5 days were in Group III with partly cloudy skies, 3 days were in Group IV with heavy overcast with a few clearings, and 3 days were in Group V with total overcast. This grouping procedure was then examined for typical attenuation values and zenith angle variations.

4.3 Data Reduction

In investigating the zenith angle dependence of the antenna temperature, however, a secant-type variation could be observed only in Group I. However, due to the smallness of the opacity on clear days and the inherent accuracy of the measurement, considerable scatter existed, in the determination of opacity. An average value for the opacity of .04 was taken, although individual values ranged from .03 to .08. The days of Group II, the slightly overcast days, exhibited more scatter and as a result

made identification of an exponential secant dependence even more dubious. In most cases, however, the antenna temperatures of the Group II days were no more than 1% lower than the Group I values. The data for Group III days appeared independent of elevation angle with antenna temperatures generally 5% below that of the corresponding clear day. Group IV containing only 3 days, exhibited such scatter and lack of day-to-day correlation, that the radiometric significance of this grouping is in doubt. Finally, Group V containing the days with continuous low overcast, did not show a secant-type dependence, and instead, indicated an average antenna temperature 6% below those on corresponding clear days.

In order to assess the value of atmospheric corrections based on these groupings, rather than on ground level humidity measurements alone, the data spread using various corrections was employed. Each point represented is a 30 minute average of the radiometer output taken at meridian crossing and at 1, 2, 3 and 4 hours later. Figure 8 indicates the same data after correction by a secant-type law with an opacity determined from ground observations of water vapor density. Figure 9 represents again the same data points, this time corrected for cloud attenuation in Group III and V and the previous secant correction in the other three groups. Recalling that the peak-to-peak instrument noise of the radio telescope was $\pm 3\%$, it may be seen from Figure 7 that 68% of the data points fall within the 3% range of the average value, indicating that on the days when observations were made the range of attenuations encountered were small to begin with. In Figure 8, 76% of the data points are within 3% of the average. In Figure 9, 83% are within 3% of the average. Thus, in using both ground humidity and cloud groupings, the number of points outside the $\pm 3\%$ interval was reduced by a factor of two.

The radiometer data was also analyzed for the types and durations of fluctuations typical of the various weather groupings. In Group I, no fluctuations greater than instrument noise of 3% were seen for more than 1.7% of the time. In Group II, days with high thin haze produced slow variations in the antenna temperature that followed the variations in the photo diode record. These variations exhibited periods of 20 to 30 minutes with net amplitudes of 3% of the solar total antenna temperature of 120°K and occurred 3.7% of the time. For the cases of more pronounced hazes, variations up to 5% were noted. However, such variations occurred less than 10% of the observation time. The partly cloudy sky data in Group III did not exhibit any fluctuations for more than 10% of the time. Periods of the fluctuations correlated well to the centers of the darkest clouds passing before the sun. Average durations of such fluctuations were 10 minutes and amplitude changes of 4% were typical also. The Group IV data exhibited the largest fluctuations with peak-to-peak variations up to 15% of the antenna temperature. These variations were most often decreases in intensity lasting approximately 15 minutes each and occupying approximately 25% of the time of observation. Finally, Group V data exhibited less pronounced variation than Group IV, although the net antenna temperatures were lower. Typically, the fluctuations were slow lasting approximately 30 minutes and causing amplitude changes no greater than 10% of the antenna temperature.

4.4 Conclusions

In summary, it can be seen that the use of the photocell data as a grouping discriminant does improve the secant corrected observational data. However, the spread

is still significant and equally good results can be obtained from elimination of the poorer observing days' data. Thus, the procedure followed in these measurements allow the use of more data, but still does not adequately resolve the problem of atmosphere attenuation corrections when only ground level values of temperature and humidity are available.

Taking the above figures as indicative of the March, April, May period of the year, it is noted that on the 9 days (eliminated from the above groupings due to the occurrence of precipitation), observations were eliminated due to typical fluctuations of 30% in the signal. On 11 clear days, fluctuation levels were set by the system noise. For 15% of the remaining 19 days, atmospheric induced fluctuations exceeded the system noise. Thus, for over 31% of the time during which observations were taken, the external fluctuations produced by the atmosphere and its constituents exceeded the system noise level. The overall average of these fluctuations was 10% of the antenna temperature or approximately three times the normal system noise level. Thus, an unavoidable amount of scatter will be introduced on any observations if care is not taken to eliminate nonoptimum meteorological conditions, in spite of the adequacy of the attenuation level correction.

In view of the nature of the results obtained, it is recommended that further measurements of this kind be undertaken with the addition of a photographic record of the cloud features. This information, together with photocell recordings, would allow further refinement of the role played by the various types of cloud formations on the overall attenuation coefficient at 8.6 millimeters. On days of overcast, aerial photographs of the cloud cover distribution should also be obtained, if possible.

Since the ground level values of the temperature and humidity correlate with, but do not form a reliable estimate of the overall opacity on clear and hazy days, it is suggested that the basic parameters entering the opacity expressions, namely the linewidth parameter and collision effectiveness parameters relating linewidths to molecular concentrations, should be re-examined to eliminate much of the existing controversy concerning values of atmospheric opacity for various atmospheric temperature and pressure profiles.

5.0 RADOME CONSIDERATIONS

As noted in the introduction to Part II of this Final Report, a protective, air-supported radome represented a unique feature of the Radio Observatory. The advantages and disadvantages of radomes for various applications has been the subject of several intensive studies. One half of Volume 26 of the M.I.T. Radiation Laboratory Series is devoted to this subject. Radomes for radio telescopes were first investigated in the mid-1950's during the original planning phase for the National Radio Astronomy Observatory. The study at that time was concerned primarily with a protective weather cover for a proposed 600-foot diameter steerable antenna aperture. The radome cost was estimated at \$25,000,000, with an overall size sufficient to house the Empire State Building.

Since that time there have been several additional and more intensive studies. The literature now available on this subject would fill several volumes. In general, the trend has been in favor of radomes, particularly for military applications in which the antenna is subjected to an adverse weather environment. In moderate climates, free of ice, snow and severe wind, the unprotected antenna is most frequently deemed the more appropriate approach, since the protection which the radome offers against the weather elements is by definition not severe in these geographical locations. Relatively few observational sites in the United States meet these requirements, hence, as noted previously, the trend toward greater use of radomes is achieving increasing appeal. Most investigations concentrate greater attention on the type of radome rather than on whether or not a radome will be used.

The advantages afforded by a radome include:

1. Low initial cost for the antenna system as a consequence of the less rugged construction required for protection against wind, hail, and ice loading. This is particularly true of millimeter antenna systems, where the reflecting surface could be easily damaged by hail or be distorted by wind or ice loads. The precision pointing requirements of millimeter antenna systems can be met with a very modest power drive system when protected from wind loading.
2. A radome affords opportunity for temperature control of the antenna structure. Exposure to nonuniform solar illumination and the rapid temperature variations which occur at sunrise and sunset represent a major source of antenna pointing error.
3. The opportunity to perform repair and maintenance operations in a shirt-sleeve environment is conducive to increased instrument performance reliability. Repairs and system performance evaluation can be carried out on a 24-hour-a-day basis. Major repairs can be conveniently scheduled for periods when observing conditions are considered adverse to data accumulation requirements. This is a significant advantage, and is indicative of the success achieved in the program reported here in which down time due to equipment failure during conditions considered appropriate for observation was less than 2%. The 98% equipment

reliability figure achieved under this program was in large part related to the availability of the radome which greatly simplified repair and maintenance procedures and schedules.

4. Within a radome enclosure, critical RF front end components need not be contained in temperature-controlled weatherproof enclosures. This not only minimizes cost, but affords opportunity for quick interchange of relatively simple and easily accessible modular packages designed for laboratory environment.

There is one major disadvantage to a radome which in some applications is considered sufficient to offset all of the advantages noted above. This is the deleterious effect which a radome has on the received signal. If the precise nature of the effect could be predicted and carefully measured, there would be less concern. Unfortunately, a radome is located in the near field or pulsating field of the secondary aperture which is the most complex portion of the electromagnetic field of an antenna. Analytical treatment of this problem is adequate only for initial design considerations. A radome is invariably tested and calibrated with the aid of model studies.

A detailed engineering investigation of the effect on the received signals of the air-supported radome at the Needham Observatory would represent a major effort and require extensive measurements. The alternate and more practical approach which was undertaken during the program was to establish the efficacy of those techniques which would assure performance within limits consistent with observation requirements. It should be noted that a precise measure of radome performance would require a radio source of known intensity located in the far field of the antenna whose position could be adjusted to the various pointing angles required during the lunar observing program. The impracticability of this approach is immediately evident by noting that the far field for the antenna at an 8.6 millimeter wavelength is approximately 70,000 feet, negating even the utility of an instrumented aircraft for measurements of this type.

When the radome is dry its effect on the received signal can be simply represented by an attenuation which is predominantly reflective rather than resistive. The value of the attenuation is frequency dependent; however, it can be very easily measured in the laboratory by standard techniques using a small sample of the radome material. Measurements of this type were performed at our Laboratory and repeated at the University of Texas through the courtesy of Drs. Straiton and Tolbert. These laboratory measurements were then reconfirmed at the Observatory by measuring the relative intensity of a received signal from a beacon located in the far field of the antenna and by a small antenna located external to the radome.

During the early portion of the observing program considerable effort was concentrated on establishing the simplest technique by which the observer would be able to assure that the radome was "dry" and its contribution to the total error would be known.

Under typical low wind conditions the detection of precipitation and condensation products on the radome surface can and was confirmed by visual observation. Of greatest concern was the time interval following a period of precipitation during which the radome was "wet" as a consequence of water absorption. The technique of detecting this condition was fortuitously aided by the radiometric receiver which, in a high sensitivity mode, is easily able to detect the differential effective temperature

contributions of a wet versus dry radome as a function of the elevation angle of observation. By scanning the antenna over a range of elevation angles from near zenith to a few degrees above the horizon, a dry radome will show a response which follows the secant law of the zenith angle typical of atmospheric attenuation. If the radome is wet, two relatively abrupt discontinuities will be noted as a function of the elevation angle, particularly if an exploded-beam horn is used in the comparison mode of operation. The first discontinuity is noted at an antenna elevation angle of approximately 25° , at that point above the horizontal great circle of the radome sphere where water droplets tend to run off and the transition between the upper wet hemisphere and the lower dry hemisphere goes through the most pronounced transition. The next discontinuity is noticed at an elevation angle of approximately 70° where large droplets tend to coalesce and yet remain on the upper portion of the dome. This upper transition point is most noticeable when snow accumulates on the radome, since the near black body characteristics of snow provide a nearly opaque shield across the antenna aperture.

Scanning of the antenna over various elevation angles can be easily achieved by driving the antenna in hour angle only, at the anticipated declination angle of observation. This provides an immediate and conclusive indication of a wet radome condition, indicated by abrupt fluctuations in the RF input balance of the radiometric system.

As a result of these measurements, we conclude that radome effects need not be considered a limiting factor if one takes care in establishing that the radome is dry at the time of observation. The magnitude of the error can then be readily interpreted as an attenuation of the incoming signal with the magnitude of attenuation measurable to a reasonably high precision by standard techniques.

The measurement of radome attenuation should be repeated at regular intervals to detect any change which might be associated with the accumulation of dust or with deterioration of the surface paint. Early in the program the radome was painted. Prior to painting, the surface was thoroughly washed and in the process a considerable amount of black sooty material was removed. Depending on the location of the site and the conducting properties of this soot, one might experience a considerable variation in the radome attenuation characteristics over long periods of time. Regularly scheduled cleaning of the radome is certainly recommended; however, there are a limited number of firms which perform this service and the cost for most research activities is not insignificant (\$3,600 for a 50-foot radome).

In summary, a radome offers several advantages, the most significant being the reduced cost of the antenna system if the radome is considered as part of the instrument during the design phase. If, however, the antenna system has been designed to withstand the rigors of weather conditions at its geographical location, the added expense associated with introducing a radome is questionable. This is particularly true of radio telescopes where survival rather than full operation is the prime requisite. If the instrument is capable of surviving the weather, then the observing periods can be selected with a greater degree of freedom than afforded by a radome. A clear day following a rainy period is most frequently suspect for radome-enclosed antennas. This, of course, would not be the case for an exposed antenna. A radome-enclosed antenna will be inoperative under the mildest conditions of precipitation. An exposed antenna, however, can operate quite successfully under conditions of this type.

There is no simple all inclusive answer to the question of whether radomes should be used or not. The answer depends on the specific application and the geographical location of the instrument.

TABLE I

MEASURED ATMOSPHERIC ATTENUATIONS
AND ANTENNA TEMPERATURES
(Coates, 1958)

Source	Date	Vertical Atmospheric Attenuation		Corrected Antenna Temperature Θ
		A) Sunrise and Moonrise Measurements	B) Atmospheric Radiation Measurements	
Sun	September 10, 1956	1.8 ± 0.3 db	---	5330°K
	October 1, 1956	1.9 ± 0.1	2.0 ± 0.2 db	5620
	October 12, 1956	—	2.2 ± 0.3	5956
	November 15, 1956	1.6 ± 0.2	1.7 ± 0.3	5250
	December 4, 1956	1.6 ± 0.2	1.8 ± 0.3	5594
	February 12, 1957	—	1.9 ± 0.2	5880
Moon	November 15, 1957	1.7 ± 0.3	1.8 ± 0.3	202°K

Average Θ run = 5605°K

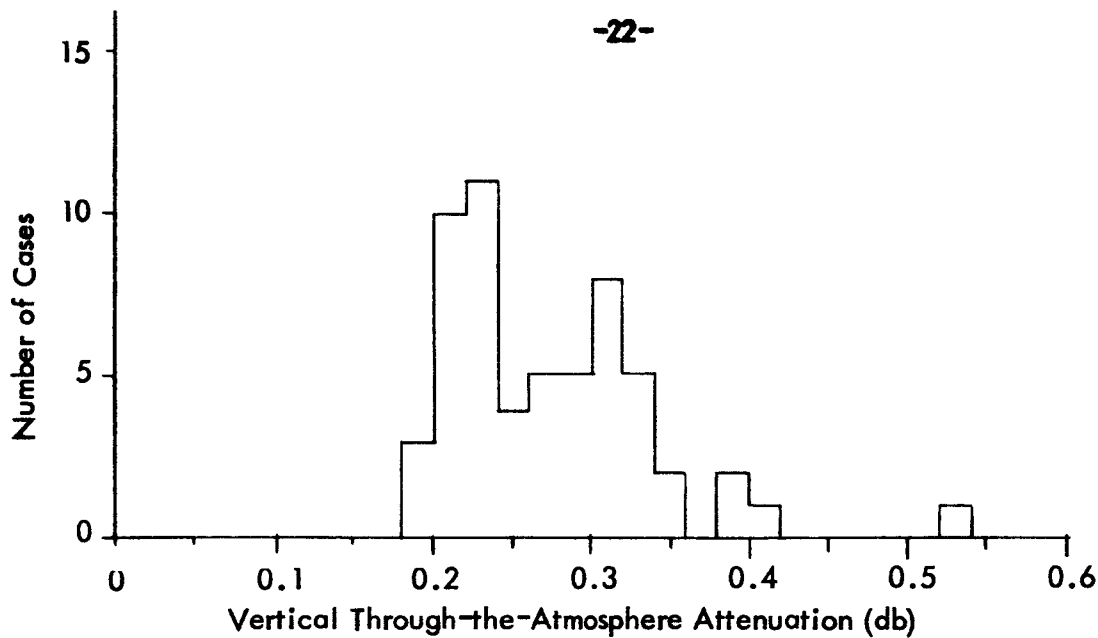


Figure 1

Histogram of Measured Daily Medians of Vertical Through the Atmosphere Attenuation at 8.6 MM During Period December 1962 Through April 1963.(Lee and Waterman 1964)

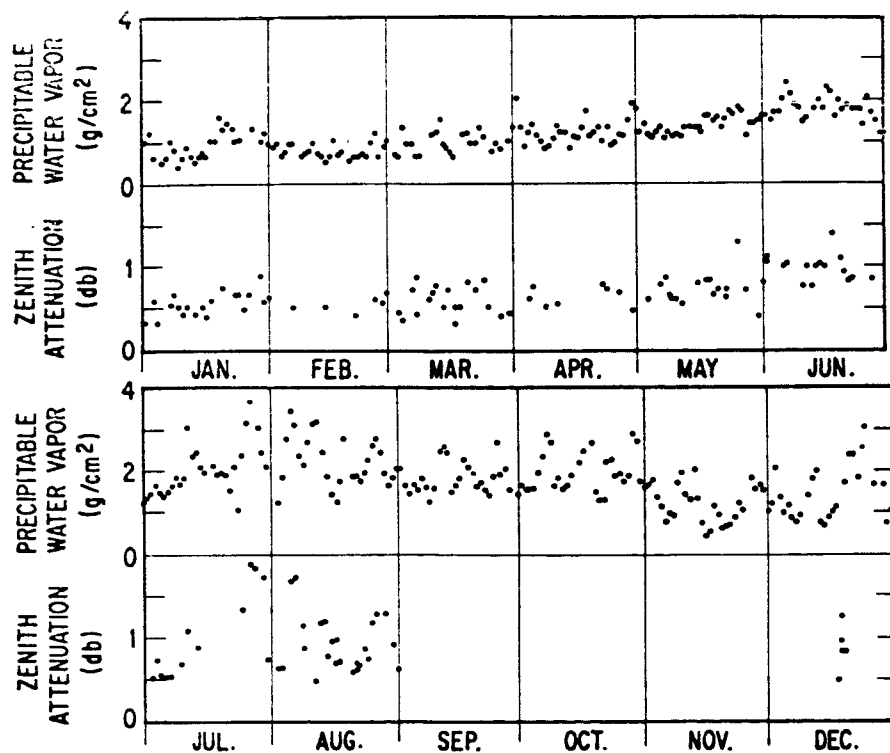


Figure 2

Summary of Zenith Attenuation at 3.2 MM and Precipitable Water Vapor for the Year 1964.
(Shimabukuro, 1965)

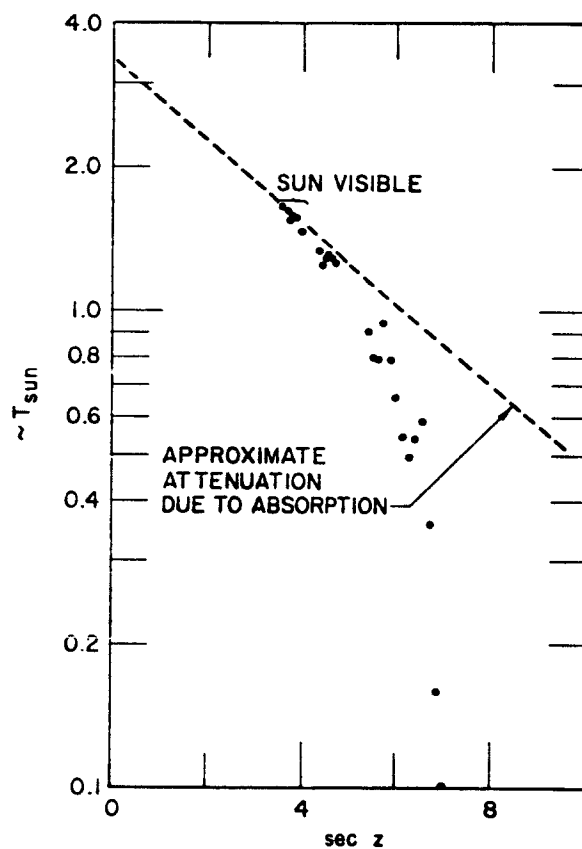
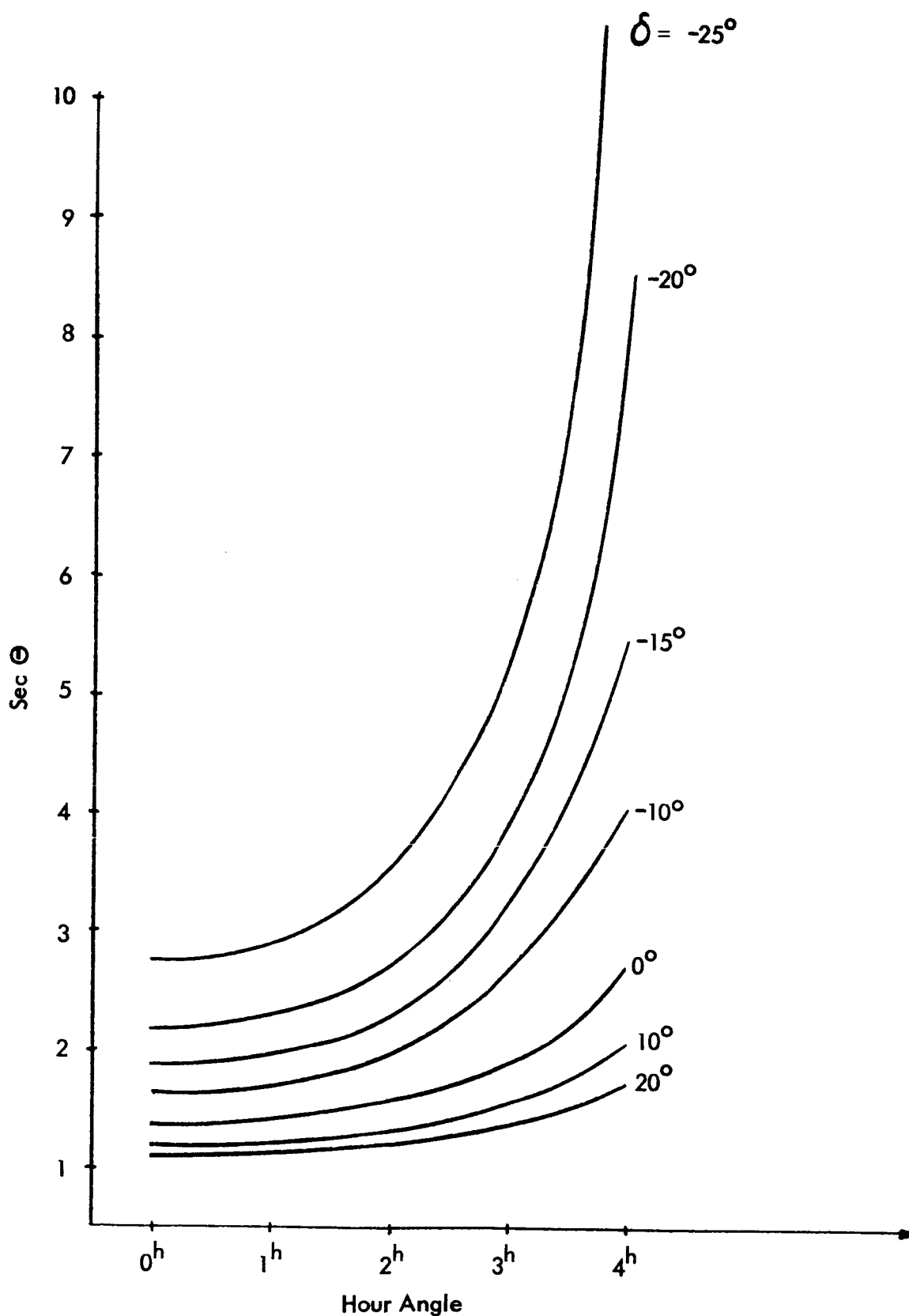


Figure 3

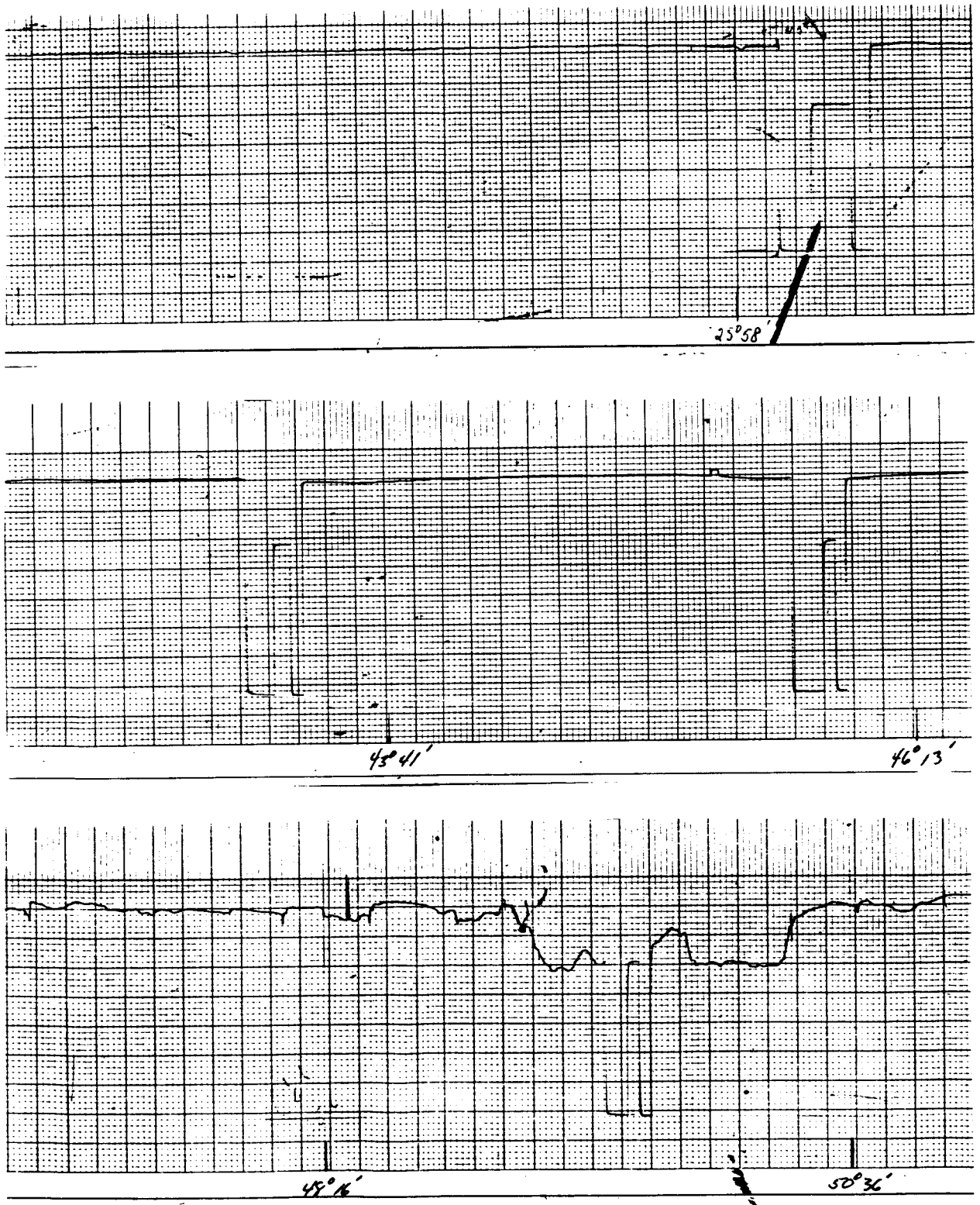
Effect of Thick Clouds on Attenuation

(Shimab ukuro, 1965)



SECANT OF ZENITH ANGLE VERSUS HOUR ANGLE AND DECLINATION, δ

FIGURE 4



TYPICAL SOLAR RECORDINGS

FIGURE 5

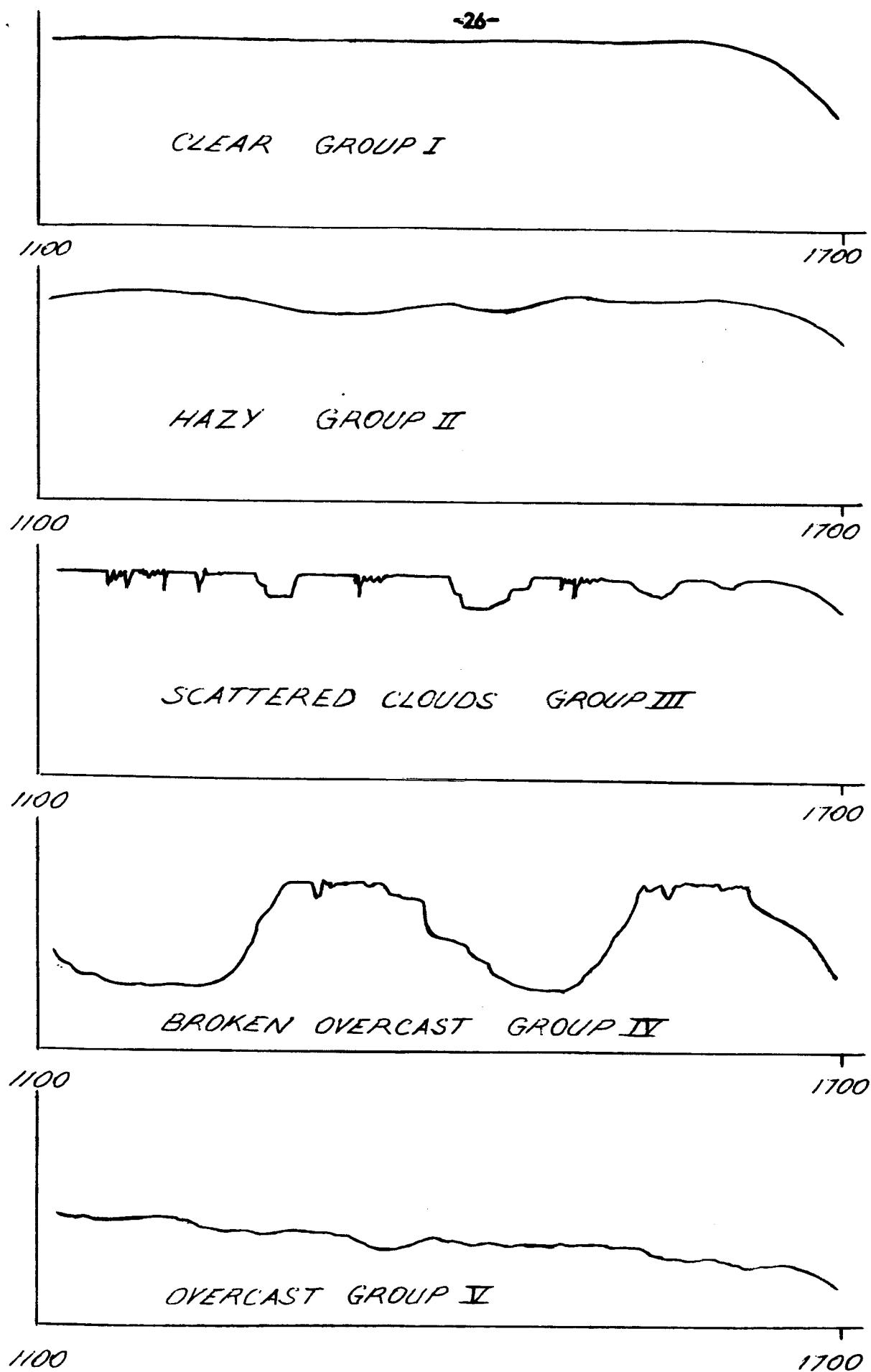


Figure 6

Photodetector Weather Groupings

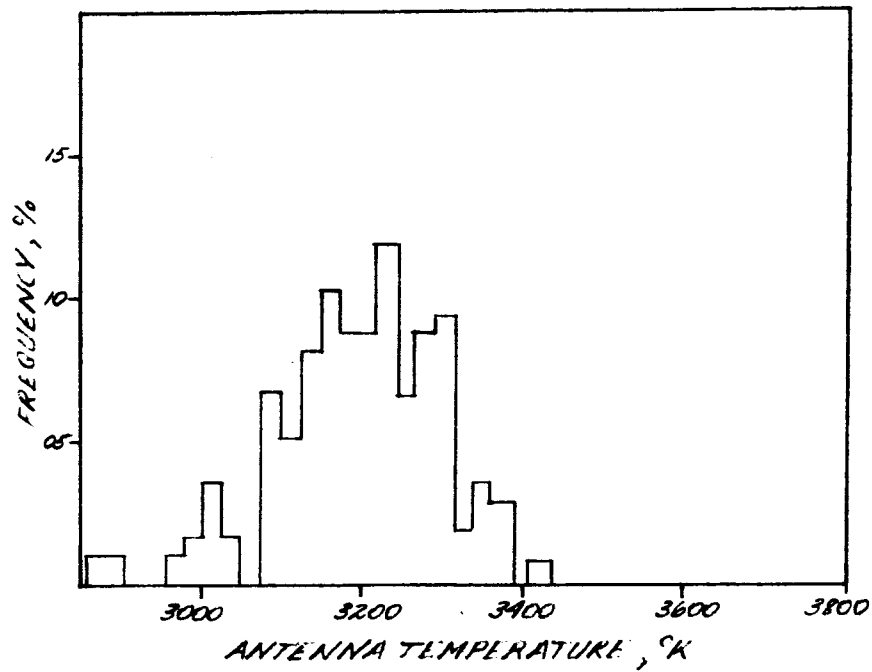


FIGURE 7
CALCULATED DATA DISTRIBUTION

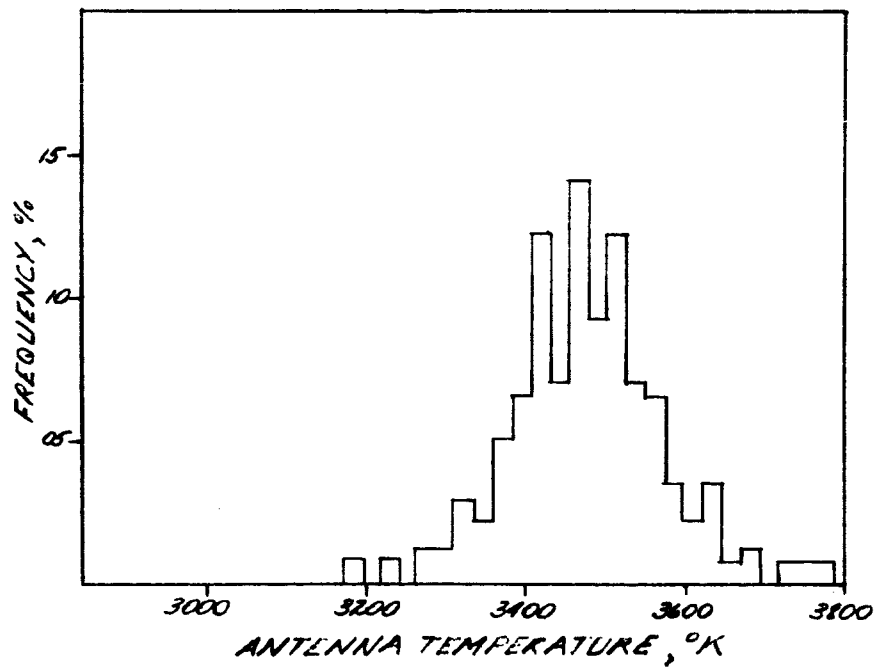


FIGURE 8
SELECTED DATA DISTRIBUTION

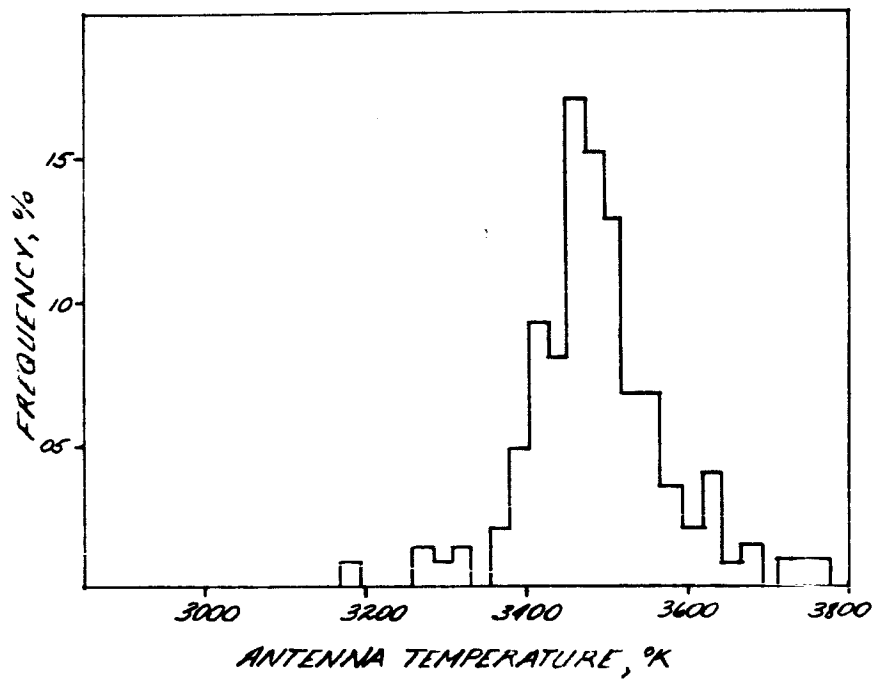


FIGURE 9
MODIFIED SIGANT CORRECTED
DISTRIBUTION

REFERENCES

- Chandrasekhar, S. (1960), Radiative Transfer, p. 1, (Dover Publications, New York, N.Y.).
- Coates, R. J. (1958), Measurements of Solar Radiation and Atmospheric Attenuation at 4.3 Millimeters Wavelength, Proc. IRE, 46, p. 122-126, January 1958.
- Goody, R. M. (1964), Atmospheric Radiation, p. 29, (Oxford, Clarendon Press).
- Lee, R. W. and A. T. Waterman (1964), A Daily Record of Total Atmospheric Absorption at 8.6mm, Proc. 5th International Symposium on Space Technology and Science, 1964.
- Meeks, M. L. and A. E. Lilley (1963), The Microwave Spectrum of Oxygen in the Earth's Atmosphere, J. Geophys. Res. 68, no. 6, p. 1683-1703, March 15, 1963.
- Pawsey, J. L. and R. N. Bracewell (1955), Radio Astronomy, Ch. 2 (Oxford, Clarendon Press).
- Shimabukuro, F. I. (1965), Propagation Through The Atmosphere at A Wavelength of 3.3mm, Aerospace Corporation Report TDR-469(5230-41)-2, June 1965.
- Westwater, E. R. (1965), Ground Based Posane Probing Using Microwave Spectrum of Oxygen, Radio Science, 69D, no. 9, p. 1201-1211, September 1965.
- Wulfsberg, K. N. (1964), Apparent Sky Temperatures at Millimeter Wave Frequencies, Phys. Sci. Res. Paper No. 38, Air Force Cambridge Research Laboratories, July 1964.

ADDENDUM

PART II

ATMOSPHERIC CHARACTERISTICS

1.0 ATTENUATION BY ATMOSPHERIC GASES (Westwater et al, 1964)

The major atmospheric gases that are absorptive in the frequency range of 10 to 100 Gc/s are water vapor and oxygen. In this frequency range the gaseous absorption arises principally in the 1.35 cm line (22.235 Gc/s) of water vapor and the series of lines centered around 0.5 cm (60.0 Gc/s) of oxygen (Van Vleck, 1947a). The variations of these absorptions with pressure, frequency, temperature, and humidity are described by the Van Vleck (1947a, b) theory of absorption. The frequency dependence of these absorptions is shown in Figure 1 (Van Vleck, 1947a). Since water vapor absorption is directly proportional to the absolute humidity (Van Vleck, 1951), variations in signal intensity due to water vapor absorption may be specified directly in terms of the variations in the absolute humidity of the atmosphere.

It can be seen from Figure 1 that the water vapor absorption exceeds the oxygen absorption in the frequency range 13 Gc/s to 32 Gc/s indicating that in this frequency range the total absorption will be the more sensitive to changes in the water vapor content of the air, while outside this frequency range the absorption will be more sensitive to changes in oxygen density. The absorption equations and the conditions under which they are applicable have been discussed by Van Vleck (1947a).

The Van Vleck theory describes these absorptions in the following manner: The oxygen absorption in decibels per kilometer (γ) at $T = 293^\circ\text{K}$ and at standard atmospheric pressure, is given by the expression:

$$\frac{0.34}{\lambda^2} \left[\frac{\Delta\nu_1}{\frac{1}{\lambda^2} + \Delta\nu_1^2} + \frac{\Delta\nu_2}{\left(2 + \frac{1}{\lambda}\right)^2 + \Delta\nu_2^2} + \frac{\Delta\nu_2}{\left(2 - \frac{1}{\lambda}\right)^2 + \Delta\nu_2^2} \right] = \gamma_1 \quad (1)$$

where λ is the wavelength (cm) for which the absorption is to be determined and where $\Delta\nu_1$ and $\Delta\nu_2$ are line width factors with dimensions of cm^{-1} . This formula is based on the approximations of collision broadening theory. The term in (1) involving $\Delta\nu_1$ gives the nonresonant absorption arising from the zero frequency line of oxygen molecules while the terms involving $\Delta\nu_2$ describe the effects of the several natural resonant absorptions of the oxygen molecule which are in the vicinity of 0.5 cm wavelength. The $(2 + 1/\lambda)$ (cm^{-1}) terms are the portion of the shape factors that describe the decay of the absorption at frequencies away from the resonant frequency (the number 2 is the reciprocal of the centroid resonant wavelength 0.5 cm).

The water vapor absorption at 293°K arising from the 1.35 cm line γ_2 , is given by:

$$\gamma_2 = \frac{3.5 \times 10^{-3}}{\lambda^2} e \left[\frac{\Delta\nu_3}{\left(\frac{1}{\lambda} - \frac{1}{1.35}\right)^2 + \Delta\nu_3^2} + \frac{\Delta\nu_3}{\left(\frac{1}{\lambda} + \frac{1}{1.35}\right)^2 + \Delta\nu_3^2} \right] \quad (2)$$

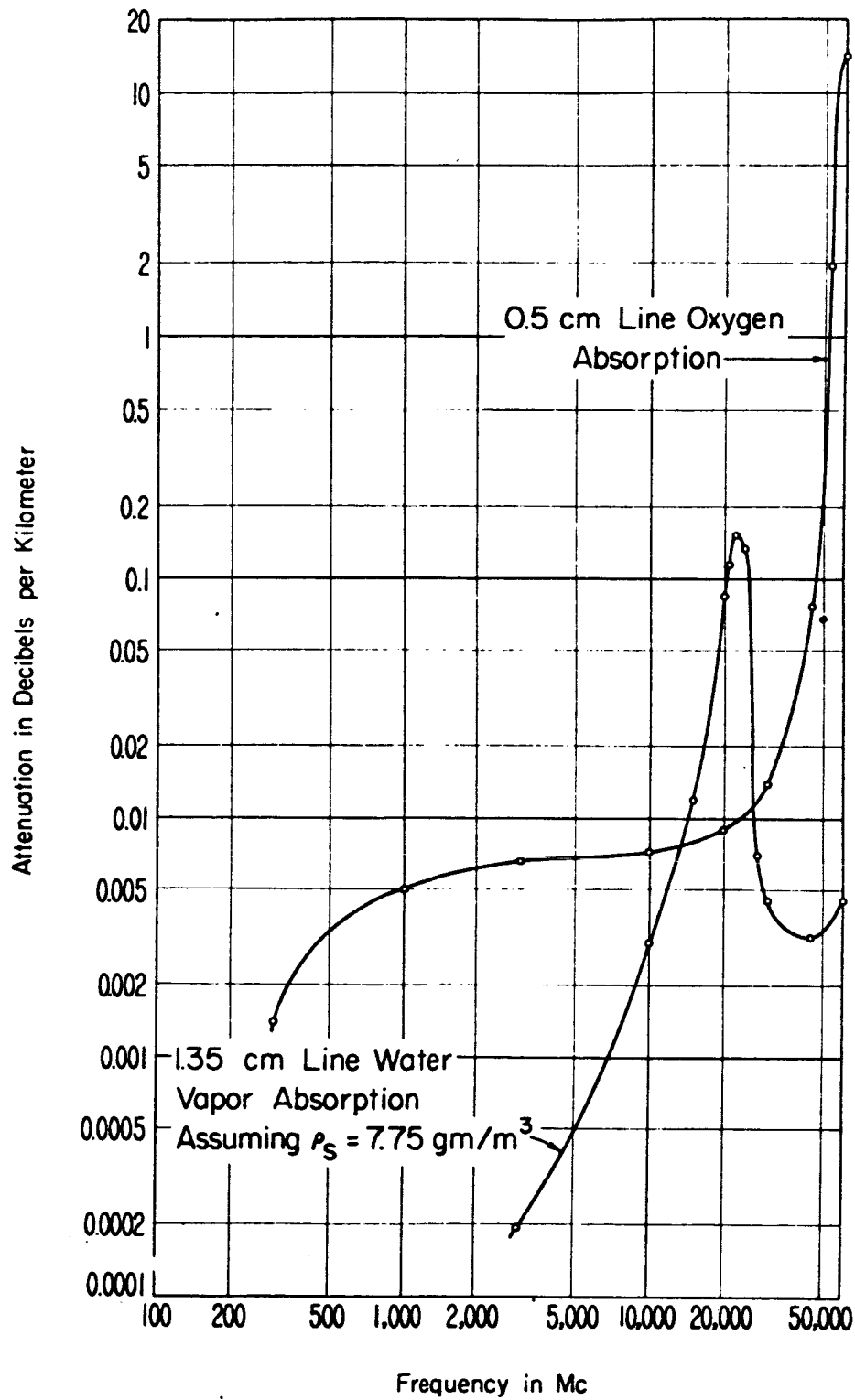


Figure 1 Attenuation of radio waves in oxygen and water vapor.
(Westwater et al, 1964)

where e is the absolute humidity in g/m^3 and $\Delta\nu_3$ is the linewidth factor of the 1.35 cm water vapor absorption line. The additional absorption arising from absorption bands above the 1.35 cm line, γ_3 , is described by:

$$\gamma_3 = \frac{.05 \Delta\nu_4}{\lambda^2} \rho \quad (3)$$

where $\Delta\nu_4$ is the effective linewidth of the absorption bands above the 1.35 cm line. The nonresonant term has been increased by a factor of 4 over the original Van Vleck formula in order to better satisfy experimental results (Becker and Autler, 1946). The particular linewidth values used in computing the absorption coefficients are given in Table 1.

1.1 Pressure and Temperature Dependence

The preceding expressions for gaseous absorption do not reflect the pressure and temperature sensitivity of either the numerical intensity factor or the linewidths. This sensitivity must be considered for the present application since it is necessary to consider the manner in which the absorption varies with temperature and pressure throughout the atmosphere. The dependence of intensity factors upon atmospheric pressure and temperature variation is considered to be that given by the Van Vleck theory. The magnitude and temperature dependence of the linewidths is a question not completely resolved. Both theory and experiment indicate the linewidth to vary as $1/T^x$, $x > 0$. Different measurements on the same line of oxygen have given values of x ranging from 0.71 to 0.90 with differences in the magnitude of $\Delta\nu$ of about 20 per cent (Tinkham and Strandberg, 1955; Hill and Gordy, 1954). Experiments have also clearly indicated that the linewidth changes from line to line, with maximum fluctuations of about 15 per cent. In the frequency region considered here (10 - 90 Gc/s), the centroid frequency approximation for oxygen is valid and a mean linewidth can be used with reasonable accuracy, but in the region of the resonant frequencies of oxygen, the line-to-line linewidth variations must be taken into account. The expressions used to calculate the absorption are given in Table 2. In Table 2, P is expressed in millibars, T in $^\circ\text{K}$, e in gms/M^3 , and λ in cm.

The reference temperatures and pressures given are those at which the appropriate experimental determinations were made. A detailed discussion of the theoretical aspects of the pressure and temperature dependence is given by Artman (1953).

Experimental measurements on the absorption of microwaves by the atmosphere show different values of the loss than those obtained by theoretical prediction methods. There is reasonably good agreement between the predicted and measured loss for oxygen, but the measured loss of water vapor is considerably greater than that of the predicted amount, particularly above 40 Gc/s (Straiton and Tolbert, 1960).

In applying the above considerations to absorption approximations, it also must be remembered that for a given relative humidity, the density will vary considerably with temperature. Table 3 shows attenuation by water vapor at various temperatures and wavelengths.

The oxygen absorption occurs because of a large number of lines around 60 Gc/s. In the region from 3 to 45 Gc/s the attenuation is proportional to P^2 and $T^{-11/4}$. As the temperatures decrease the attenuation increase gradually. At -40°C oxygen attenuation

TABLE 1

LINEWIDTH FACTORS USED TO DETERMINE ATMOSPHERIC ABSORPTION

<u>Linewidth</u>	<u>Temperature</u>	<u>Value</u>	<u>Source</u>
$\Delta\nu_{1,0}$	293°K	$0.018 \text{ cm}^{-1} \text{ atmos.}^{-1}$	Birnbaum and Maryott (1955)
$\Delta\nu_{2,0}$	300°K	$0.049 \text{ cm}^{-1} \text{ atmos.}^{-1}$	J. O. Artman and J. P. Gordon (1954)
$\Delta\nu_{3,0}$	318°K	$0.087 \text{ cm}^{-1} \text{ atmos.}^{-1}$	G. E. Becker and S. H. Autler (1946)
$\Delta\nu_{4,0}$	318°K	$0.087 \text{ cm}^{-1} \text{ atmos.}^{-1}$	G. E. Becker and S. H. Autler (1946)

Table 2
Values Used in the Calculation of Atmospheric Absorption

Absorption [db/km]	Intensity Factor	Line Width [cm ⁻¹]
γ_1	$\frac{.34}{\lambda^2} \left(\frac{P}{1013.25} \right) \left(\frac{293}{T} \right)^2$	$\Delta\nu_{1,0} \left(\frac{P}{1013.25} \right) \left(\frac{293}{T} \right)^{\frac{3}{4}}$ and $\Delta\nu_{2,0} \left(\frac{P}{1013.25} \right) \left(\frac{300}{T} \right)^{\frac{3}{4}}$
$\gamma_2 \frac{\gamma_2}{\rho}$	$\frac{.0318}{\lambda^2} \left(\frac{293}{T} \right)^{\frac{5}{2}} \exp \left(-\frac{644}{T} \right)$	$\Delta\nu_{3,0} \left(\frac{P}{1013.25} \right) \left(\frac{318}{T} \right)^{\frac{1}{2}} (1 + .0046\rho)$
$\gamma_3 \frac{\gamma_3}{\rho}$	$\frac{.05}{\lambda^2} \left(\frac{293}{T} \right)$	$\Delta\nu_{4,0} \left(\frac{P}{1013.25} \right) \left(\frac{318}{T} \right)^{\frac{1}{2}} (1 + .0046\rho)$

Table 3
Water Vapor Attenuation (One way) in db/km [After Gunn-East]
P, pressure in atmospheres; ρ water vapor content in g/m³

T(°C)	$\lambda(\text{cm})$	10	5.7	3.2	1.8	1.24	0.9					
20	0.07×10^{-3}	P ρ	0.24×10^{-3}	P ρ	0.7×10^{-3}	P ρ^*	4.3×10^{-3}	P ρ^*	22.0×10^{-3}	P ρ^{-1}	9.5×10^{-3}	P ρ
0	0.08×10^{-3}	P ρ	0.27×10^{-3}	P ρ	0.8×10^{-3}	P ρ	4.8×10^{-3}	P ρ^*	23.3×10^{-3}	P ρ^{-1}	10.4×10^{-3}	P ρ
-20	0.09×10^{-3}	P ρ	0.30×10^{-3}	P ρ	0.9×10^{-3}	P ρ	5.0×10^{-3}	P ρ^*	24.6×10^{-3}	P ρ^{-1}	11.4×10^{-3}	P ρ
-40	0.10×10^{-3}	P ρ	0.34×10^{-3}	P ρ	1.0×10^{-3}	P ρ	5.4×10^{-3}	P ρ^*	26.1×10^{-3}	P ρ^{-1}	12.6×10^{-3}	P ρ

* The pressure dependencies shown are only approximate. Near 1.35 cm water vapor absorption line (between 1.0 cm and 2.0 cm) no simple power is accurate.

Table 4
Pressure and Temperature Correction for Oxygen Attenuation for Wavelengths
between 0.7 and 10 cm [After Gunn-East]

T (°C)	Factor (P is pressure in atmospheres)
20	1.00 P ²
0	1.19 P ²
-20	1.45 P ²
-40	1.78 P ²

is about 78 per cent higher than at 20°C due to increased density at low temperatures. Table 4 shows the pressure and temperature corrections for oxygen attenuation at wavelengths between 0.7 and 10 cm.

Figure 2 shows the attenuation at a pressure of 1 atmosphere and 20°C as a function of wavelength (Gunn and East, 1954). Curve (a) shows oxygen attenuation at 1 atmosphere pressure and 293°K, using $\Delta\nu = 0.039 \text{ cm}^{-1}$ for the 0.5 cm lines and $\Delta\nu = 0.02 \text{ cm}^{-1}$ for the zero frequency line, (b) shows again oxygen attenuation using $\Delta\nu$ values of 0.039 and 0.50 cm^{-1} respectively, curve (c) shows water vapor attenuation due to a water content of 1 gm/m^3 . In (c) the solid lines represent values of attenuation measured by Becker and Autler (1946), and the dashed line is calculated from the Van Vleck Formula.

1.3 Additional Atmospheric Constituents

In addition to oxygen and water vapor, there are a number of other atmospheric gases which have absorption lines in the microwave region from 10 to 100 Gc/s. These gases normally constitute a negligible portion of the general composition of the atmosphere, but could conceivably contribute to attenuation. Table 5 shows the resonant frequencies, maximum absorption coefficients at 300°K (attenuation coefficient if the fraction of molecules present were equal to unity), expected concentration in the atmosphere, and expected absorption coefficients due to these trace constituents. The data on molecular absorption coefficients were taken from Ghosh and Edwards (1956), that on concentrations from the Compendium of Meteorology (1951). It is readily seen that the attenuation due to these sources is negligible compared to the absorption due to oxygen and water vapor.

2.0 ATTENUATION BY METEOROLOGICAL ELEMENTS

2.1 Clouds

Cloud droplets are regarded here as those water or ice particles having radii smaller than 100μ or 0.01 cm. For wavelengths of incident radiation well in excess of 0.5 cm, the attenuation becomes independent of the drop size distribution. The generally accepted equations for attenuation by clouds usually show the moisture component of the equations in the form of the liquid water content (g/m^3). Observations indicate that the liquid water concentration in clouds generally ranges from 1 to 2.5 g/m^3 (Donaldson, 1955), although Weickmann and aufm Kampe (1953) have reported isolated instances of cumulus congestus clouds with a reading of 4.0 g/m^3 in the upper levels. In ice clouds it will rarely exceed 0.5, and is often less than 0.1 g/m^3 . The attenuation in db/km of cloud drops may be written as:

$$K = K_1 M$$

where:

$$\begin{aligned} K_1 &= \text{attenuation coefficient in db/km/g/m}^3 \\ M &= \text{liquid-water content in g/m}^3 \end{aligned}$$

Values of K_1 by ice and water clouds are given for various wavelengths and temperatures by Gunn and East (1954) in Table 6.

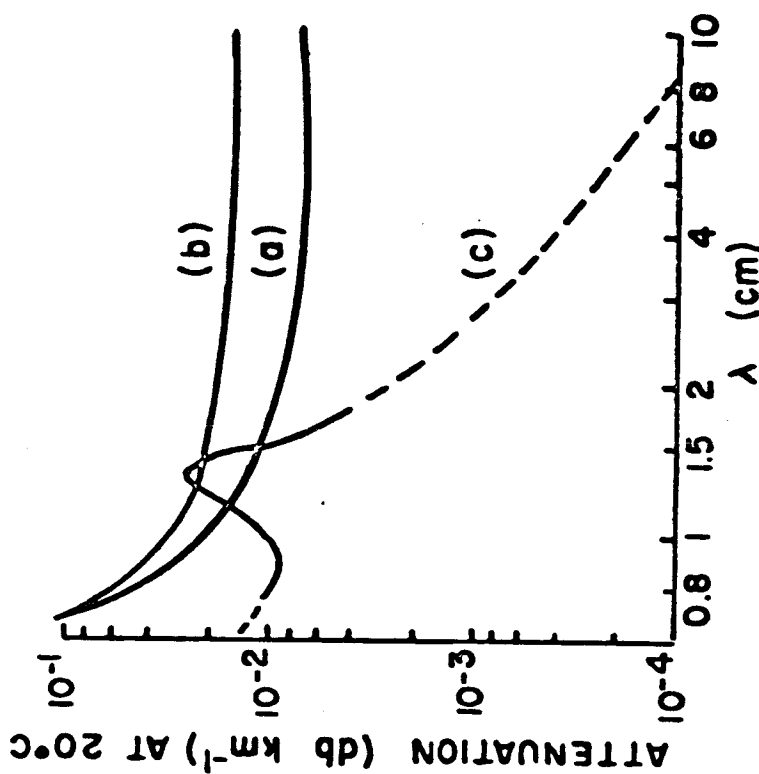


Figure 2 Atmospheric attenuation versus wavelength. (a) Attenuation due to O₂ in air at 1 atmosphere pressure and 293°K, using $\Delta\nu = 0.039 \text{ cm}^{-1}$ for zero-frequency line. (b) As (a), using $\Delta\nu = 0.039 \text{ cm}^{-1}$ for 5 mm lines and $\Delta\nu = 0.05 \text{ cm}^{-1}$ for zero-frequency line. (c) Attenuation due to 1 gm⁻³ of water vapour in atmosphere: full line, measured (Becker and Autler, 1946); dashed line, calculated.

Table 5

Expected Absorption Coefficients of Trace Atmospheric Constituents
At 300°K (Westwater et al, 1964)

Gas	$\nu(\text{Mc})$	$\gamma_{\text{max}}(\text{db/km})$	% by volume at ground	$\gamma(\text{db/km})$ at ground
SO_2	12,258.17	1.9×10^{-1}	$(0 \text{ to } 1) \times 10^{-6}$	$(0 - 1.9) \times 10^{-7}$
	12,854.54	8.7×10^{-1}		$(0 - 8.7) \times 10^{-7}$
	23,433.42	1.2×10^{-1}		$(0 - 1.2) \times 10^{-7}$
	24,304.96	2.3		$(0 - 2.3 \times 10^{-6})$
	25,398.22	2.1		$(0 - 2.1) \times 10^{-6}$
	29,320.36	3.3		$(0 - 3.3) \times 10^{-6}$
	44,098.62	5.2		$(0 - 5.2) \times 10^{-6}$
	52,030.60	9.5×10^{-1}		$(0 - 9.5) \times 10^{-7}$
N_2O	24,274.78	2.5	0.5×10^{-6}	1.25×10^{-6}
	22,274.60	2.5		1.25×10^{-6}
	25,121.55	2.5		1.25×10^{-6}
	25,123.25	2.5		1.25×10^{-6}
NO_2	26,289.6	2.9	$(0 \text{ to } 2) \times 10^{-8}$	$(0 \text{ to } 5.8) \times 10^{-8}$
O_3	10,247.3	9.5×10^{-2}	Summer $(0 \text{ to } .07) \times 10^{-6}$ Winter $(0 \text{ to } .02) \times 10^{-6}$	$(0 \text{ to } 6.3) \times 10^{-9}$
	11,075.9	9.1×10^{-2}		$(0 \text{ to } 6.3) \times 10^{-9}$
	42,832.7	4.3×10^{-1}		$(0 \text{ to } 2.8) \times 10^{-8}$

TABLE 6

ONE-WAY ATTENUATION COEFFICIENT, K_1 , IN CLOUDS

IN DB/KM/GM/M³

(Westwater et al, 1964)

Temperature (°C)		Wavelength (cm)			
		0.9	1.24	1.8	3.2
Water Cloud	20	0.647	0.311	0.128	0.0483
	10	0.681	0.406	0.179	0.0630
	0	0.99	0.532	0.267	0.0858
	-8	1.25	0.684	0.34(extra-polated)	0.112(extra-polated)
Ice Cloud	0	8.74×10^{-3}	6.35×10^{-3}	4.36×10^{-3}	2.46×10^{-3}
	-10	2.93×10^{-3}	2.11×10^{-3}	1.46×10^{-3}	8.19×10^{-4}
	-20	2.0×10^{-3}	1.45×10^{-3}	1.0×10^{-3}	5.63×10^{-4}

Several important facts are demonstrated by Table 6. The decrease in attenuation with increasing wavelength is clearly shown. The values change by about an order of magnitude for a change of λ from 1 to 3 cm. The data presented here also show that attenuation increases with decreasing temperature. Ice clouds give attenuations about two orders of magnitude smaller than water clouds of the same water content. Thus, the attenuation of microwaves by ice clouds can be neglected for all practical purposes (Battan, 1959).

2.2 Rain

Ryde and Ryde (1945) calculated the effects of rain on microwave propagation and showed that absorption and scattering effects of raindrops become more pronounced at the higher microwave frequencies where the wavelength and the raindrop diameters are more nearly comparable. In the 10 cm band and at lower wavelengths the effects are appreciable, but at wavelengths in excess of 10 cm the effects are greatly decreased. It is also known that suspended water droplets and rain have an absorption rate in excess of that of the combined oxygen and water vapor absorption (Bean and Abbott, 1957).

In practice it has been convenient to express rain attenuation as a function of the precipitation rate, R , which depends on both the liquid water content and the fall velocity of the drops, the latter in turn depending on the size of the drops.

Ryde studied the attenuation of microwaves by rain and showed that this attenuation in db/km can be approximated by:

$$K_R = K \int_0^r [R(r)]^\alpha dr \quad (4)$$

where:

K_R = total attenuation in db

K = constant

$R(r)$ = rainfall rate

r = length of propagation path in km

α = constant

Laws and Parsons (1943) observed the distribution of drop sizes for various rates of fall on a horizontal surface. The higher the rainfall rate, the larger the drops, and also the greater the range in size of the drops. However, in order to derive the size distributions occurring while the drops are falling freely in the air, each value must be divided by the particular velocity of fall appropriate to the corresponding drop diameter. Figure 3 shows the resulting distribution in air, expressed as the per cent of total measured precipitation versus diameter, for three chosen representative values of precipitation rate, P , namely, 2.5 mm/hr., 25 mm/hr., and 100 mm/hr. (Ryde, 1946). Figure 4 (Hathaway and Evans,

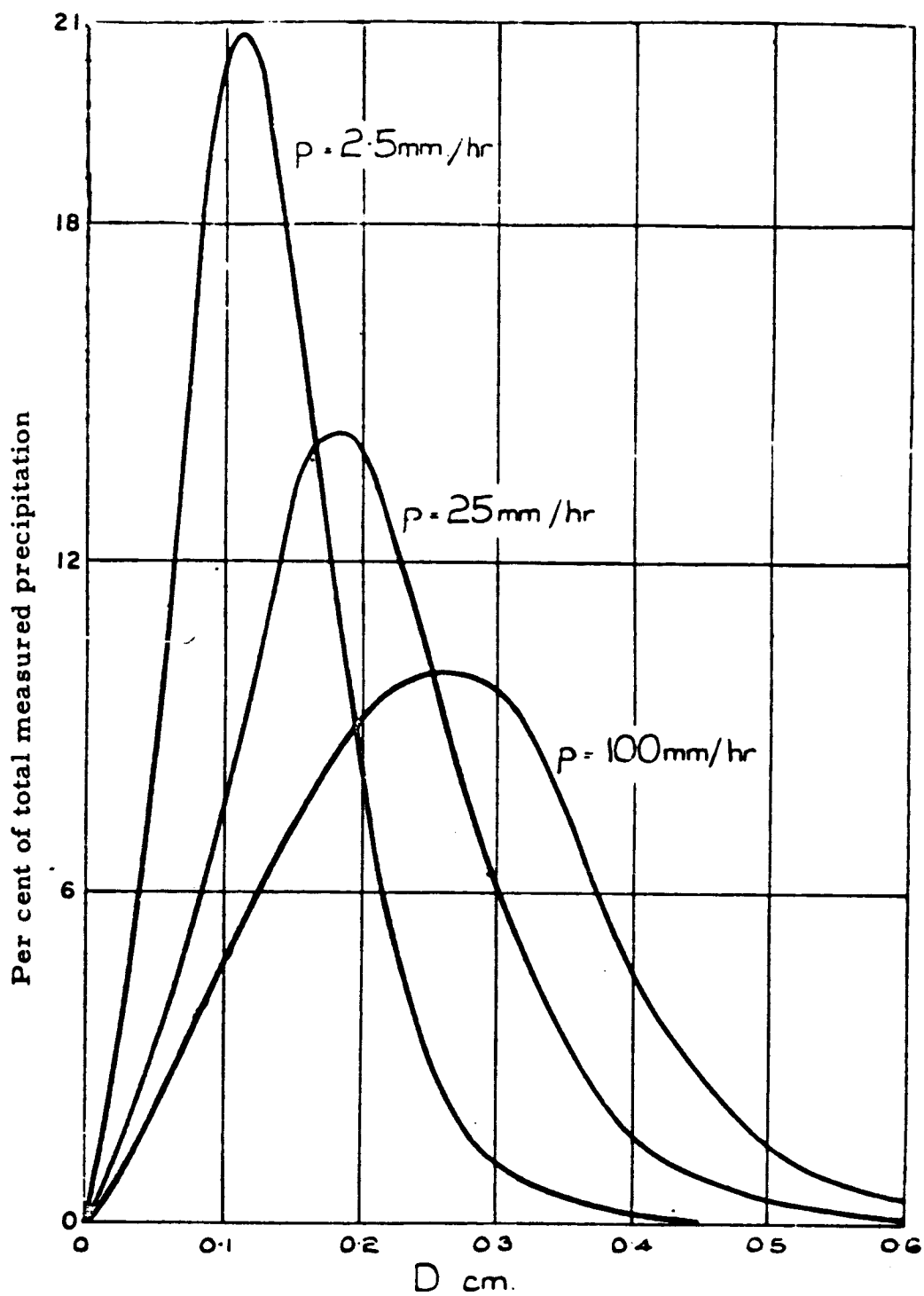


Figure 3 Per cent of total measured precipitation of raindrops as a function of drop diameter for various precipitation rates.
(Westwater et al, 1964)

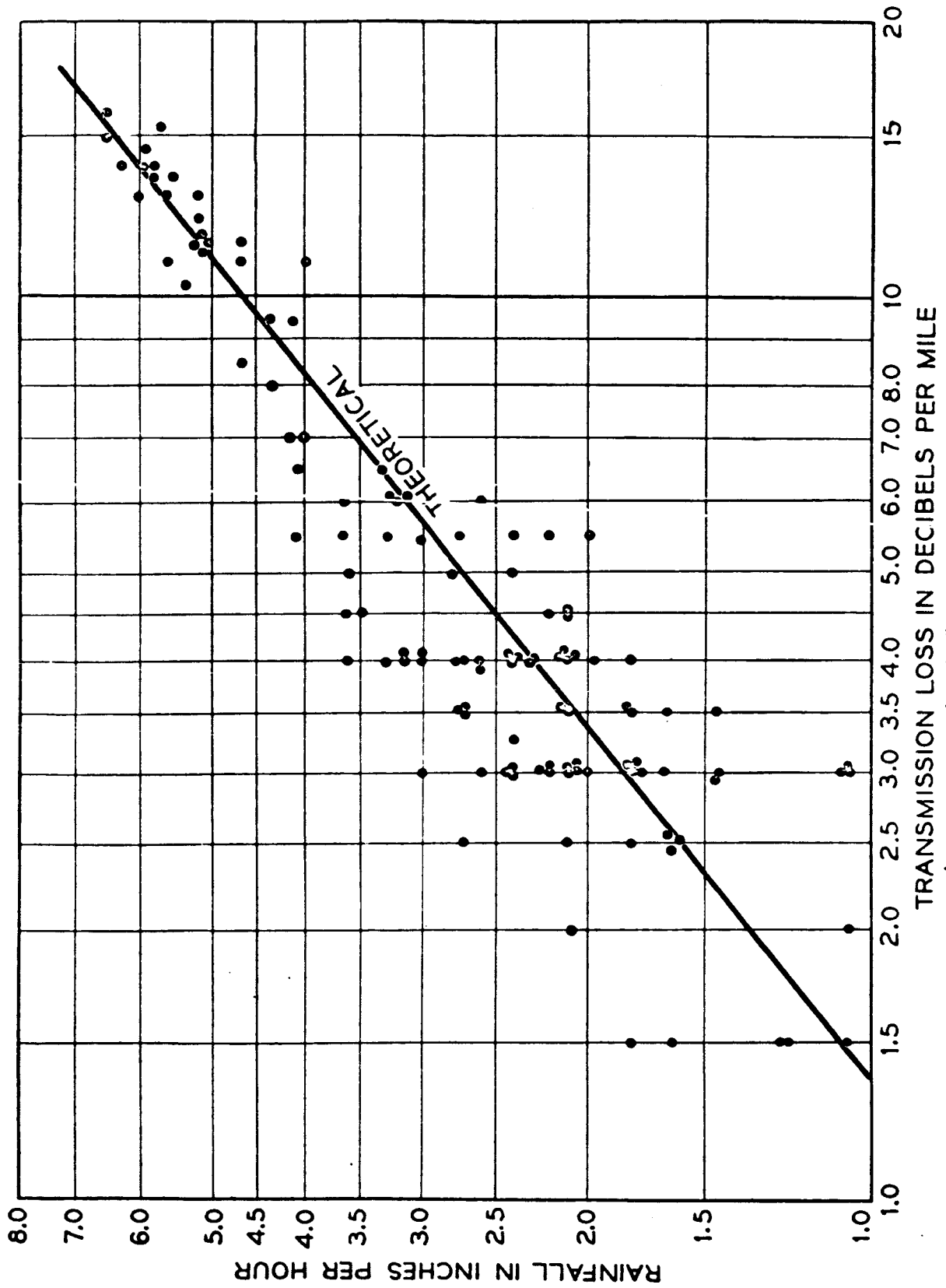


Figure 4 Transmission Loss Due to Rainfall
(Westwater et al, 1964)

1959) is a scatter diagram showing transmission loss versus rainfall rate. For comparison, Ryde's equation is also plotted on Figure 4.

The greatest uncertainty in predictions of attenuation due to rainfall, using theoretical formulae as a basis for calculation, is the extremely limited knowledge of drop size distribution in rains of varying rates of fall observed under differing climatic and current weather conditions. There is little evidence that a rain with a known rate of fall has a unique drop size distribution though studies on this problem seem to indicate that a most probable drop size distribution can be attached to a rain of given rate of fall (Laws and Parsons, 1943). Table 7 shows the percentage of total volume of rainfall occupied by raindrops of different diameters (cm) and varying rainfall rates (mm/hr). Tables 7 and 8 are offered as an aid to estimating, through a qualitative approach, the attenuation of radio waves by raindrops (Burrows and Attwood, 1949).

The absorption cross-sections of raindrops (Mie, 1908; Burrows and Attwood, 1949) have been computed for use in Table 8. This latter table gives the decibel attenuation per kilometer in rains of different rates of fall and radio wavelengths between 0.3 and 10 cm. In Table 9, similar to Table 8, an additional set of results is contained for rains of measured drop size distribution.

Since the scattering coefficients (Mie, 1908) depend on the temperature (because of its effects on the dielectric properties of water), it is important to evaluate the attenuation of rain whose drops are at different temperatures from those in the preceding tables. Table 10 contains the necessary data relative to the change of attenuation with temperature and is to be used with Table 8. For example, in Table 8, with a precipitation rate of $\rho = 0.25$ mm/hr., temperature of 18°C , $\lambda = 1.25$ cm, the attenuation is 0.0215 db/km. Using the correction factors obtained from Table 10, for the same general conditions of precipitation and wavelength, for a temperature reading of 0°C the attenuation reads 0.02043 db/km; for a value of 30°C an attenuation of 0.019350 db/km is noted.

Rainfall Attenuation Climatology

The above paragraphs have been concerned with a descriptive presentation of the theoretical and technical background of the problem of attenuation by rain and atmospheric gases. In an attempt to circumvent the difficulties of the above methods of attenuation prediction, a climatological approach to this problem was attempted (Westwater et al, 1964). However, the results were disappointing due to the fact that the problems of a systematic climatological estimation of rainfall attenuation are many and varied. Answers are still needed for such questions as how often do various rainfall rates and drop sizes occur in geographical areas and over how large an area do these rate and drop size statistics apply (Bussey, 1950).

Unfortunately, the present state of meteorological knowledge concerning these problems is such that no conclusions can be drawn on a systematic or climatological basis. In view of these facts, it appears prudent at this time to provide only engineering estimates of the combined gaseous and rain absorption.

2.3 Hail

Ryde concluded that the attenuation caused by hail is one-hundredth that caused by rain, that ice crystal clouds cause no sensible attenuations, and that snow produces very small attenuation even at the excessive rate of fall of five inches an hour. However, the

Table 7 Percentage of total volume of rainfall occupied by raindrops of different diameters D (cm) and varying rainfall rates p (mm/hr).
[Burrows and Attwood, 1949]

precip. mm/hr D, in cm	0.25	1.25	2.5	12.5	25	50	100	150
	Percentage of total volume							
0.05	28.0	10.9	7.3	2.6	1.7	1.2	1.0	1.0
0.10	50.1	37.1	27.8	11.5	7.6	5.4	4.6	4.1
0.15	18.2	31.3	32.8	24.5	18.4	12.5	8.8	7.6
0.20	3.0	13.5	19.0	25.4	23.9	19.9	13.9	11.7
0.25	0.7	4.9	7.9	17.3	19.9	20.9	17.1	13.9
0.30		1.5	3.3	10.1	12.8	15.6	18.4	17.7
0.35		0.6	1.1	4.3	8.2	10.9	15.0	16.1
0.40		0.2	0.6	2.3	3.5	6.7	9.0	11.9
0.45			0.2	1.2	2.1	3.3	5.8	7.7
0.50				0.6	1.1	1.8	3.0	3.6
0.55				0.2	0.5	1.1	1.7	2.2
0.60					0.2	0.5	1.0	1.2
0.65						0.2	0.7	1.0
0.70								0.3

Table 8 (Burrows - Attwood)

Attenuation in decibels per kilometer for different rates of precipitation of rain. Temperature 18°C, λ in cm									
P mm/hr	$\lambda=0.3$	$\lambda=0.4$	$\lambda=0.5$	$\lambda=0.6$	$\lambda=1.0$	$\lambda=1.25$	$\lambda=3.0$	$\lambda=3.2$	$\lambda=10$
0.25	0.305	0.230	0.160	0.106	0.037	0.0215	0.00224	0.0019	0.0000997
1.25	1.15	0.929	0.720	0.549	0.228	0.136	0.0161	0.0117	0.000416
2.5	1.98	1.66	1.34	1.08	0.492	0.298	0.0388	0.0317	0.000785
12.5	6.72	6.04	5.36	4.72	2.73	1.77	0.285	0.238	0.00364
25.0	11.3	10.4	9.49	8.59	5.47	3.72	0.656	0.555	0.00728
50.	19.2	17.9	16.6	15.3	10.7	7.67	1.46	1.26	0.0149
100.	33.3	31.1	29.0	27.0	20.0	15.3	3.24	2.80	0.0311
150.	46.0	43.7	40.5	37.9	28.8	22.8	4.97	4.39	0.0481

Table 9 (Burrows - Attwood)

Attenuation in rains of known drop size distribution and rate of fall (decibels per kilometer)						
p mm/hr	Wavelength λ in cm					
	1.25	3	5	8	10	15
2.46	$1.93 \cdot 10^{-1}$	$4.92 \cdot 10^{-2}$	$4.24 \cdot 10^{-3}$	$1.23 \cdot 10^{-3}$	$7.34 \cdot 10^{-4}$	$2.80 \cdot 10^{-4}$
4.0	$3.18 \cdot 10^{-1}$	$8.63 \cdot 10^{-2}$	$7.11 \cdot 10^{-3}$	$2.04 \cdot 10^{-3}$	$1.19 \cdot 10^{-3}$	$4.69 \cdot 10^{-4}$
6.0	$6.15 \cdot 10^{-1}$	$1.92 \cdot 10^{-1}$	$1.25 \cdot 10^{-2}$	$3.02 \cdot 10^{-3}$	$1.67 \cdot 10^{-3}$	$5.84 \cdot 10^{-4}$
15.2	2.12	$6.13 \cdot 10^{-1}$	$5.91 \cdot 10^{-2}$	$1.17 \cdot 10^{-2}$	$5.68 \cdot 10^{-3}$	$1.69 \cdot 10^{-3}$
18.7	2.37	$8.01 \cdot 10^{-1}$	$5.13 \cdot 10^{-2}$	$1.10 \cdot 10^{-2}$	$6.46 \cdot 10^{-3}$	$1.85 \cdot 10^{-3}$
22.6	2.40	$7.28 \cdot 10^{-1}$	$5.29 \cdot 10^{-2}$	$1.21 \cdot 10^{-2}$	$6.96 \cdot 10^{-3}$	$2.27 \cdot 10^{-3}$
34.3	4.51	1.28	$1.12 \cdot 10^{-1}$	$2.32 \cdot 10^{-2}$	$1.17 \cdot 10^{-2}$	$3.64 \cdot 10^{-3}$
43.1	6.17	1.64	$1.65 \cdot 10^{-1}$	$3.33 \cdot 10^{-2}$	$1.62 \cdot 10^{-2}$	$4.96 \cdot 10^{-3}$

Table 10 Correction factor for rain attenuation (Burrows - Attwood)

Rate of ppt mm/hr	λ cm	Correction factor θ ()				
		$t=0^{\circ}\text{C}$	$t=10^{\circ}\text{C}$	$t=18^{\circ}\text{C}$	$t=30^{\circ}\text{C}$	$t=40^{\circ}\text{C}$
0.25	0.5	0.85	0.95	1.0	1.02	0.99
	1.25	0.95	1.00	1.0	0.90	0.81
	3.2	1.21	1.10	1.0	0.79	0.55
	10.0	2.01	1.40	1.0	0.70	0.59
2.5	0.5	0.87	0.95	1.0	1.03	1.01
	1.25	0.85	0.99	1.0	0.92	0.80
	3.2	0.82	1.01	1.0	0.82	0.64
	10.0	2.02	1.40	1.0	0.70	0.59
12.5	0.5	0.90	0.96	1.0	1.02	1.00
	1.25	0.83	0.96	1.0	0.93	0.81
	3.2	0.64	0.88	1.0	0.90	0.70
	10.0	2.03	1.40	1.0	0.70	0.59
50.0	0.5	0.94	0.98	1.0	1.01	1.00
	1.25	0.84	0.95	1.0	0.95	0.83
	3.2	0.62	0.87	1.0	0.99	0.81
	10.0	2.01	1.40	1.0	0.70	0.58
150.	0.5	0.96	0.98	1.0	1.01	1.00
	1.25	0.86	0.96	1.0	0.97	0.87
	3.2	0.66	0.88	1.0	1.03	0.89
	10.0	2.00	1.40	1.0	0.70	0.58

scattering by spheres surrounded by a concentric film of different dielectric constant does not give the same effect that Ryde's results for dry particules would indicate (Hathaway and Evans, 1959); Kerker, Langleben, and Gunn, 1951). For example, when one-tenth of the radius of an ice sphere of radius 0.2 cm melts, the scattering of 10 cm radiation is approximately 90 per cent of the value which would be scattered by an all-water drop.

For the particular combinations of wavelengths (λ) and droplet radii (a) such that $\alpha = 0.126$ ($\alpha = 2\pi a/\lambda$) calculations by Kerker, Langleben and Gunn (1951) showed that particules attained total-attenuation cross-sections corresponding to all-melted particles when less than 10 per cent of the ice particles were melted. When the melted mass reached about 10-20 per cent, the attenuation was about twice that of a completely melted particle. These calculations show that the attenuation in the melting of ice immediately under the 0°C (Best, 1957) isotherm can be substantially larger than in the snow region just above, and under some circumstances, greater than in the rain below the melting level. Further melting cannot lead to much further enhancement, apparently, and may lead to a lessening of the reflectivity of the particle by bringing it to sphericity or by breaking up of the particle.

REFERENCES

- Artman, J. O. (1953). Absorption of Microwaves by Oxygen in the Millimeter Wavelength Region, Columbia Radiation Laboratory Report.
- Artman, J. O., and J. P. Gordon (1954). Physical Review 96(5), 1237.
- Battan, L. J. (1959). Radar Meteorology (University of Chicago Press).
- Bean, B. R., and R. L. Abbott (1957). Oxygen and Water Vapor Absorption of Radio Waves in the Atmosphere, Geofisica Pura e Applicata 37, 127-144.
- Becker, G. B., and S. H. Autler (1946). Physical Review 70(5), 300.
- Bennett, C. A., and N. L. Franklin (1954). Statistical Analysis in Chemistry and The Chemical Industry. (John Wiley and Sons, New York)
- Best, A. C. (1957). Physics in Meteorology (Pittman and Sons, London).
- Birnbaum, G., and A. A. Maryott (1955). Physical Review 99, 1636.
- Burrows, C. R., and S. S. Attwood (1949). Radio Wave Propagation, Consolidated Summary Technical Report of the Committee on Propagation, NDRC, 219 (Academic Press, New York).
- Bussey, H. E. (1950), Proc. IRE 38(7), 781.
- Compendium of Meteorology (1951). American Meteorological Society, Boston, Mass.
- Deming, W. E. (1943). Statistical Adjustment of Data (John Wiley and Sons, New York).
- Donaldson, R. J., Jr. (1955). J. of Meteorology 12(3), 238.
- Dutton, E. J., and G. D. Thayer (1961). Techniques for computing refraction of radio waves in the troposphere. NBS Tech. Note No. 97.
- Ghosh, S. N., and H. D. Edwards (1956). Air Force Surveys in Geophysics, No. 82.
- Gunn, K. L. S., and T. W. R. East (1954). Quart. J. Royal Meteorological Society, London XXX, 522.
- Hathaway, S. D., and H. W. Evans (1959). Bell System Tech. J. 38(1).
- Hill, R. M., and W. Gordy (1954). Physical Review 93(5), 1019.
- Kerker, M., M. P. Langleben, and R. L. S. Gunn (1951), J. Meteorology 8, 424.
- Laws, J. O., and D. A. Parsons (1943). Trans. Am. Geophys. U., 24th Annual Meeting, 452.

References - Cont.

Mie, G. (1908). *An Physik* 25, 377.

Ratner, B. (1947). Upper air average values of temperature, pressure, and relative humidity over the United States and Alaska (U. S. Weather Bureau).

Ryde, J. W. (1946). Meteorological factors in radio wave propagation, Phys. Society, London, 169.

Ryde, J. W., and D. Ryde (1945). Attenuation of centimeter waves by rain, hail, fog, and clouds (General Electric, Wembly).

Saxton, J. A., and H. G. Hopkins (1951). *Proc. IRE* 98, Pt. III, 31.

Straiton, A. W., and C. W. Tolbert (1960). *Proc. IRE* 48(5), 898.

Shklovsky, I. S. (1960). *Cosmic Radio Waves* (Harvard University Press).

Tinkham, M., and M. W. P. Strandberg (1955). *Physical Review* 99(2), 537.

Talbert, C. W., and A. W. Straiton (1957). *Trans IRE* AP-5(2), 239

Van Vleck, J. H. (1947a). *Physical Review* 71, 413.

Van Vleck, J. H. (1947b). *Physical Review* 71, 421.

Van Vleck, J. H. (1951). *Propagation of Short Radio Waves*, Chap. 8, (McGraw-Hill Book Company, New York).

Weickmann, H. K., and H. J. aufm Kampe (1953). *J. Meteorology* 10, 204.

Westwater, E. R., B. R. Bean, and R. L. Abbott (1964). *Absorption Properties of the Troposphere at Radio Frequencies*, NBS Report No. 8270.